



University of Kentucky
UKnowledge

Theses and Dissertations--Mechanical
Engineering

Mechanical Engineering


2021

Experimental Investigation of Image Distortion in a Mach 6 Hypersonic Flow

Ricky W. Green II

University of Kentucky, greenrw94@gmail.com

Author ORCID Identifier:

 <https://orcid.org/0000-0001-6048-1967>

Digital Object Identifier: <https://doi.org/10.13023/etd.2021.349>

[Right click to open a feedback form in a new tab to let us know how this document benefits you.](#)

Recommended Citation

Green, Ricky W. II, "Experimental Investigation of Image Distortion in a Mach 6 Hypersonic Flow" (2021).
Theses and Dissertations--Mechanical Engineering. 182.
https://uknowledge.uky.edu/me_etds/182

This Master's Thesis is brought to you for free and open access by the Mechanical Engineering at UKnowledge. It has been accepted for inclusion in Theses and Dissertations--Mechanical Engineering by an authorized administrator of UKnowledge. For more information, please contact UKnowledge@lsv.uky.edu.

STUDENT AGREEMENT:

I represent that my thesis or dissertation and abstract are my original work. Proper attribution has been given to all outside sources. I understand that I am solely responsible for obtaining any needed copyright permissions. I have obtained needed written permission statement(s) from the owner(s) of each third-party copyrighted matter to be included in my work, allowing electronic distribution (if such use is not permitted by the fair use doctrine) which will be submitted to UKnowledge as Additional File.

I hereby grant to The University of Kentucky and its agents the irrevocable, non-exclusive, and royalty-free license to archive and make accessible my work in whole or in part in all forms of media, now or hereafter known. I agree that the document mentioned above may be made available immediately for worldwide access unless an embargo applies.

I retain all other ownership rights to the copyright of my work. I also retain the right to use in future works (such as articles or books) all or part of my work. I understand that I am free to register the copyright to my work.

REVIEW, APPROVAL AND ACCEPTANCE

The document mentioned above has been reviewed and accepted by the student's advisor, on behalf of the advisory committee, and by the Director of Graduate Studies (DGS), on behalf of the program; we verify that this is the final, approved version of the student's thesis including all changes required by the advisory committee. The undersigned agree to abide by the statements above.

Ricky W. Green II, Student

Dr. Kozo Saito, Major Professor

Dr. Alexandre Martin, Director of Graduate Studies

EXPERIMENTAL INVESTIGATION
OF IMAGE DISTORTION IN A MACH 6
HYPERSONIC FLOW

THESIS

A thesis submitted in partial fulfillment of the
requirements for the degree of Master of Science in
Mechanical Engineering in the College of Engineering
at the University of Kentucky

By

Ricky Green

Lexington, Kentucky

Director: Dr. Kozo Saito Professor of Mechanical Engineering

Lexington, Kentucky

2021

Copyright © Ricky Green 2021

<https://orcid.org/0000-0001-6048-1967>

ABSTRACT OF THESIS

EXPERIMENTAL INVESTIGATION OF IMAGE DISTORTION IN A MACH 6 HYPERSONIC FLOW

The image distortion that is inherently present when imaging through a flow field at hypersonic speeds was investigated. The original problem involves observation of the outside world from the inside an aircraft moving at hypersonic speeds. For this work, a Mach 6 hypersonic wind tunnel at Wright Patterson Air Force Base (WPAFB) was used and optical patterns were imaged with and without flow field characteristics. Two test campaigns were scheduled to conduct experiments that would provide answers to the proposed problem of the effect on observable aberrations through flow fields.

During the first test campaign, October 2017, optical patterns were laser etched on anodized aluminum inserts that would couple to a 15°-degree wedge probe that had been operated with the Mach 6 tunnel previously. During this test phase, lessons learned were extremely acknowledged for preparing for the second campaign in February-March 2019. A primary effect observed was due to tunnel vibrations that created apparent optical distortion by “smearing” the optical patterns over the acquisition time of the camera. During the second test campaign there were 2 primary test models that would be mounted in the tunnel for optical analysis. Newly manufactured steel plates were coupled to the already investigated 15°-degree wedge probe for verification of what was observed previously. Also, a 7° half angle cone was manufactured as a replica of a cone that was already in operation at WPAFB.

Characterization of optical distortion was done by using a quantity known as a Strehl Ratio. The Strehl Ratio is defined as the ratio of the peak intensity of a point source from an aberrated image, which has been affected due to distortion, to the corresponding point source from a diffraction limited system. Line Distribution Functions (LDFs) were identified to expand the definition from a ratio of maximums to a ratio of the shapes of the line widths. Measured vibrational influences were extracted in both the axial and vertical directions of flow to account for any artificial distortion mechanisms. These lines in both directions created our optical patterns simultaneously giving information of vibrational influences in either direction as well as the measured distortion over the test targets.

Lastly, there was an attempt to relate the experimental findings to real world applications. Considerations from the first test campaign using the wedge probe are presented for this using what is known from the General Image Quality Equation (GIQE). This was developed as an analytical solution for determining image quality parameters within the National Imagery Interpretability Rating Scale (NIIRS).

KEYWORDS: image distortion, hypersonic, Strehl ratio, line distribution function

Ricky Wayne Green II
(Name of Student)

(07/27/21)
Date

EXPERIMENTAL INVESTIGATION
OF IMAGE DISTORTION IN A MACH 6
HYPERSONIC FLOW

By
Ricky Wayne Green II

Dr. Kozo Saito

Director of Thesis

Dr. Alexandre Martin

Director of Graduate Studies

(07/27/21)

Date

TABLE OF CONTENTS

LIST OF TABLES.....	vi
LIST OF FIGURES.....	vii
CHAPTER 1. INTRODUCTION	10
1.1 Objectives of Research	10
1.2 Distortion Measurement Methods.....	11
CHAPTER 2. TEST FACILITIES AND EXPERIMENTAL SETUPS	15
2.1 Test Models	16
2.2 Imaging Setups.....	19
2.2.1 Side Window Cameras	20
2.2.2 Surface Patterns applied to the models.....	22
2.2.3 Spectral Sensitivity of the Nikon D610.....	24
2.2.4 IR imaging.....	25
2.3 Test Matrices.....	27
2.4 Vibrational Analysis.....	29
CHAPTER 3. FLOW FIELD DATA ANALYSIS.....	31
3.1 Flow Field Analysis from Schlieren.....	31
3.2 IR imaging of the wedge model.....	34
3.3 IR imaging of the cone Model	38
3.4 Vibrational influence on the Imaging.....	40
3.5 Distortion Analysis Methods.....	47
CHAPTER 4. ANALYSIS METHODS ON OPTICAL DISTORTION	51
4.1 Strehl Ratios and Line Distribution Functions.....	51
4.2 Methods of Extracting LDFs from the Measured Profiles.....	53
4.2.1 Fitting Measured data through an integration of a single High Resolution Gauss profile	55
4.2.2 Superposition of multiple narrow Gauss profiles.....	57
4.2.3 Direct Interpolation of measured Line Profiles using an Averaging over Shifted Profiles.....	60
4.3 Lab Experiment using a back Illuminated Slit with Artificial Distortion.....	61
4.4 Results from Mach 6 Wind Tunnel Experiment	62
4.4.1 Selection of Analysis Locations for the models	63
4.4.2 Strehl Ratio Results with the Wedge Probe	66
4.4.3 Strehl Ratio Results of the Cone Model	70
CHAPTER 5. EXTRAPOLATION OF THE WIND TUNNEL TEST TO REAL WORLD IMAGING.....	73
5.1 General Image Quality Equation	73
5.2 Extrapolated Results.....	76

CHAPTER 6. CONCLUSIONS	80
[APPENDICES]	84
<i>[APPENDIX 1. TEST CAMPAIGN PROTOCOLS]</i>	84
<i>[APPENDIX 2. TECHNICAL DRAWINGS]</i>	93
[REFERENCES]	96
[VITA]	97

LIST OF TABLES

<i>Table 2.1</i>	<i>Working conditions for Mach 6 wind tunnel</i>	<i>16</i>
<i>Table 5.1</i>	<i>Coefficients for current version of GIQE 5</i>	<i>74</i>
<i>Table 5.2</i>	<i>Numerical NIIRS values for 1900PSI at -15° AoA.....</i>	<i>77</i>
<i>Table 5.3</i>	<i>Numerical NIIRS values for 1900PSI at -0° AoA.....</i>	<i>78</i>
<i>Table 5.4</i>	<i>Numerical NIIRS values for 900PSI at -15° AoA.....</i>	<i>78</i>
<i>Table 5.5</i>	<i>Numerical NIIRS values for 900PSI at -0° AoA.....</i>	<i>78</i>

LIST OF FIGURES

Figure 1.1	Illustration showing reduction in contrast as line pair widths are made finer [1].....	13
Figure 2.1	Open test section of the Mach 6 wind tunnel.	15
Figure 2.2	Schematic of the Mach 6 High Reynolds Number Facility.....	16
Figure 2.3	15° Wedge Probe that was already in use at WPAFB.....	17
Figure 2.4	Detachable 7° half-angle cone that was used by WPAFB.....	19
Figure 2.5	Image displaying the top and side window access points into the tunnel test chamber.....	20
Figure 2.6	15° wedge plate insert used during October 2017 test campaign.....	22
Figure 2.7	15° wedge plate insert, and laser etching used during Feb-Mar 2019 test campaign.....	23
Figure 2.8	7° half angle wedge cone body and 10% tip etching.....	24
Figure 2.9	Spectral sensitivity of the RGB converted pixels for a Nikon D610 at a White Balance (WB) of 5560K.....	25
Figure 2.10	A black plate without laser etching positioned that the test height inside of the tunnel with 3 thermocouples attached at the surface.....	26
Figure 2.11	Calibration curves from the thermocouple experiments for the wedge (above) and cone (below) with the 10% and 20% tips.....	27
Figure 2.12	Balcar 6400 Xenon Flash lamp flash durations measured at the lowest and highest power levels.....	28
Figure 2.13	Image of the 15° wedge probe illustrating the location and mounting of the tri-axial accelerometer to the insert plate.....	30
Figure 3.1	Theta-Beta-M relation curve with the measured deflection and shock wave angles showing the measured tunnel Mach number at ~5.8.....	32
Figure 3.2	Schlieren shadowgraphs for the 15° wedge probe over all AoA and reservoir pressures.....	33
Figure 3.3	Schlieren shadowgraphs for the 7° half angle cone with the 10% attached tip at different angles of attack.....	33
Figure 3.4	Raw IR at 1900PSI and 15° angle of attack at different times showing the extraction method of intensities and temperatures for a selected streamline.....	35
Figure 3.5	Normalized intensity and temperature profiles for extracted streamlines at beginning, middle and end test for 15° angle of attack over all 3 reservoir pressures.	37
Figure 3.6	Normalized intensity and temperature profiles for extracted streamlines at beginning, middle and end test for 5° angle of attack over all 3 reservoir pressures.	38
Figure 3.7	Raw IR images of the 10% cone tip over all 3 reservoir pressures.....	39
Figure 3.8	Comparison of transitional locations observed from WPAFB [3,8,9].....	39
Figure 3.9	Raw IR images of the 20% cone tip over all 3 reservoir pressures.....	40

Figure 3.10	Measured displacement of the wedge probe at 900 and 1400 PSI reservoir pressure in the axial (X-axis) and perpendicular (Z-axis) directions to flow. Vertical and Horizontal displacements are measured at the camera lens end.	43
Figure 3.11	Measured displacement of the wedge probe at 1900 PSI reservoir pressure in the axial (X-axis) and perpendicular (Z-axis) directions to flow. Vertical and Horizontal displacements are measured at the camera lens end.....	44
Figure 3.12	15° wedge probe with plate inserts showing the vertical and horizontal LDF extraction method over all lines inside of the yellow pattern.....	45
Figure 3.13	Measured vertical displacement of horizontal lines in subsequent images using Nikon camera with constant illumination for 1400 and 1900PSI [3]	46
Figure 3.14	Measured horizontal displacement of vertical lines in subsequent images using Nikon camera with constant illumination for 1400 and 1900 PSI [3]	46
Figure 3.15	Illumination pattern of a point spread function for a diffraction limited and aberrated case [1].....	48
Figure 3.16	Illustration of how the LSF is derived from the PSF [1]	49
Figure 4.1	General principles of how LDFs were extracted during tunnel operation [3]	51
Figure 4.2	Theoretical Gauss and Voight distributions are investigated for reformulation of Strehl Ratio.	52
Figure 4.3	Comparison of theoretical Airy disk and Gaussian profiles with similar FWHM.....	53
Figure 4.4	Illustration of the high-resolution profiles on the CCD.....	54
Figure 4.5	Best fitting of a measured profile using a single Gauss distribution.....	55
Figure 4.6	Observed relationship between the profile HWHM and r3max.....	56
Figure 4.7	Observed relationship between the profile HWHM and r4max.....	57
Figure 4.8	Using a superposition of many narrow Gauss profiles to create a non-Gauss generating LDF.....	58
Figure 4.9	Best fitting of a measured profile using a non-Gauss distribution created from a superposition of many narrow Gauss profiles	58
Figure 4.10	Sketch of the Optical Setup used for investigating the setup sensitivity using a back illuminated slit with artificial diction mechanisms.....	62
Figure 4.11	Selected locations for analysis on the wedge plate from the October 2017 test campaign	63
Figure 4.12	Surface evolution of the LDFs on plate insert during the first test.....	64
Figure 4.13	Selected locations for analysis on the wedge plate from the February-March 2019 test campaign.....	65
Figure 4.14	Selected locations for analysis on the cone base of 20% and 10% blunt tips and on the 10% tip with the least influence of particle damage	66

Figure 4.15	Resulting Strehl Ratios from the old test data using the FWHM of the extracted LDFs for 900 and 1900PSI over all angles of attack.	67
Figure 4.16	Strehl Ratios extracted from the flash illuminated images at 900 and 1900PSI using both intensity and FWHM ratios.	68
Figure 4.17	Strehl Ratios extracted from LDF FWHM ratios with constant illumination and varying acquisition times at 1900PSI and 15° angle of attack.....	69
Figure 4.18	Strehl Ratios from LDF FWHM ratios vs distance to the 10% and 20% blunt cone tip on the cone base for all reservoir pressures under a 0° angle of attack for the RGB camera pixels.	70
Figure 4.19	Strehl Ratios from LDF FWHM ratios vs distance to the 10% and 20% blunt cone tip on the cone base for all reservoir pressures under all angle of attack averaged over the RGB camera pixels.....	71
Figure 5.1	The 5° slanted edge area used for characterizing the camera's ability the reproduce sharp edges.....	75
Figure 5.2	The process of measuring RER a half pixel on either side of the 0.5 measured intensity	75
Figure 5.3	Extracted NIIRS values for hypothetical distances up the 100km for experiments at 1900PSI and AoA of 0° and -15°.....	76

CHAPTER 1. INTRODUCTION

It is important to investigate the interactions of a flow field body around high-speed vehicles for the purpose of optical performance when imaging through the flow patterns. The sensor design for this purpose to be used requires a qualitative and quantitative investigation of how imaging is impaired through the boundary layer and shock structures. For application to hypersonics and Electro-Optic/Infrared (EO/IR) sensor analysis, distortion as a result from various aero-optic effects like boresight error and remote sensing is to be quantified.

The basic problem at hand is the observation of the outside world from inside high-speed vehicles through the flow field experienced. In the case that a wind tunnel is used, observation optics in the form of defined patterns on a test model would be observed with and without flow field boundaries. This means that the optical path is in reverse, that we are actually looking from the outside world into the vehicle traveling at hypersonic. Optical distortion would be quantified as the deformation measured when imaging the optical patterns when there is flow around the model compared to when there is no flow.

Investigation of optical distortion in hypersonic flows was done conducting experiments using the 15° wedge probe with attachable plates and laser etched optical patterns and with the simplified 7° half-angle cone. The main effects of distortion were expected to be caused by the flow field around the body; and the stronger shock structures were expected to affect imaging negatively. Scale modeling would be used to interpret the experimental results on a real-world level.

1.1 Objectives of Research

The purpose of this work is to qualitatively and quantitatively investigate how imaging is impaired through a flow field around a body that is created in hypersonic flight. Hypersonic flight is defined as any flight through Earth's atmosphere at speeds Mach 5 and greater [11]. In this case a Mach 6 High Reynolds Number facility at Wright Patterson Air Force Base (WPAFB) was used for experimental work. At this facility test models with optical patterns were mounted inside of the tunnel and exposed to the flow. For the purposes of the experiments, it is assumed that the results achieved by measuring the

observation optics from outside would yield comparable results to if imaging was done from the inside. This is an assumption that the aero-optic effects present are a result of the inherent gradients generated across a shock structure which would be the same from viewing from inside or outside [2].

Several experimental setups and observation optics were selected for investigating distortion effects while applied to different geometries. These included a 15° wedge probe already available at WPAFB with plate inserts that could be mounted to the flat and angled sides of the wedge. Also available was a 7° half-angle cone model that had been tested at various angles of attack in the past. The existing model, though, was fully instrumented with thermocouples and pressure sensors to measure data during testing. This model was also polished for a very smooth and shiny surface so creating suitable observation optics on the surface would pose a challenge. Although, blackening of the surface seemed to be a viable method, in an attempt to avoid damaging any instrumentation while altering the surface of the existing WPAFB, a geometrically identical copy was manufactured at University of Kentucky's (UK) Mechanical Engineering machine shop. The cone constructed at UK was then blackened using a black zinc chemical coating and optical patterns were laser etched to the surface. The new cone model consisted of a base section and interchangeable tips consisting of 10% and 20% bluntness of the 4-inch diameter cone base. Different observation techniques including visual and IR imaging were applied to investigate the observed distortion and possible transition to turbulence over the test model.

1.2 Distortion Measurement Methods

Current analysis methods determine optical distortion differently depending on the quantity to be measured. For example, commercially available test targets from Edmund Optics offer options for analyzing resolution, distortion and many more. These two options are stated for simplicity as one could define observed distortion as a decrease in resolution. Distortion is a vague term to describe these test targets though as Edmund Optics defines this effect as a percent change in the field height of the image. Because of this, various optical patterns (comprised from the various known targets) and analysis methods were

carefully tested and chosen for test experiments during the early 2017 test campaign. Some of the test targets selected for investigation for this problem are discussed.

A common pattern found on resolution targets consists of a series of light and dark alternating lines spaced at equal widths. One group of a light and dark line is referred to as a line pair. A given test target may contain several of these line pairs at finer widths spaced more closely together to determine the resolution limit of the system. The smallest discernable line pair width is described to be the system's limiting resolution in line pairs per millimeter (LP/mm) [1]. Such a test target is more commonly referred to as a variable frequency target. These provide resolution information quickly, which is great when varying lens systems, object distance, or anything else that may alter the Field of View (FoV) of the system. Our proposed setup would have a constant FoV and thus, these patterns may not provide meaningful information. If these patterns were imaged and distortion is induced from flow field, the maximum resolvable LP/mm would decrease, but there is no evidence that this is a proper way to define distortion for our problem. A more detailed quantification of the system's maximum performance can be determined by using a single pair of these alternating light and dark bars. The analysis methods will be discussed in more detail further on in the analysis section 3.3 by using the Strehl Ratio.

The Strehl Ratio was identified as a quantitative metric for measuring distortion through turbulent atmosphere [2]. The Strehl Ratio is defined as the ratio of the peak intensity of a point source from an aberrated image, which has been affected by distortion, to the peak intensity of corresponding point source from a diffraction limited system. The defining characteristics of a diffraction limited system are given by the Airy disk which is defined as the best focused spot of light that is produced by a point source imaged by a perfect lens with a circular aperture, which in turn determines the theoretical maximum resolving power of the lens [1].

Another optical analysis process investigated was the use of the Modulation Transfer Function (MTF). This method is constructed from imaging over light and dark bars that vary in equal spacing and thickness as in a variable frequency target. When imaging over a variable frequency target each line pair would continue to increasingly "blur" into each other as the frequency of the alternating light and dark lines increases.

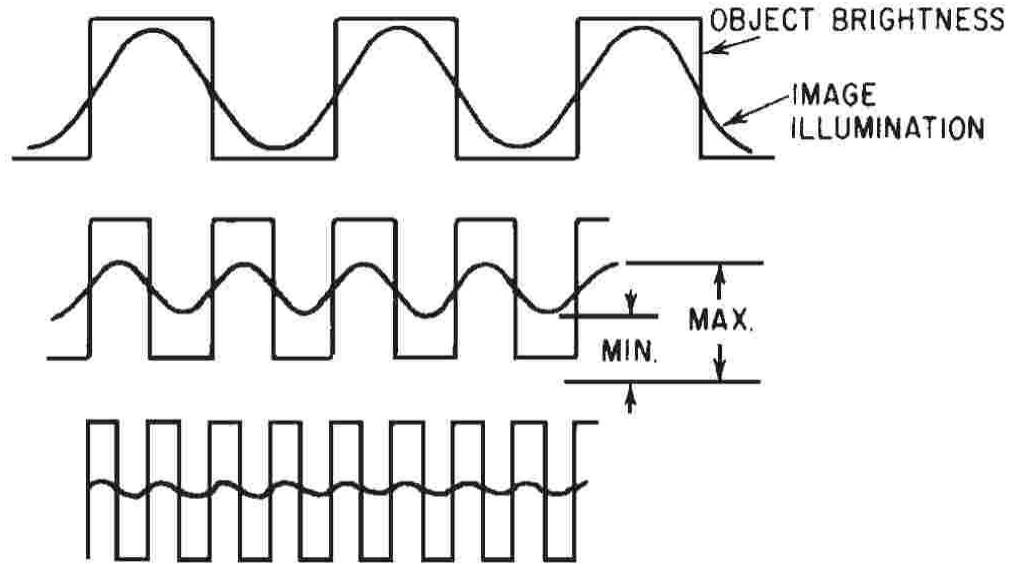


Figure 1.1 Illustration showing reduction in contrast as line pair widths are made finer [1].

The main effect present is the achievable contrast imaged from the line pairs with decreasing width. Contrast, or more commonly referred to as modulation in this context, is commonly expressed as a ratio of the maximum (max) and minimum (min) illumination levels of the imaged profiles as shown in Figure 1.1 [1]. Also, Fig. 1.1 demonstrates the effect of decreasing width line pairs with a uniform object brightness on modulation.

$$Modulation = \frac{max - min}{max + min} \quad \text{Eq. 1}$$

The MTF curve is then defined by calculating and plotting the modulation as described from Eq. 1 with respect to the corresponding frequency of the line widths. This will describe the optical system and the limiting characteristics as a function of distinguishing between light and dark and has become almost the universal quantitative analysis method for image quality [1].

The MTF method can ultimately be directly related to a Strehl ratio which was determined as the quantitative measurement for investigating the induced flow field distortion for this work. Alternatively, it can also be computed as a ratio of the volume under three dimensional aberrated (distortion induced) MTF curve to the non-distorted MTF curve. In addition, a quick assessment of image quality can also be done simply by using the area under the two-dimensional curves MTF curves [1].

The discussed targets, methods and ideas provide the optical analysis approaches that were investigated to build upon determining a valid procedure to investigate the influence of distortion through a flow field. Of course, the Strehl Ratio immediately stood out and was primarily focused to be our quantitative metric as it has previously been used for determining distortion in turbulent atmosphere [2]. This appeared to be the exact quantity that would be used. The final procedure used for quantifying the observed distortion will be discussed later.

For analysis, appropriate test targets were imaged through the flow field as illuminated surface patterns on the test probes. The optical patterns were laser etched onto metal plates that could be mounted to the 15° wedge model, and onto the surface of the 7° half-angle cone that was black zinc plated before being laser edged. These patterns were primarily composed of lines that would form a grid pattern and could be analyzed similarly as described above as a single pair of alternating light and dark bars. Although additional patterns were also attempted for use in analysis during the initial 2017 test campaign; these consisted of variable frequency targets, star sector targets, as well as point sources; the gridded line profiles were most useful in distortion analysis and were primarily adopted as a lesson learned from the first test campaign to the surface patterns during the 2019 test campaign. Information on distortion is coupled to the shape of the parallel lines created by the gridded patterns as well as the degree of blurring that is experienced.

Several imaging and illumination setups were used in recording data before, during and after testing. As a baseline for measuring distortion, a commercially available Nikon D610 coupled with several different illumination methods was used. In addition, to gather more information on the flow structures and thermal loads experienced by the test models, Schlieren and IR imaging were used. Other imaging methods were also considered for data acquisition. These included an industry used Redlake Megaplus and a high-speed Phantom Miro M310, both with 12-bit AD conversion for higher discretization over pixels. More information on these imaging setups will be discussed in more detail later in Chapter 2.

CHAPTER 2. TEST FACILITIES AND EXPERIMENTAL SETUPS

The facility used for the experimental work was a Mach 6 high Reynolds Number wind tunnel built in 1972 and located at Wright Patterson Air Force Base, Area B, Dayton, Ohio. This is an intermittent blow down tunnel. Upstream of the nozzle is a 12-inch open jet configuration and, downstream inside the chamber, is a uniform 10-inch diameter cross section that is used as the testing section. The air is supplied from a 9,200 ft³ bottle farm that offers working conditions between 700-2,100 PSI and is heated by a pebble bed reservoir composed of 50,000 lbs of 3/4-inch stainless steel balls. Fig. 2.1 shows the tunnel open to view the test section. For our tests, a sting adapter (present in model attachment in Fig. 2.4) was mounted inside the chamber to a hydraulic lift that would inject and eject the model during flow on. The sting was able to allow for different angles of attack for information on differences in distortion when imaging through stronger or weaker shock structures. The sting adapter could provide changes of $\pm 15^\circ$ angle of attack and $\pm 5^\circ$ yaw. Table 2.1 characterizes the working conditions of the facility.

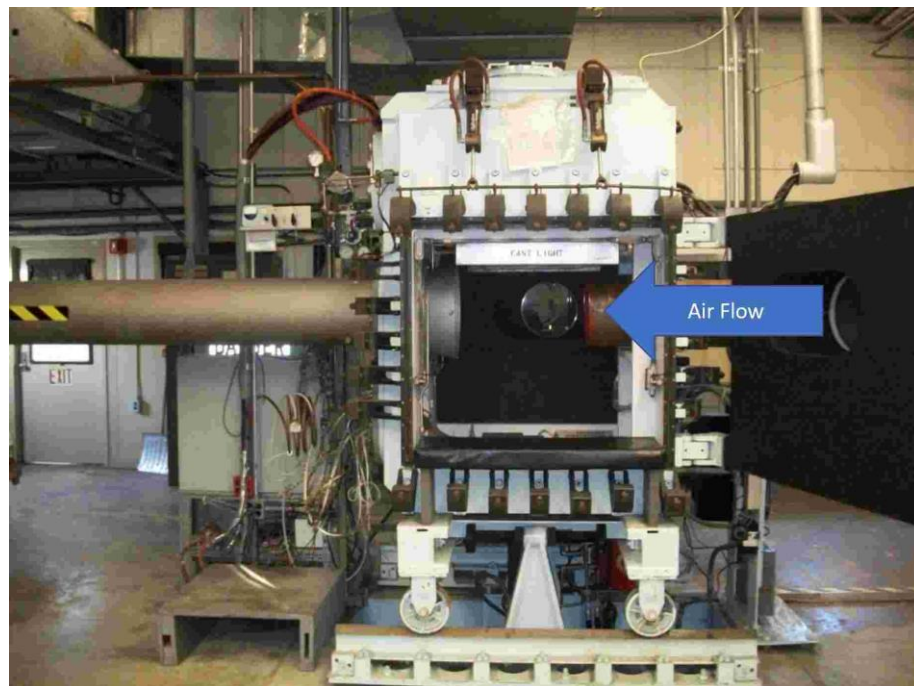


Figure 2.1 Open test section of the Mach 6 wind tunnel.

Table 2.1 Working conditions for Mach 6 wind tunnel

Condition	Description
Test Section	There is a uniform 10-inch diameter cross section, 17-28 inches long.
Mach Number	6. (Schlieren calibration gave 5.85).
Temperature	900-1100° R (227-338° C)
Pressure	Operating pressures of 700-2100 PSI
Reynolds Number Range	10-30 million/ft
Test Time / Day	5 minutes at Reynolds number 30 million/ft 12 minutes at Reynolds number 10 million/ft
Test Medium	Air
Density Altitude Simulation	30,000 – 60,000 ft

The tunnel has two primary viewing windows into the test section. These windows will be referred to as the side window (viewing into the chamber as Fig. 2.1 is positioned) and the top window which views down into the chamber. The setups used at the different viewing angles are discussed below.

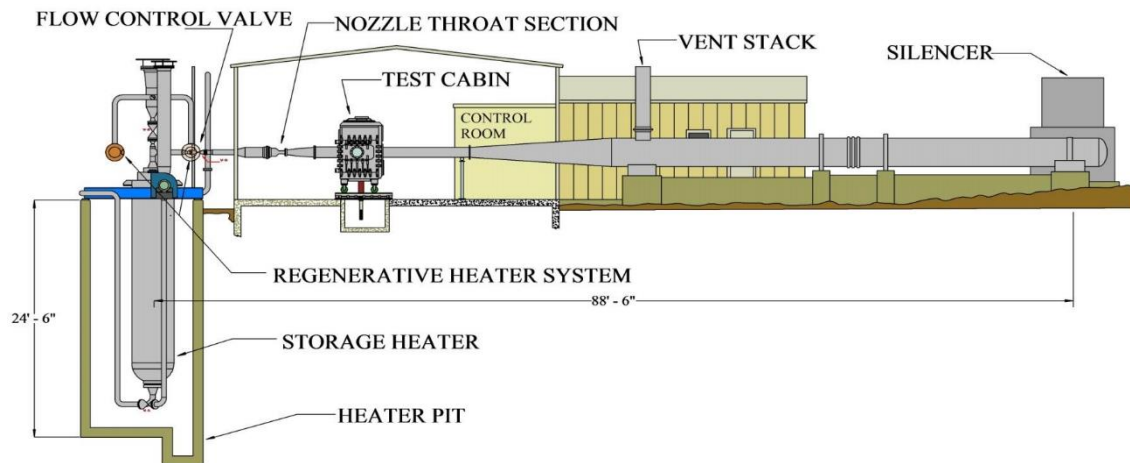


Figure 2.2 Schematic of the Mach 6 High Reynolds Number Facility

2.1 Test Models

There was consideration as to what models would be used in investigating optical distortion generated through hypersonic flow fields. One test model readily available and

already in operation at WPAFB was the 15° wedge probe which was used as the primary test subject in the first test campaign. This model has interchangeable plate inserts (4 x 5 x 0.06 inches), located at 3 inches and approximately 2 inches from the leading edge the flat and angled sides, respectively. Fig. 2.3 shows the model that was provided.

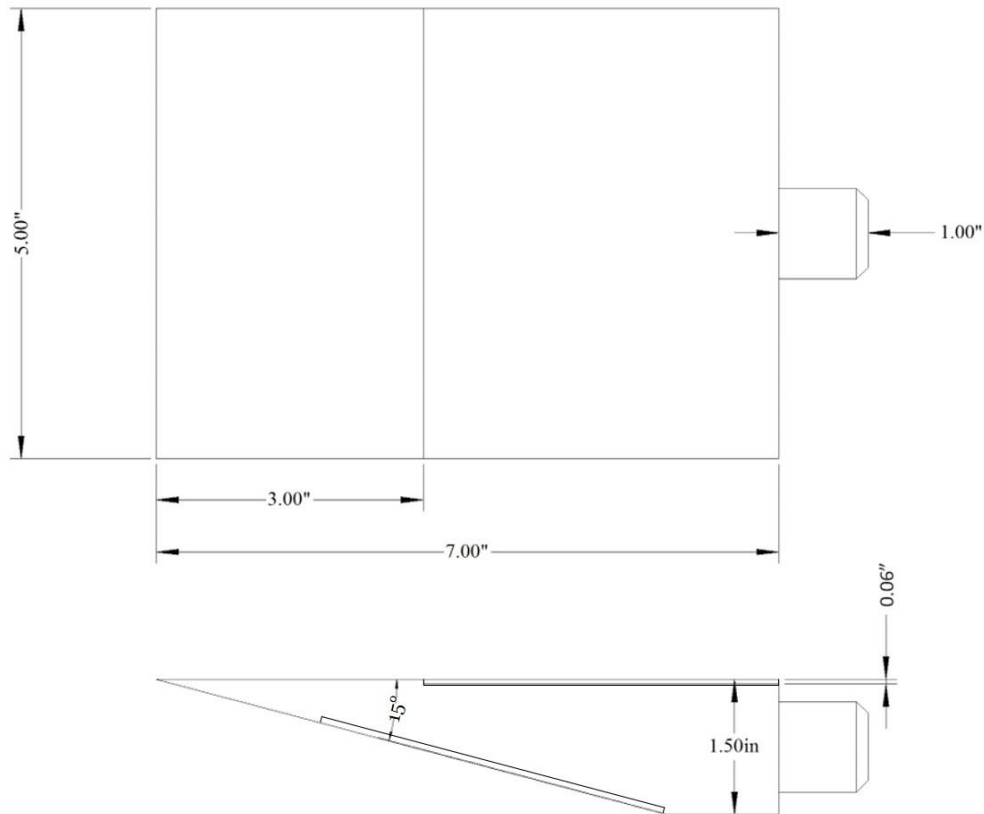


Figure 2.3 15° Wedge Probe that was already in use at WPAFB

Initially the plate inserts were made of an anodized aluminum which allowed for easy laser etching of optical patterns. Although this appeared to be an easy solution to coupling optical patterns to the wedge model, the structural integrity of the material over the steel plates that had been run by WPAFB in the past posed an issue in the first test campaign. During the later test phases the plate material was changed to steel to account for this concern and a black zinc coating was applied to the surface of the steel to allow for laser etching of new patterns. In addition to the wedge model available, it was thought to consider manufacturing wedge models with blunt tips to delay transition to turbulent flow. For the current wedge, it was thought that the transitioning region would be ~4 to 5 inches downstream of the leading edge which would be on the location of where the plate inserts

are. Infra-Red (IR) measurements were conducted to investigate transition to turbulence indicated by an increased heat load to the surface, yielding an increase in surface temperature. The expected turbulent regions expected from what is seen in the IR would be used for comparison with those which are laminar.

Any thermal loads could affect the plate in terms of expansions over the length of the plate. Such expansions could also be interpreted as broadening or deformations over a line profile during analysis. During tunnel operation a temperature change on the surface of the plate was observed to be on order of about 70°C was observed. If we consider the worst-case scenario then the anticipated linear thermal expansion over the 127 mm width (5 inches) would be ~0.21 mm. If these same parameters are considered for linear expansion over single line which might be mistaken as unwanted broadening, a maximum expansion on order of ~0.1 μm. This would be negligible and rather undetectable as this dimension is on order of 1/30th of the measured pixel sizes. These considerations were considered when determining where on the plates to take measured data, and to assess if the effect of thermal expansion could be seen as falsely broadening the surfaces patterns during the test phase.

Another model also frequently in operation at WPAFB is the 7° half-angle cone model mentioned earlier. This model was also used extensively in the Mach 6 hypersonic tunnel for investigation of flow field structures, thermal analysis of the surface, as well as transition locations from the cone tip. The model described here was still in use and instrumented with dozens of thermocouples to monitor the heating on the surface. To avoid possible damage to this more sophisticated and expensive model during the plating and edging process, a simplified but geometrically identical model was designed at the University of Kentucky (UK) and manufactured in the College of Mechanical Engineering machine shop. Simplifications of the cone are only internal and create a thicker model, rather increasing structural integrity. The cone was designed to have interchangeable tips of 10 and 20% bluntness which determines the ratio of the tip diameter to the cone base diameter. Technical drawings of the cones manufactured at UK are included in [APPENDIX 2. TECHNICAL DRAWINGS].

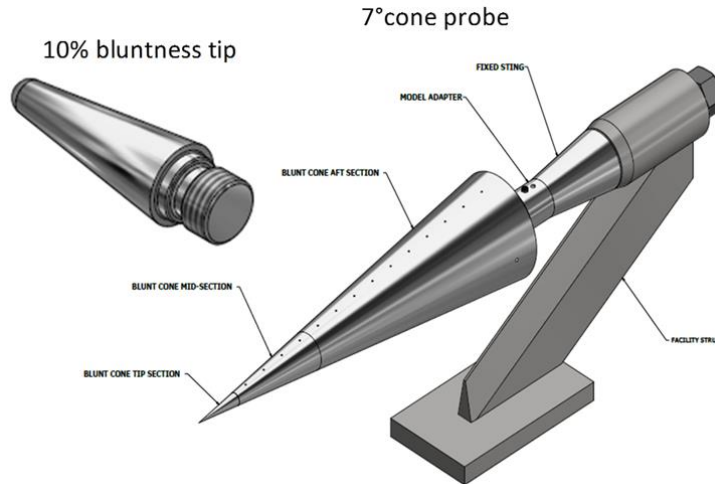


Figure 2.4 Detachable 7° half-angle cone that was used by WPAFB

2.2 Imaging Setups

Multiple camera and illumination setups were tested and used to achieve the highest quality data that could be obtained for distortion analysis. These setups were determined as those that did not saturate the camera sensor, but also had a high signal to noise ratio (SNR). Initially, there were several camera setups that were intended to be used to image the test models from the 2 available viewing angles (side and top views). These imaging setups and the locations mounted at the side and top of the tunnel are discussed further in this chapter.

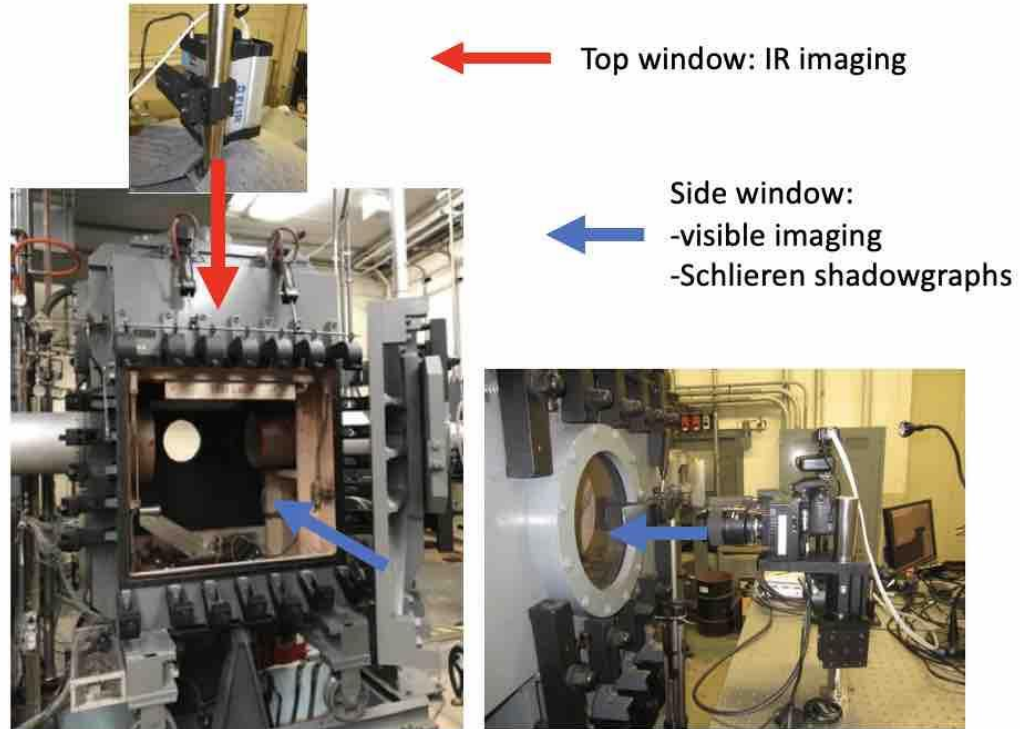


Figure 2.5 Image displaying the top and side window access points into the tunnel test chamber

2.2.1 Side Window Cameras

Multiple imaging systems were mounted for viewing the test models from the side window. These included a commercially available Nikon D610 DSLR full frame camera (6016 x 4016 pixels, 14-bit AD conversion RAW NEF file format), an industrial grade Redlake Megaplug EC16000 (4872 x 3248 pixels, 12-bit AD conversion), and a Phantom Miro M310 high speed camera with a frequency of 3,260 Hz in full frame mode (1280 x 800 pixels, 12-bit AD conversion, with a sensor size of 25.6 mm x 16 mm). Each camera setup served a unique purpose. The Redlake Megaplug was intended as a higher discretization setup that would allow 12-bit analysis in comparison to the 8-bit Nikon JPEG file format. The Phantom Miro was introduced to investigate a high frequency oscillation of the flow that are up to turbulent. The Nikon D610 paired with a Nikkor 200mm f/4 lens systems were used as a baseline method for quantifying optical distortion. A Nikkor 105mm f/2.8 lens as well as another Nikkor 200mm f/4 lens system were paired with

Redlake and Phantom cameras, respectively. With the combination of Nikon DSLR and 200 mm lens, the field of view imaged was approximately 195 x 130 mm at the given distance of the camera to the focused object inside the tunnel of 1.2 meters. Given the sensor size and the field of view, if perfect imaging and focusing is assumed, a theoretical best resolution of 0.03 mm per pixel can be obtained. Theoretical best resolutions for the Redlake and Phantom cameras were also calculated to be approximately 0.07 and 0.14 mm per pixel respectively.

When imaging from the side window using the above setups, the models are to be rolled by 90°. It is assumed that rolling the model has no influence on flow field conditions as geometrically it is in the same orientation to the flow. During the first test campaign, the Nikon and Redlake setups were mounted in parallel and acquired data simultaneously to limit the tunnel operation time. Higher discretization expected from the Redlake camera was intended to confirm and make more accurate statements from what was acquired from the Nikon setup. However, almost immediately there were technical problems which prevented the use of the Redlake camera and very little data was acquired using this setup. In the following, data was collected in JPEG and Nikon's raw NEF file formats to attempt to accomplish the same goal. Although, Nikon's NEF format is not easily readable to post processing software in the native 14-bit unlike the converted 8-bit JPEG images which are standardly read by most imaging post processing software. An attempt to extract the raw 14-bit data is done to verify results.

Wright Patterson had Schlieren setups readily available as a standard facility diagnostic method. Personnel on base agreed to perform high speed Schlieren imaging of the flow around the wedge. These images document all test conditions that were investigated with the other camera setups. While performing Schlieren tests the models were oriented at the nominal condition (towards the top window) and simultaneous data could not be taken with the Nikon system. Instead, IR imaging was performed in parallel to the Schlieren measurements.

2.2.2 Surface Patterns applied to the models

The patterns that were chosen for the first test campaign were composed of several known optical targets with characteristic designs that could define the quality of imaging through the shock flow field structures and singularities. The test targets used in the first test campaign are shown below in Fig. 2.6. The design included a star sector target which is ideal for identifying focusing errors as well as astigmatism, various point sources ranging from diameters of 10 to 500 μm (identified within the green box), a variable frequency resolution target that was expected to measure resolutions on order of 10 LP/mm (identified within the red box), and gridded patterns with point sources in the center (identified within the yellow box). However, after inspection of the laser etched patterns, it was identified that the target included only patterns of variable frequency up to 10 LP/mm and a minimum point source of 50 μm , since limited by the manufacturing process.

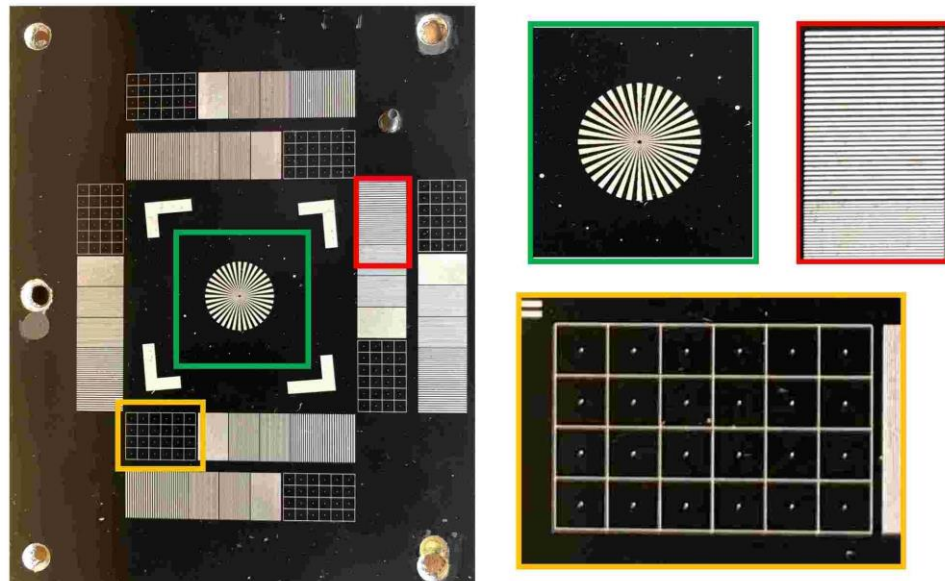


Figure 2.6 15° wedge plate insert used during October 2017 test campaign

While analyzing the data acquired in the first test campaign it was quickly realized that the most useful information was contained in the gridded patterns. Because of these results, the newly designed steel plate inserts to be used during the second test campaign included primarily gridded patterns for analysis complemented through point sources and

5° tilted squares for measurements of point distribution functions and edge response functions, respectively.

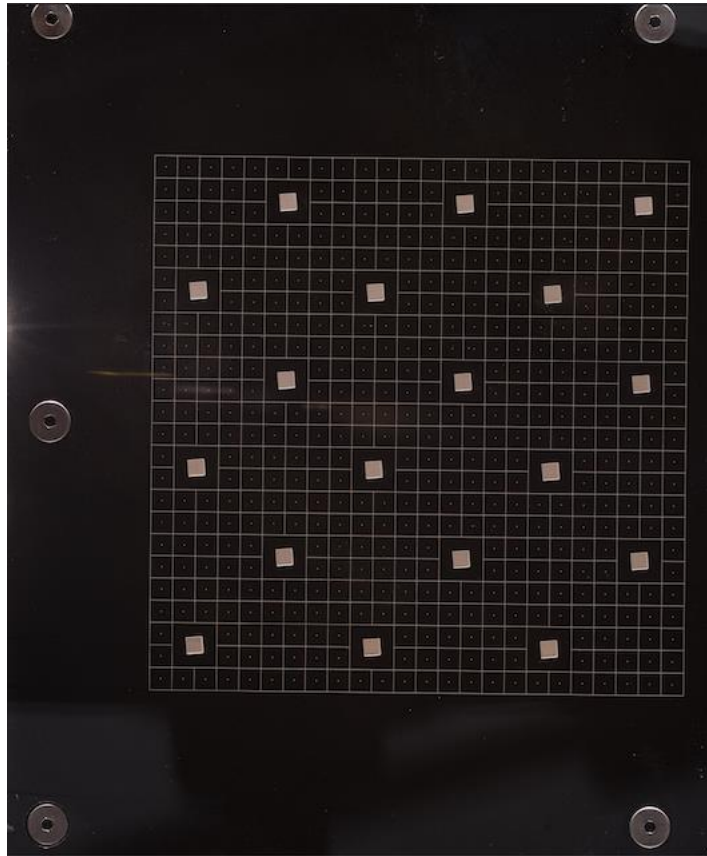


Figure 2.7 15° wedge plate insert, and laser etching used during Feb-Mar 2019 test campaign

Design of the optical patterns on the wedge model was primarily based on manufacturing limitations and what was seen previously with the wedge model. Laser etching complex designs, even that of a tilted square pattern becomes difficult when etching over a curved surface as present on the 7 deg cone. Therefore, only circumferential, and axial lines were chosen to create a similar gridded pattern over the cone surface. Azimuthal lines were etched 120° around the body and extended from near the 10% tip to 8 inches back from where the nose tips attached to the body and were placed 0.25 inches apart from each other. No patterns were etched to the 20% tips as the primary region of interest was seen from 3 inches downstream from the leading tip to the back end of the cone, and the 20% tip was ~ 3 inches in length already. Axial lines were etched over a field

of view of 120° as well every 10° and extended from the first circumferential line on the 10% tip to the furthest downstream radial line on the cone body.

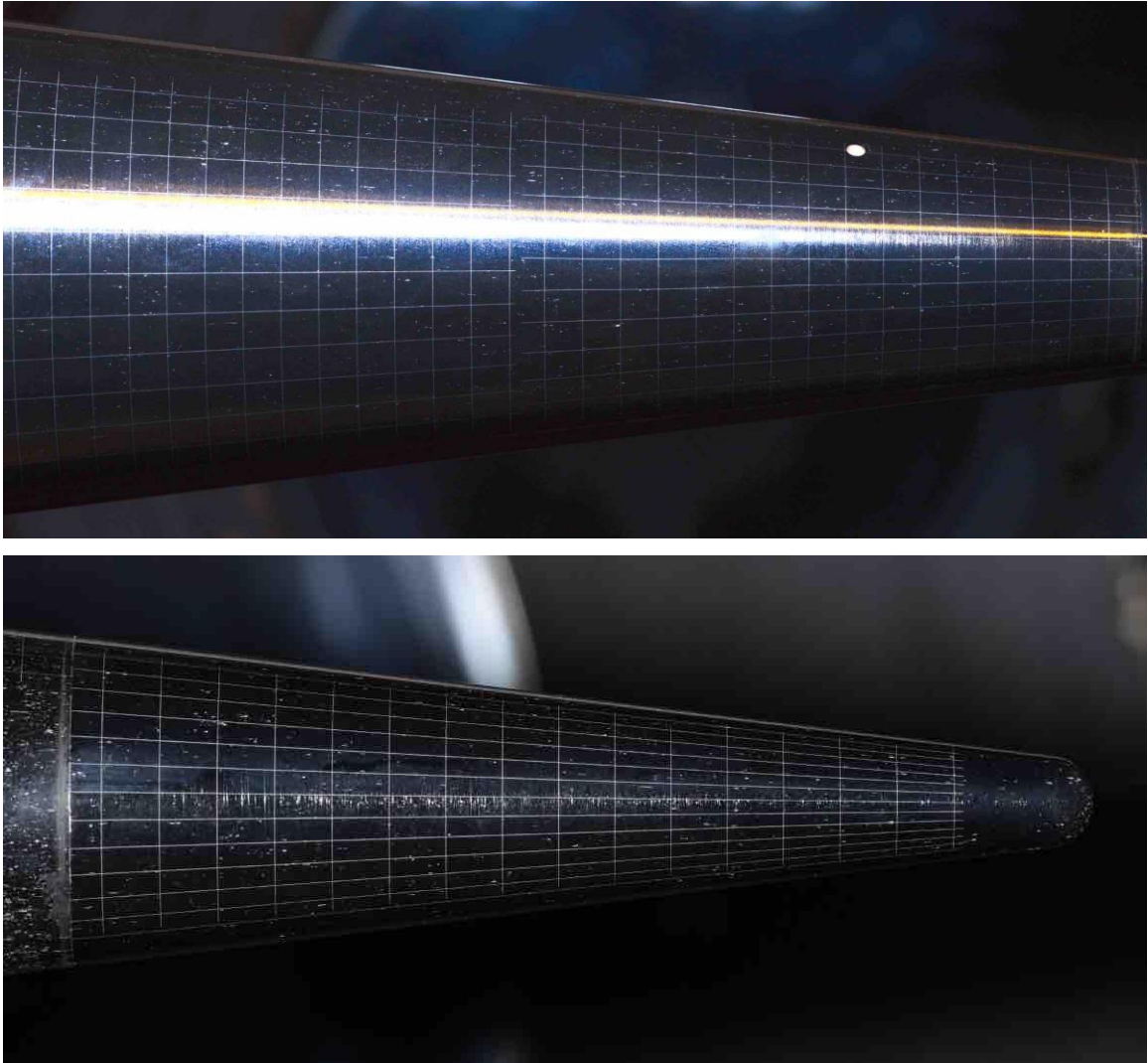


Figure 2.8 7° half angle wedge cone body and 10% tip etching

2.2.3 *Spectral Sensitivity of the Nikon D610*

When the Nikon array converts the raw file format to an 8-bit JPEG information on sensitivity in each of the red, green, and blue (RGB) color spaces can be performed. The spectral sensitivity of the Nikon 3 color channel pixels was analyzed using a calibration lamp and a lab spectrometer which provided monochromatic light between 400 and 1000

nm. The results presented are for a manual white balance temperature setting of 5560 K and show the spectral efficiency of the RGB pixels corrected for the spectrometer grating.

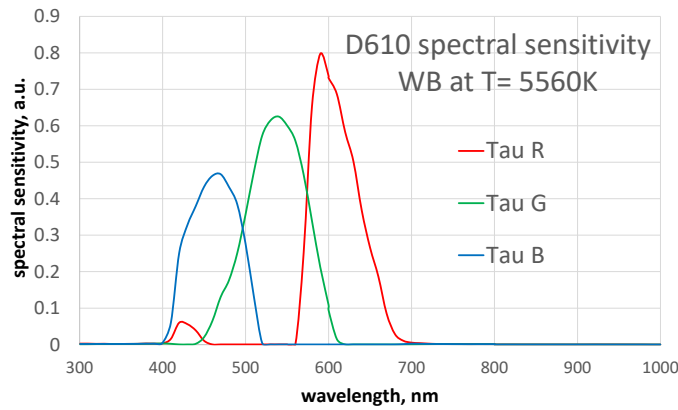


Figure 2.9 Spectral sensitivity of the RGB converted pixels for a Nikon D610 at a White Balance (WB) of 5560K

2.2.4 IR imaging

The IR camera used was provided by the University of Kentucky’s Institute of Research for Technology Development (IR4TD). A FLIR SC4000 series camera (320 x 256 pixel, 14-bit counts per pixel) was used which was sensitive in the 3.0 – 5.0 μm range. The setup was paired with an available 25 mm lens system which at our focusing distance offered a field of view of approximately 10 x 8 inches (250 x 200 mm). This imaging was done from the top window port looking into the test section and was often done simultaneously with other side window imaging setups such as Schlieren and wavefront distortion measurements. IR Imaging of the models was done at nominal orientation with the wedge pitched at 0, -5, -10, and -15 degrees whereas the cone was pitched at -4, 0, and 4 degrees. The IR imaging experiments were conducted to gather information of the transition locations from laminar to turbulent flow. A transition location could be identified by an increased heat load present from the turbulent boundary layer that would be detectable in the IR images.

Initial measurements with the IR camera in both test campaigns were conducted to gain information on calibration settings to convert the camera counts to a temperature distribution. This was done with blank anodized aluminum and black zinc coated steel plates that had the same coating as the etched plates used in each campaign. For the cone,

calibration with the black zinc coated steel plate can be used since the surface finish is the same as the steel plates. The plates were positioned inside the tunnel at the model location in the test section, therefore covering all effects on detected surface radiation in the optical path. Multiple thermocouples were adhered to the top surface of the plates while the underside was heated with a low power heat gun. Simultaneous data of the IR counts, and temperatures were collected while the plates were heated from room temperature to an expected test temperature of approximately 100° C. From these measurements, a direct correlation between surface temperature and IR signals was derived. A black optical plate positioned in the tunnel for calibration measurements as well as the derived temperature profiles using this method for the wedge and cone test models are displayed below.

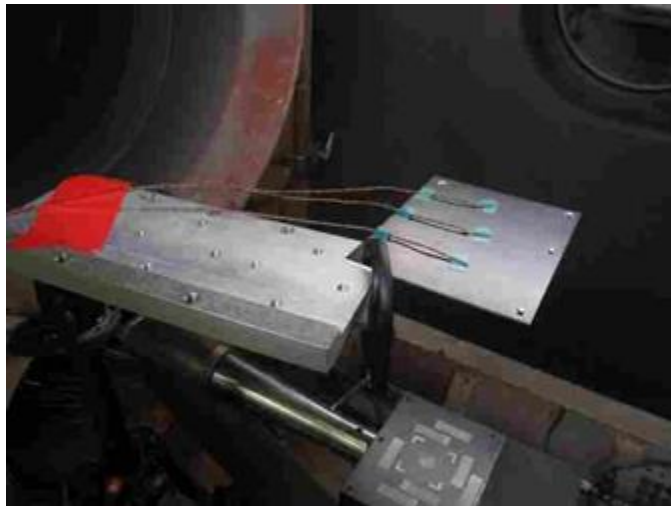


Figure 2.10 A black plate without laser etching positioned that the test height inside of the tunnel with 3 thermocouples attached at the surface

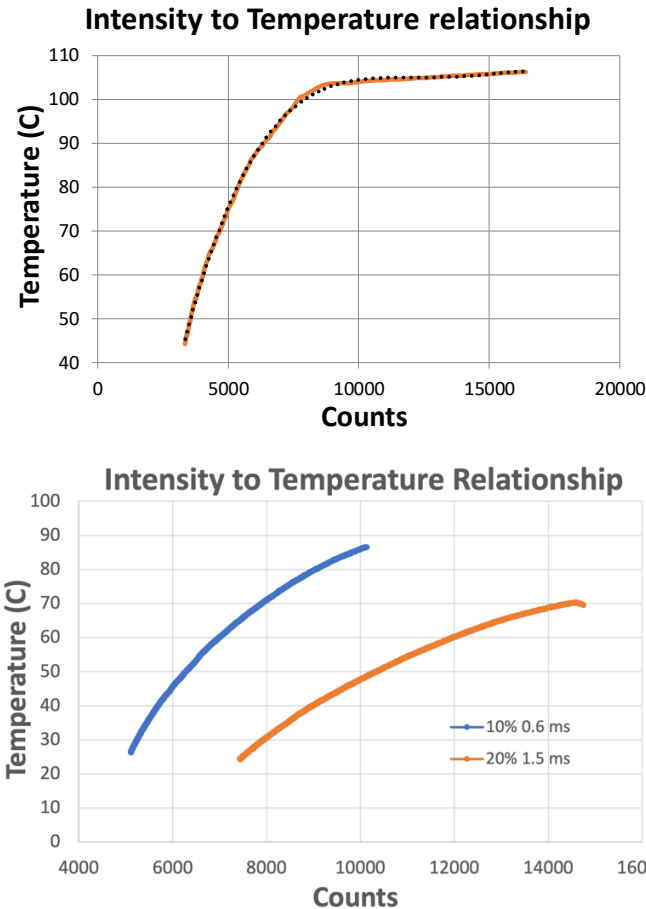


Figure 2.11 Calibration curves from the thermocouple experiments for the wedge (above) and cone (below) with the 10% and 20% tips

2.3 Test Matrices

For the first test campaign three pressure conditions were chosen across the range of capabilities of the facilities of 900, 1400, and 1900 PSI. A constant reservoir temperature was selected at 1000° R (282.4° C) as tunnel personnel suggested that varying temperature would not alter flow field conditions significantly. For each pressure condition, angles of attack were chosen for the wedge to be 0, -5, -10, -15 degrees. Each measurement condition was tested using combinations of imaging setups discussed earlier, such as IR imaging and Schlieren or Nikon imaging with different illumination methods to vary acquisition times. During this test campaign 3 illumination methods were identified for use. These included halogen tube lighting mounted inside of the tunnel, a commercial Nikon SB-700 camera flash, and a high powered Balcar 6400 Xenon Flash system. Flash durations for the Balcar

system were measured at the lowest (3.0/3.0) and highest (8.0/8.0) power level giving a range of available flash duration times that could be used to illuminate the test probes. These measurements were performed using a Thorlabs Avalanche detector ADP1 paired with a digital Tektronix oscilloscope with measurable frequencies up to 1 Ghz. The short flash duration of the Balcar Xenon flashed provided a system in which we could clearly go beyond the time scales of vibration as discussed later in Chapter 3.4, but not sufficiently low to resolve turbulence effects.

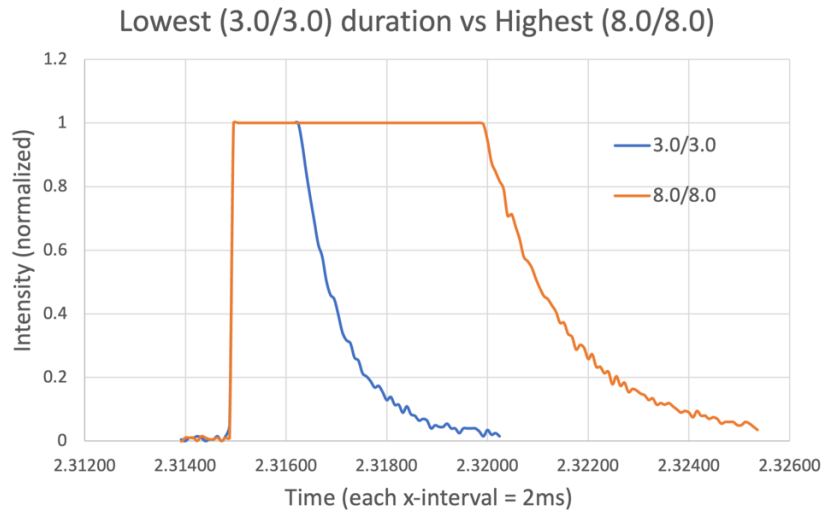


Figure 2.12 Balcar 6400 Xenon Flash lamp flash durations measured at the lowest and highest power levels

Continuing into the second test campaign, similar parameters were chosen, but given the increased number of test models, most of the conditions at 1400 PSI pressure were considered lower priority and eventually dropped to be able to capture data at the two extreme ends of the pressure range. Still, the wedge was tested over all four angles of attack in the second campaign. For the cone model, different angles of attack were chosen based on previous analysis performed with that cone. WPAFB had run the cone at all angles of attack between -4 and 4 degrees in 1-degree increments. The plan for the cone model was to run at -4, 0, 4 degrees angle of attack (AoA) to capture the extreme ends that had already been tested. A complete table of all testing run during the 2 experimental campaigns can be found below in [APPENDIX 1. TEST CAMPAIGN PROTOCOLS].

2.4 Vibrational Analysis

The desired optical distortion to be measured originates from blurring of the optical patterns on the model while inserted into the flow. This blurring would be a result of aerodynamic effects through boundary layer and shock structures measured as the difference between images taken before and during tunnel operation. However, during tunnel operation there are significant vibrations present from the mechanical loads due to the flow and from the gas flowing through the feeding structures which are even experienced from inside of the control room away from the tunnel. These vibrations could then influence the test model and optical table that the camera setups were mounted to. The oscillations experienced would cause both model and cameras to physically move and therefore cause blurring of the optical patterns by physically exposing the camera sensor a “smeared” profile over the acquisition setting.

This problem was realized during the first test campaign. Following our data collection, vibrational measurements were collected by WPAFB personnel using a tri-axial accelerometer that was mounted inside the wedge probe and 2 uni-axial accelerometers that were mounted outside of the tunnel at the end of the Nikon camera lens far from the camera body. These locations were anticipated to provide the largest displacement amplitudes experienced outside of the tunnel. The accelerometer was sensitive between ± 50 G with signal response in the X (axial), Y (vertical), and Z (lateral) directions of 100.4, 100.6, and 98.3 mV/G respectively. The Nikon accelerometer had a sensitivity between ± 500 G with a signal response of 9.27 mV/G. Data acquisition rates of both accelerometers were at 30 kHz over a scan time of 7 seconds. The gathered data therefore contains information between 0.3 and 15 kHz if the Nyquist limitation for the maximal measurable frequency of half the detection frequency is considered [12]. Fig. 2.13 shows the tri-axial accelerometer that was mounted inside of the wedge probe and mounted in tunnel for vibrational analysis from flow.

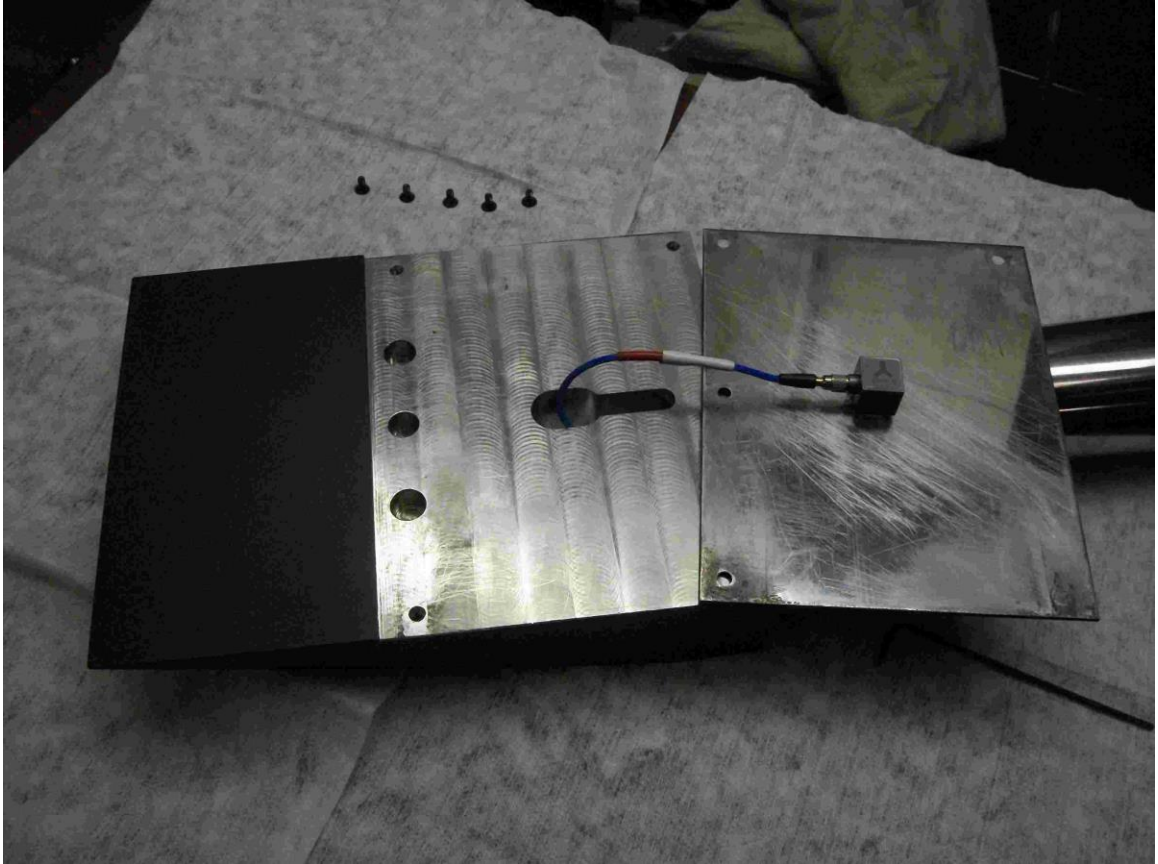


Figure 2.13 Image of the 15° wedge probe illustrating the location and mounting of the tri-axial accelerometer to the insert plate

CHAPTER 3. FLOW FIELD DATA ANALYSIS

The observed flow structure for the wedge and cone models were analyzed to support results of the imaging analysis. These flow structures were observed with the Schlieren, IR measurements as well as wavefront distortions to better understand what is gathered from the visible imaging. The shock structures observed will be presented to describe the general flow boundaries experienced from both the wedge and cone model. Also, the IR measurements will be displayed to show potential transitions from laminar to turbulent flow regime, with the cone model having pre-existing transition measurements from AFRL. These transition locations as observed from an increased heat load will be compared to the already existing data. Lastly, wavefront distortion measurements performed alongside the imaging campaign, and provided by AFRL personnel will be discussed.

3.1 Flow Field Analysis from Schlieren

Schlieren imaging of the shock structures generated by the wedge and cone models were done using a Photron Fastcam SA-Z Type 2100K (maximum resolution 1024 x 1024 but could be scaled) at all pressure and angle of attack conditions that were investigated for optical distortion. In Fig 3.2 Schlieren shadowgraphs of the wedge model are shown for all selected pressure and angle of attack conditions. An oblique shock is generated at the leading edge of the wedge model and a bow shock at the cone model tip. Given the resolution of the Schlieren imaging, oblique shock angles cannot be identified with greater uncertainty than 0.5° . The wedge shock can be used as a calibration for the Mach number of the wind tunnel using the Theta-Beta-Mach relation. From this, the Mach number of the tunnel was measured to be ~ 5.8 , which agrees well with the nominal condition of the tunnel.

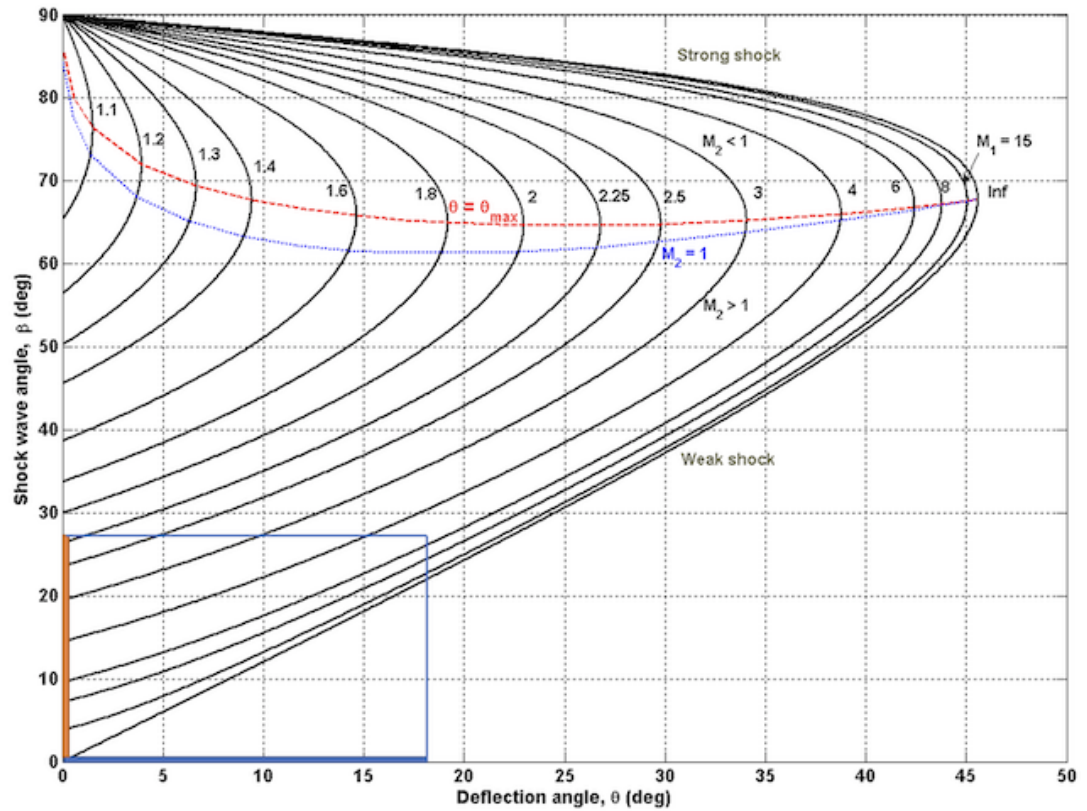
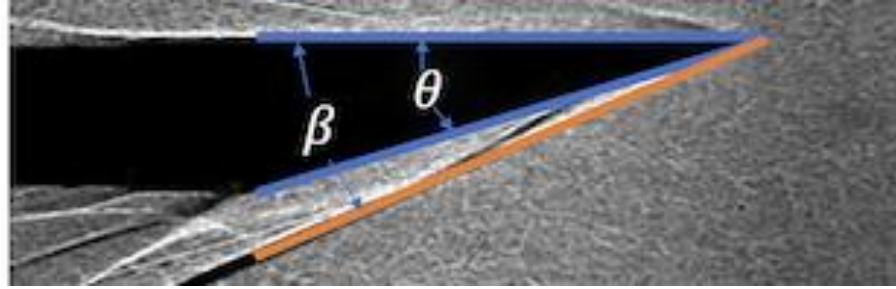


Figure 3.1 Theta-Beta-M relation curve with the measured deflection and shock wave angles showing the measured tunnel Mach number at ~ 5.8

For both models there are secondary weaker shocks that form downstream of the leading edge due to imperfections in the surface as well as the coupling location for the plate inserts and interchangeable tips. The strength of the primary shock was observed to be positively affected by increasing angle of attack and reservoir pressure. Because of symmetry of the flow over the models, shock structures for 2 different AoAs can be observed simultaneously. When the model is placed into flow at an AoA of 0° , the upper surface shows the shock structure for this condition while the bottom surface shows the shock structure at -15° . Correspondingly, when the model is placed in flow at -5° for the upper surface, the lower surface would show the shock structure for the -10° condition.

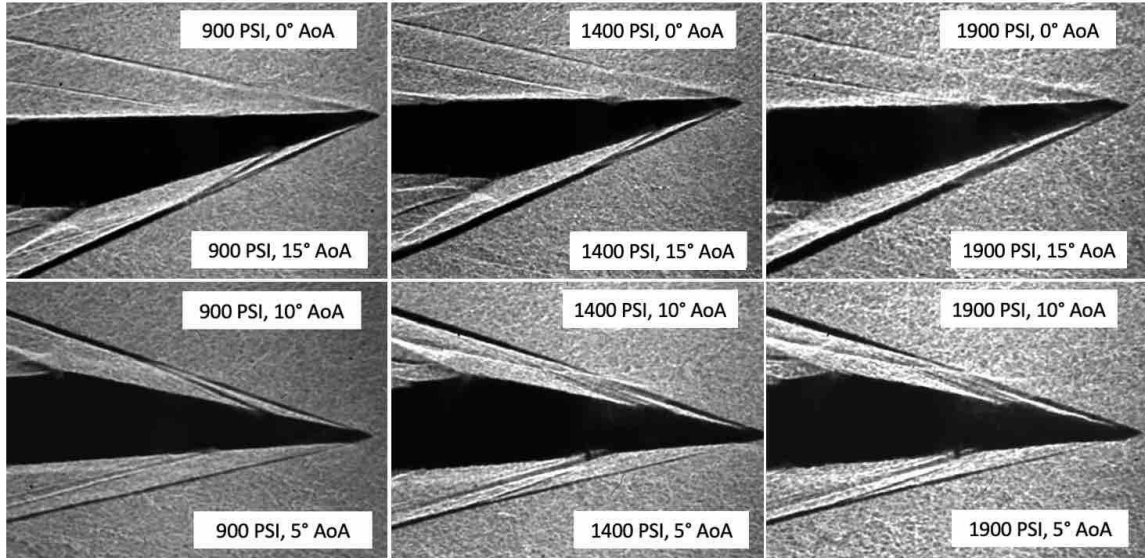


Figure 3.2 Schlieren shadowgraphs for the 15° wedge probe over all AoA and reservoir pressures.

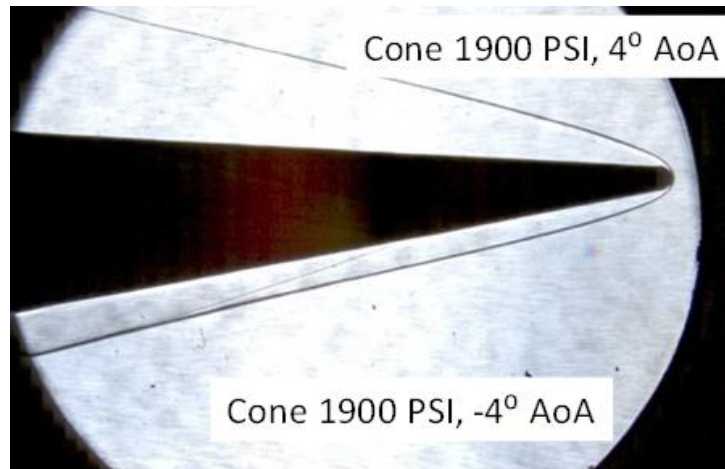


Figure 3.3 Schlieren shadowgraphs for the 7° half angle cone with the 10% attached tip at different angles of attack

During the first test campaign it was also investigated to disturb the flow over one side of the wedge model by introducing a cylinder (#4-40 screw) jutting from the plate surface. The main objective was attempting to force a transition to turbulence behind the obstruction and would locally create an additional shock structure. This would be anticipated to show locally additional optical distortion if the shock structure would be major source for such distortion. Analysis of symmetric locations downstream of the wedge with and without the additional flow obstruction was done.

3.2 IR imaging of the wedge model

The calibration curve to relate the infrared counts to temperatures was obtained with blank black plates that had not been etched with optical patterns. Analysis of the wedge probe was done using selected streamlines on either side of the optical plate that did not have influence of the laser etched surface patterns. The surface patterns would have significant difference in IR sensitivity as the calibration curves were calculated from the black anodized aluminum surface. These streamlines provided information from the attached leading edge of the optical plate to the back edge. This was done to hopefully provide information on transition locations from laminar to turbulent boundary layers, which would be seen in the thermal images as an increase in thermal load and consequently increased surface temperatures from the turbulent boundary layer. These data would be used alongside the visual Nikon data to investigate any influence that turbulent boundary layers may have on the observed optical distortion. In Fig. 3.4 an example of an IR still image of the plate at 1900PSI and 15° is shown, displaying the left and right streamline profiles that were extracted for investigation.

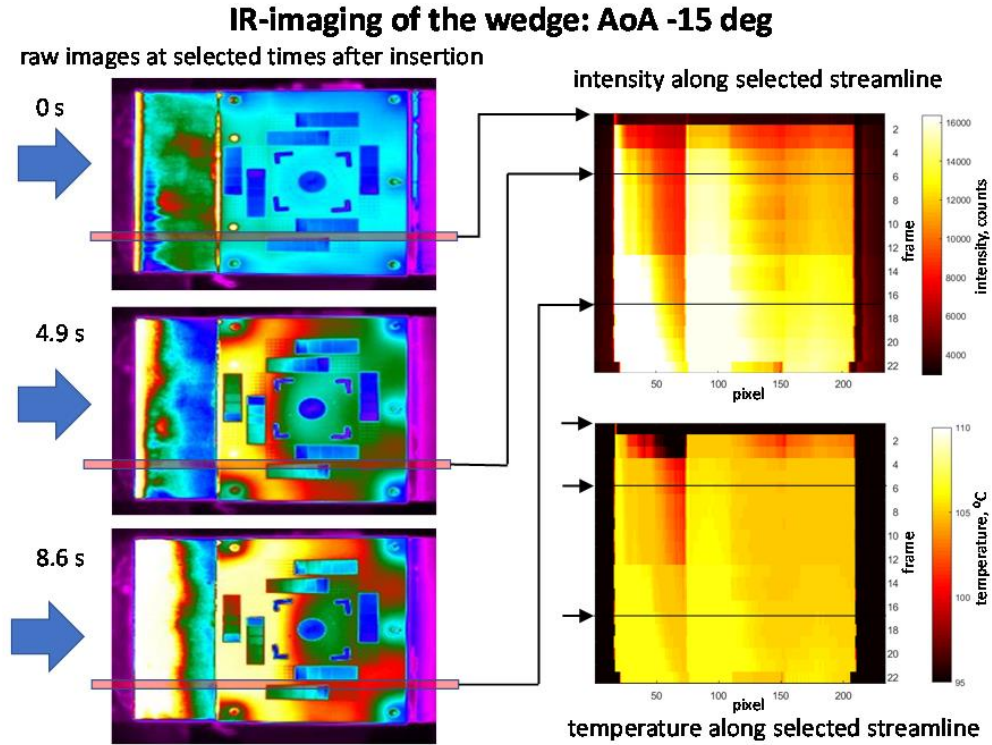


Figure 3.4 Raw IR at 1900PSI and 15° angle of attack at different times showing the extraction method of intensities and temperatures for a selected streamline

It was quickly observed that the temperature distributions extracted of the left and right streamlines over time did not depend on the side they were extracted from indicating that the left and right streamlines provided very similar information. Therefore, only the right streamline was used for analysis. A minor variation in the field of view for the optical plate with varying angle of attack was generated since the plate would be closer or farther from the focusing distance depending on if the wedge model was angled toward or away from the camera. Thus, even with the camera mounted securely to the top tunnel window and the images being refocused between changing angles of attack, the pixel locations for the streamlines would vary slightly for each angle of attack. To automate the process of determine the temperature distributions of the streamlines from the IR images a 5-pixel spread between the variable line frequency and gridded patterns were extracted. The maximum value of the 5-pixel spread was then selected to be the recorded temperature at that location, since it was observed that the optical patterns provided much lower values than the black anodized surface and were discarded.

Further analysis involved investigating the streamline temperature distributions more closely for different times in the test. Over the test time the temperature on the plate continues to increase. The surface temperature was monitored in real time during testing and the wedge would be ejected from flow when these temperatures reached the maximum of the calibrated range, which was around 100 °C. To compare intensity and temperature profiles at different times of the flow normalized profiles were generated to attempt to monitor flow field transition during the test.

For all test conditions the normalized profiles are in good qualitative agreement with one another when compared to the beginning, middle and end test streamlines for varying reservoir pressures as shown in Fig. 3.5. However, there was a noticeable dependence on the angle of attack. Mostly, higher angles of attack show an almost uniform distribution from the leading edge of the optical plate, with even a decrease from the peak intensity from the upstream edge of plate. For the test condition of 5° angle of attack, displayed in Fig. 3.6, there was a trend to see an increasing heat load downstream of the edge of the plate, and for increasing reservoir pressures, tended to occur more upstream. This increase in heat load might indicate a transitioning location on the plate ending downstream in a turbulent flow.

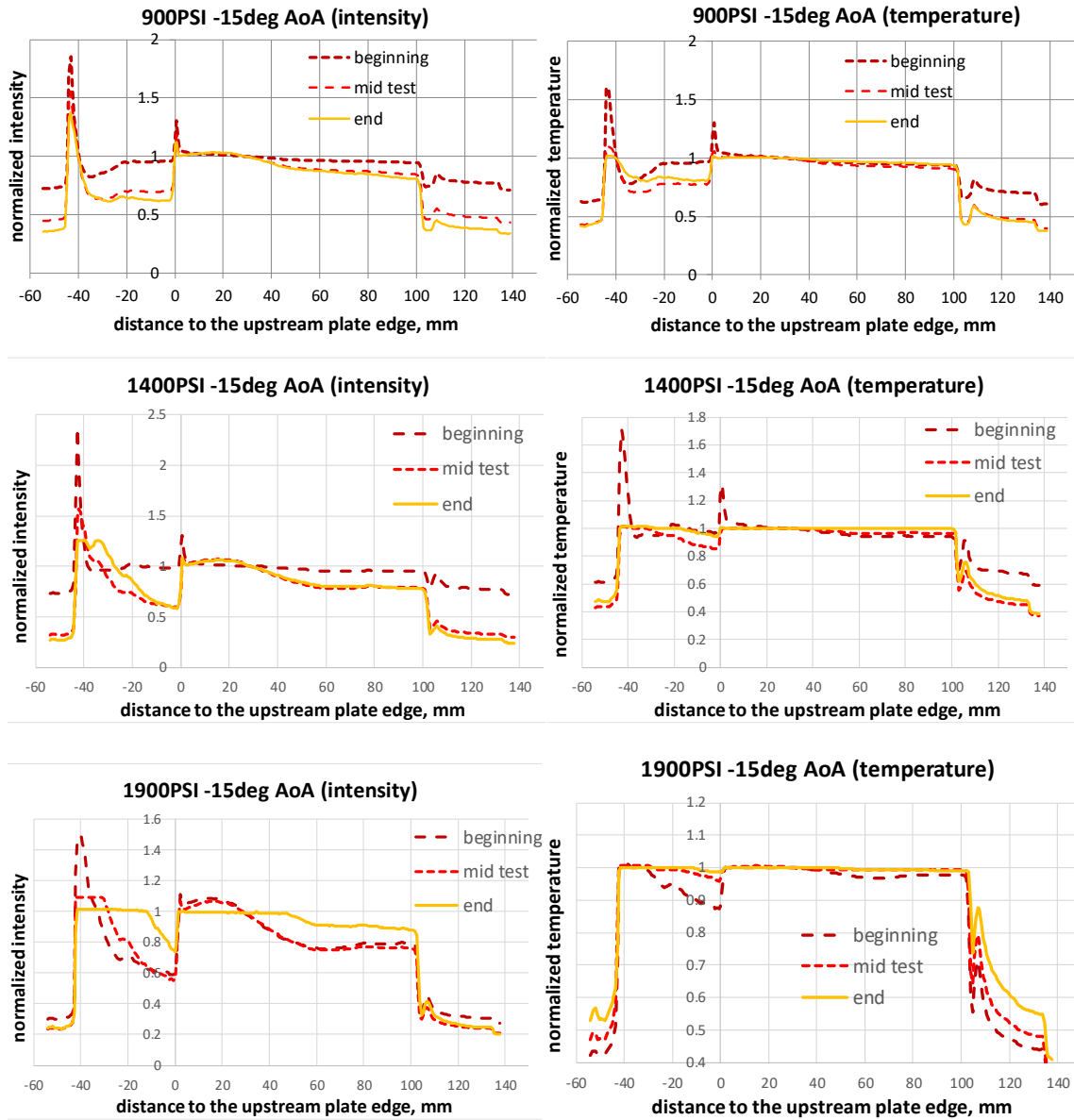


Figure 3.5 Normalized intensity and temperature profiles for extracted streamlines at beginning, middle and end test for 15° angle of attack over all 3 reservoir pressures.

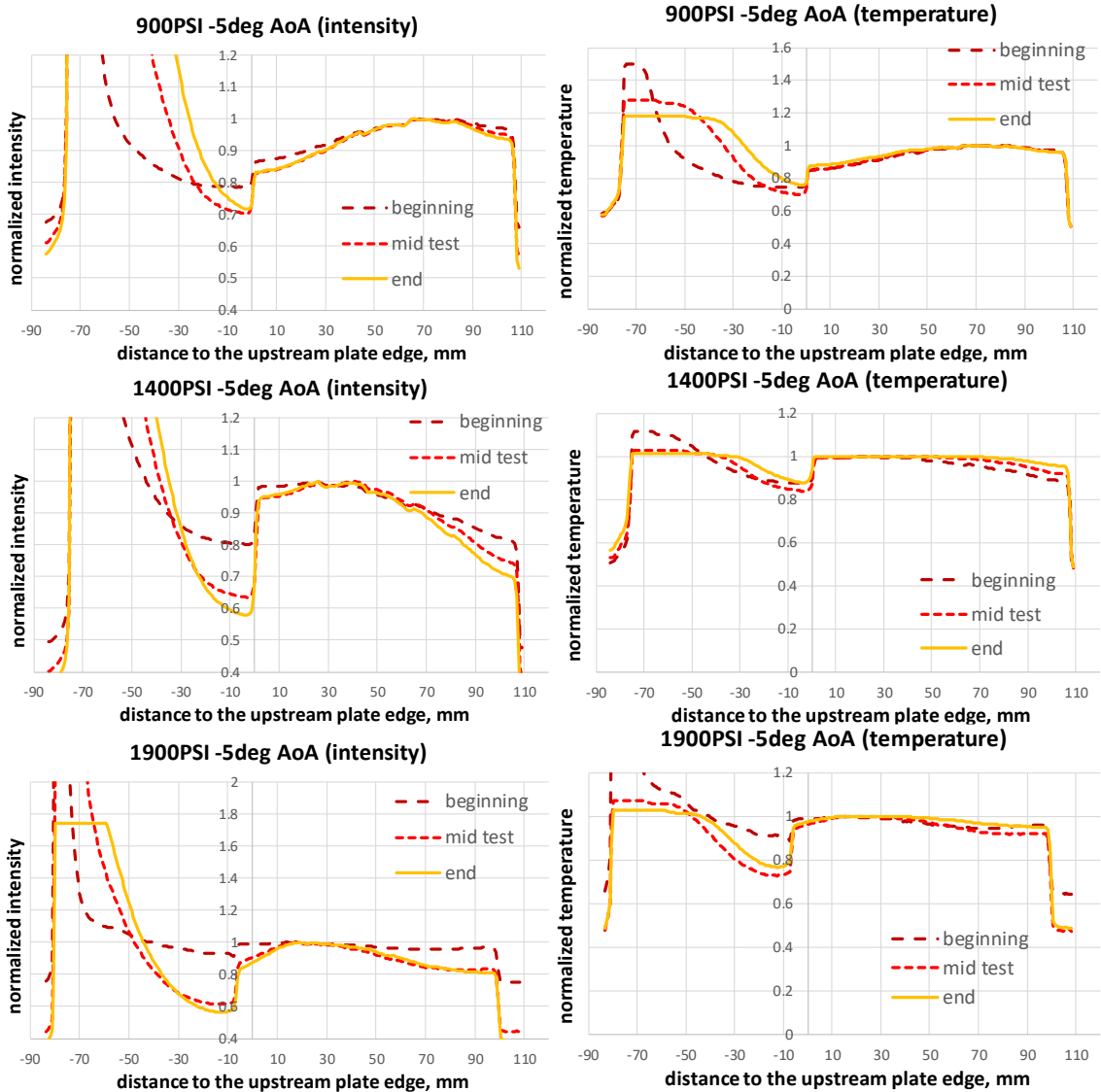


Figure 3.6 Normalized intensity and temperature profiles for extracted streamlines at beginning, middle and end test for 5° angle of attack over all 3 reservoir pressures.

3.3 IR imaging of the cone Model

Fig. 3.7 shows raw IR images of the 10% cone tip model at all reservoir pressures and 0° angle of attack. On the cone surface there is a clear heat load increase at 10.5, 9 and 7.9 inches downstream of the cone tip for reservoir pressures of 900, 1400 and 1900 PSI respectively. The earlier data with a geometrically identical cone model fitted with thermocouples on the surface yielded a similar temperature jump location. The results from

the earlier data are in good agreement and are presented and compared to our transitional locations in Fig. 3.8.

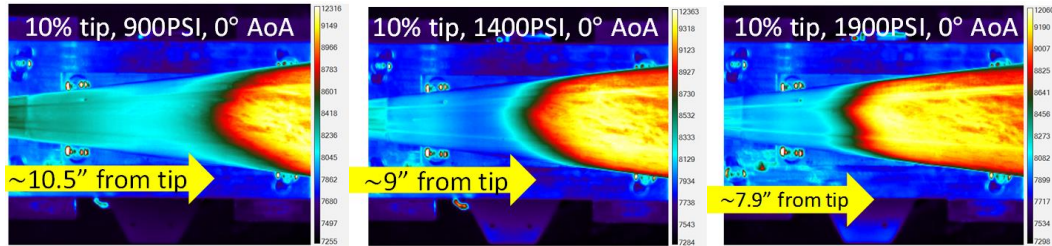


Figure 3.7 Raw IR images of the 10% cone tip over all 3 reservoir pressures

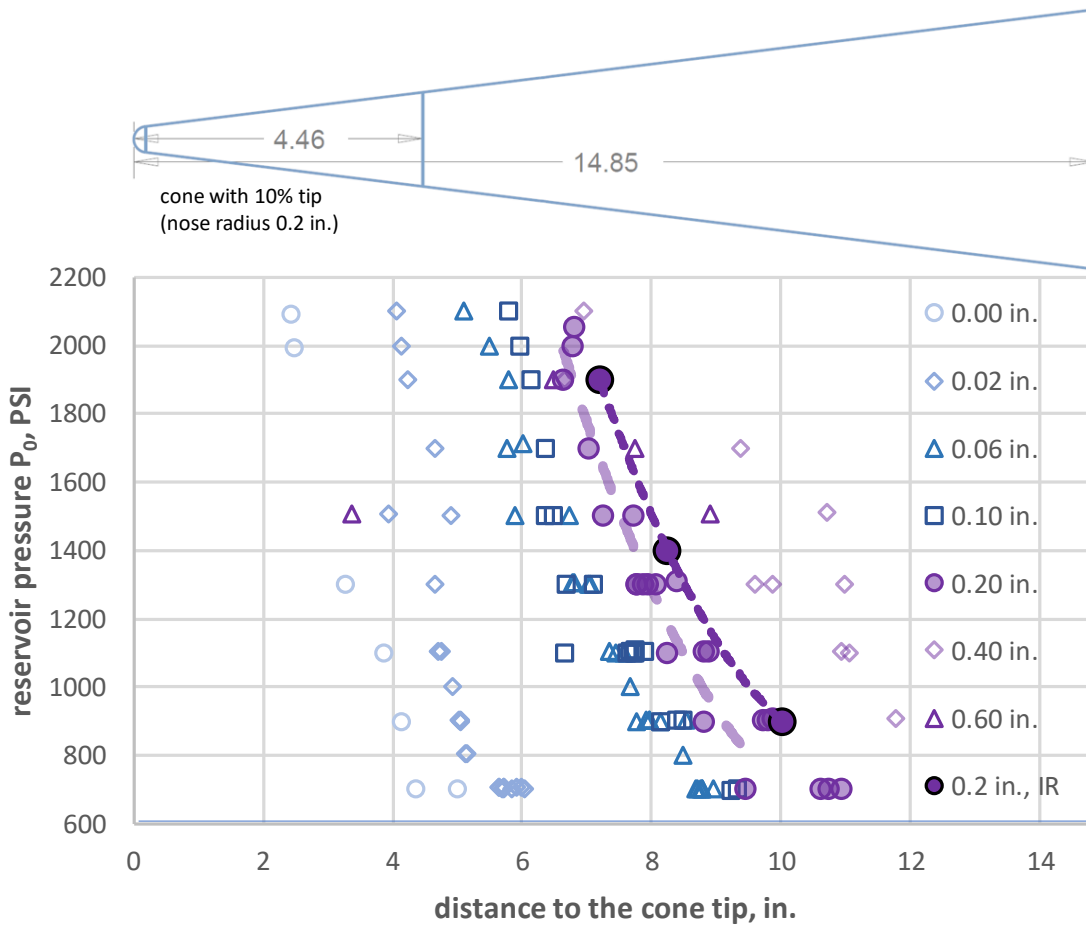


Figure 3.8 Comparison of transitional locations observed from WPAFB [3,8,9]

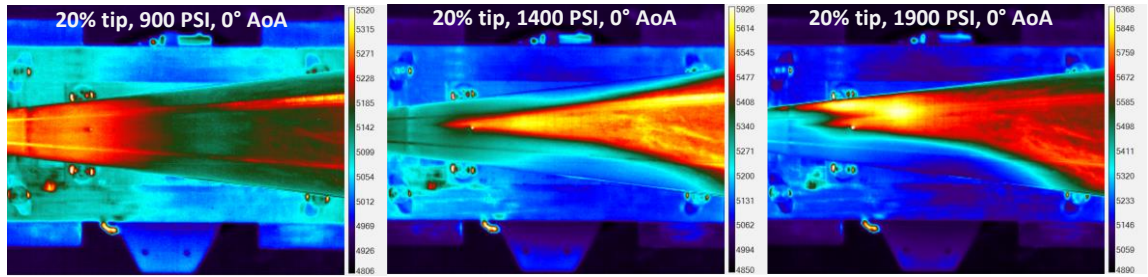


Figure 3.9 Raw IR images of the 20% cone tip over all 3 reservoir pressures

Fig. 3.9 shows raw IR images of the 20% cone tip model at all reservoir pressures and 0° angle of attack. There is no evident increased heat loading at 900PSI as illustrated in the leftmost image above. For the higher two pressure, 1400 and 1900 PSI, there is an increase of surface temperature, but this is interpreted as a trip in the flow that is not natural. Initially, the pressure port (seen as a small bright yellow circle close to the upstream heat increase) was thought to have caused a disturbance in flow. Now it is thought that maybe a slight step was present at the tip attachment that cause the disturbance in the flow which resulted in an unexpected transition.

3.4 Vibrational influence on the Imaging

Vibration effects during flow operation were investigated for the wedge probe to account for potential deformations of the point and line profiles of the optical patterns on the plate. The data were taken for influences observed inside and outside of the tunnel on the test probe and cameras systems, respectively. Again, these data were taken after the optical test campaign by WPAFB personal using the tri and uni-axis accelerometers discussed earlier in Chapter 2.4. During these measurements, the uni-axial accelerometers were setup in two configurations to determine the vibrational influence on the camera setups in the horizontal and vertical directions respective to the CCD array. No investigation outside of the tunnel was performed along the optical axis of the camera to the object as this would not be expected to cause the vibrational deformations that we were interested in. To catch these deformations, displacement data had to be extracted from the measured acceleration. Ideally, there is a direct correlation of acceleration measurements to displacements by numerically integrating the acceleration data twice. When this method was applied to the measured accelerometer data a monotonous increase in the displacement

was observed over several period of oscillations up to unphysical displacements of several centimeters.

Instead, the accelerometer measurements were processed in the Fourier space using a built-in function in MATLAB to perform a FFT (Fast Fourier Transform). The accelerometer data acquired was measured in G's at a sampling frequency of 30,000 Hz (30kHz). The values measured were converted to a [m/s²] unit by multiplying each value by 9.81 before any analysis was done. Once the data was processed by MATLAB's FFT function it shows a double-sided mirrored curve for the amplitudes at given frequencies between -15 to 15 kHz based on the maximum accurate Nyquist frequency from the 30 kHz sampling rate [12]. The negative frequencies are not physical and just represent symmetric redundant information of the positive frequencies. The actual Fourier curve that we are interested in then is the single sided spectrum which is obtained from only the positive frequencies and twice those amplitudes. The amplitudes are doubled because the redundant information from the negative frequency space should be present in the overall data.

The acceleration data that was processed and converted to a physical single sided spectrum in Fourier space was then converted into displacement data based on equations of simple harmonic motion and their displacement, velocity, and acceleration relationships. Assuming a sinusoidal motion, the equation for the displacement can be described as

$$d(t) = d_0 \sin(2\pi ft) \quad \text{Eq. 2}$$

where d_0 and f are the peak displacement and the frequency in Hz of the displacement, respectively. Velocity and acceleration relationships are determined by taking the first and second derivative of the displacement equation with respect to time t .

$$v(t) = \frac{d}{dt} d(t) = d_0 2\pi f \cos(2\pi ft) \quad \text{Eq. 3}$$

$$a(t) = \frac{d^2}{d^2t} d(t) = -d_0 (2\pi f)^2 \sin(2\pi ft) \quad \text{Eq. 4}$$

If we recall, currently we have vibrational acceleration data of the wedge probe model and the cameras in Fourier space. The second derivation of displacement is acceleration and from what we have just derived we can see that our definition of

acceleration could simply be written as a function of the initial displacement. In other terms, it can be defined to convert our acceleration data into displacements in Fourier space by dividing all data points by $-(2\pi f)^2$.

$$a(t) = -(2\pi f)^2 d(t) \quad \text{Eq. 5}$$

Similar to the MATLAB built-in FFT function, there is also a reverse process built in to convert Fourier space frequency data back into the time domain. This process in MATLAB is the inverse Fast Fourier Transform (iFFT). These displacement data could then be used to determine theoretical Point Distribution Functions (PDF) and Line Distribution Functions (LDF) curves that would result from the vibration of the wedge alone. That is, a theoretical broadened curve from a single line from our gridded optical patterns when affected by vibrational displacements over the test time.

Before the inverse transformation was performed in Fourier space it was investigated which frequencies would cause significant vibrations to the test model. From this, a decreasing amplitude curve with frequency was used and it was determined that vibrational frequencies above 10 Hz at 900 and 1,400 PSI conditions, as well as 40 Hz at 1,900 PSI have displacements on order of less than $1\mu\text{m}$. Line widths of the optical patterns were on order of $\sim 30\text{-}50\mu\text{m}$ depending on which patterns were used so the vibrations above 10 Hz are found to be negligible. On the other end of the spectrum at frequencies lower than 1 Hz, monotonously increasing displacement values with decreasing frequencies up to unrealistic values of more than 1mm was seen. These unphysical results are explained with a decreased sensitivity of the sensors which were designed for high frequency operation up to 30kHz. Fig. 3.10 shows curves of the displacement of the wedge probe at 900 and 1,400 PSI conditions in the directions of interest, as well as the cameras response in vertical and horizontal directions.

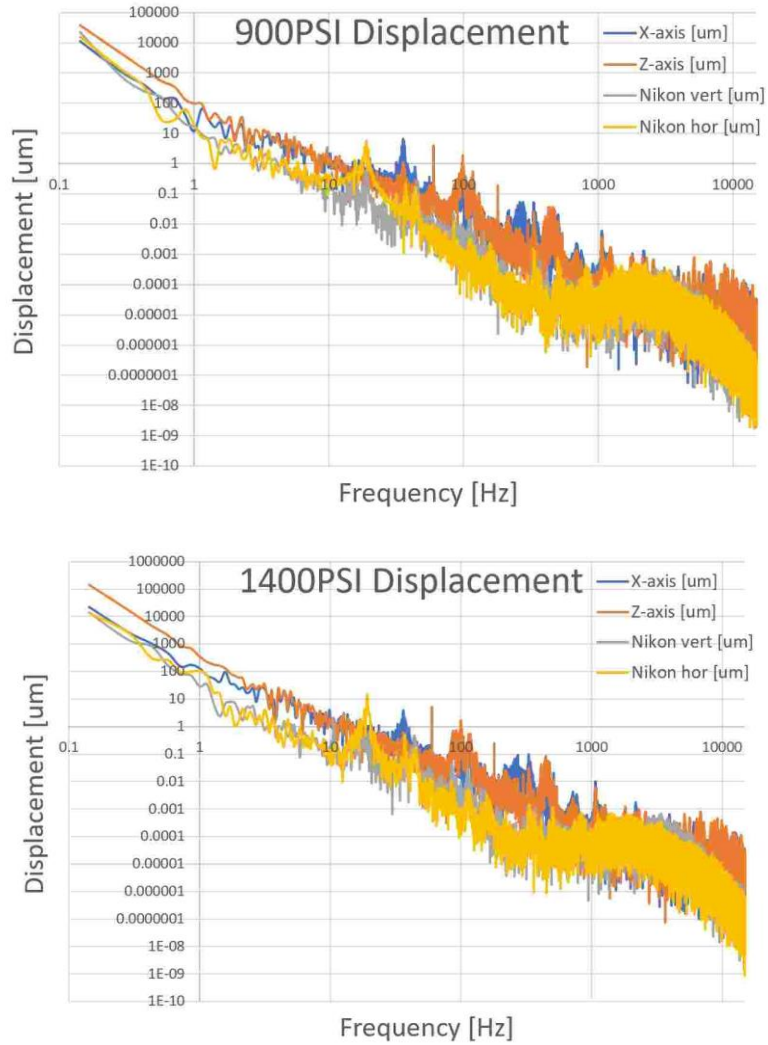


Figure 3.10 Measured displacement of the wedge probe at 900 and 1400 PSI reservoir pressure in the axial (X-axis) and perpendicular (Z-axis) directions to flow. Vertical and Horizontal displacements are measured at the camera lens end.

Spatial information was determined by superimposing all sine functions determined from all frequencies up to 300 Hz over each time step. From the frequency data already determined from the inverse Fourier transform we can see unphysical amplitudes of several millimeters in the range <5 Hz. To investigate these influences, high pass filters during the inverse Fourier process were introduced at 0.7, 1, and 3 Hz. The high pass filters as these cutoff ranges would show the influence of vibrations at low frequencies.

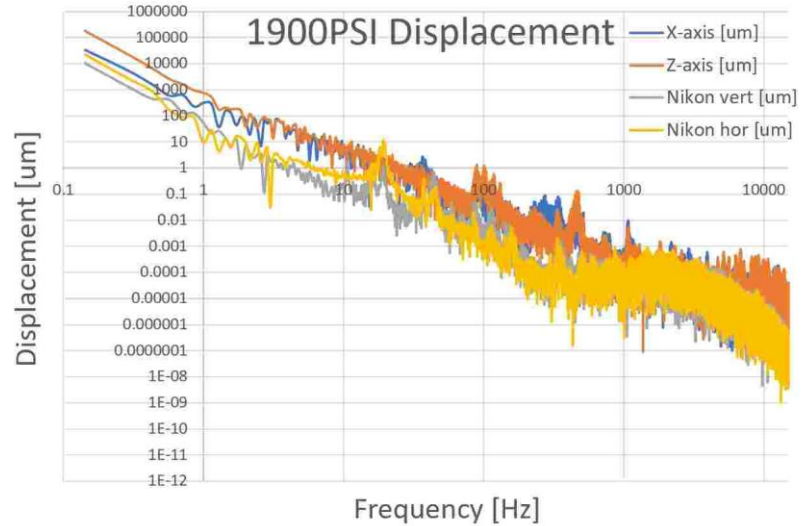


Figure 3.11 Measured displacement of the wedge probe at 1900 PSI reservoir pressure in the axial (X-axis) and perpendicular (Z-axis) directions to flow. Vertical and Horizontal displacements are measured at the camera lens end.

It was observed that there was a greater influence on vibrations parallel to the flow, the “vertical line profiles” when compared to those perpendicular, “horizontal line profiles”. This is intuitive as the force load of the flow from the nozzle would primarily be coupled to the axis parallel to the flow. Vertical and horizontal LDFs were extracted over the grid patterns to confirm the greater vibrational influence in the direction that was expected. From this, data analysis for the wedge probe during the first and second test campaign primarily focused on the gridded line patterns. From these patterns, Line Distribution Functions (LDFs) were extracted at multiple positions on the plate to investigate distortion. It is important to note the nomenclature for how vertical and horizontal LDFs are defined. Vertical lines on the plate produce horizontal LDFs (vibrational effects parallel to the flow) while the horizontal lines on the plate produce vertical LDFs (vibrational effects perpendicular to the flow). Fig. 3.12 illustrates the method by which the LDFs are identified.

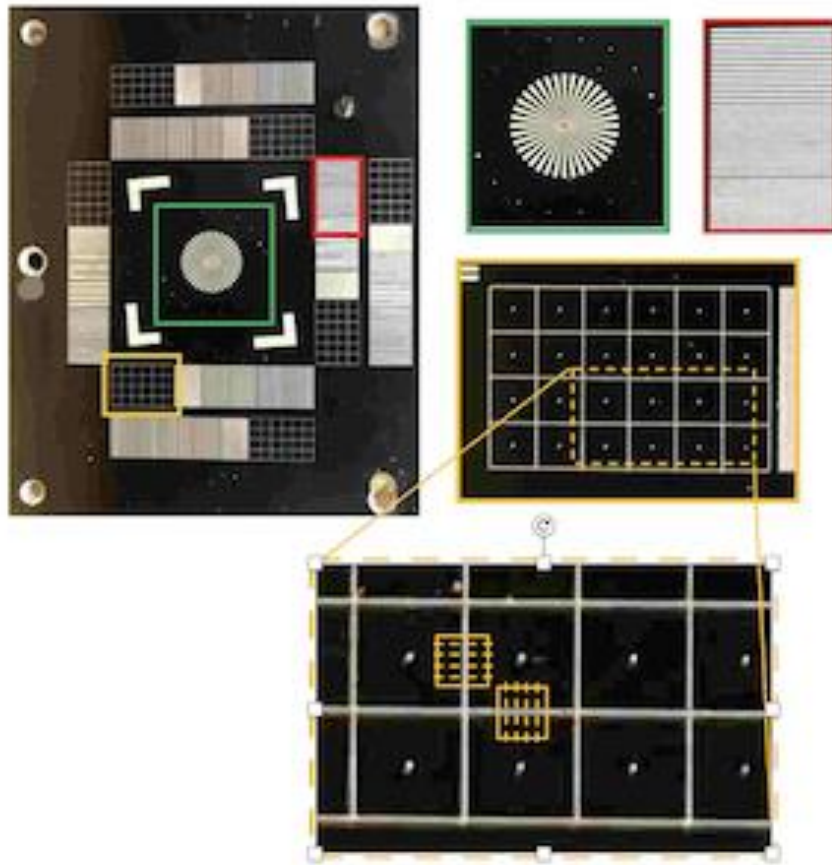


Figure 3.12 15° wedge probe with plate inserts showing the vertical and horizontal LDF extraction method over all lines inside of the yellow pattern

The initial test campaign was faced with limited illumination options and an acquisition time of 1/6 seconds for the Nikon imaging was necessary to provide proper lighting of the etched patterns. Although, from what we observe from the vibrational analysis, the test probes would move on the order of several μm . This resulted in some images showing extremely blurred lines or even double lines instead of one distinct line where the model moved several pixels over the camera sensor at the set acquisition time.

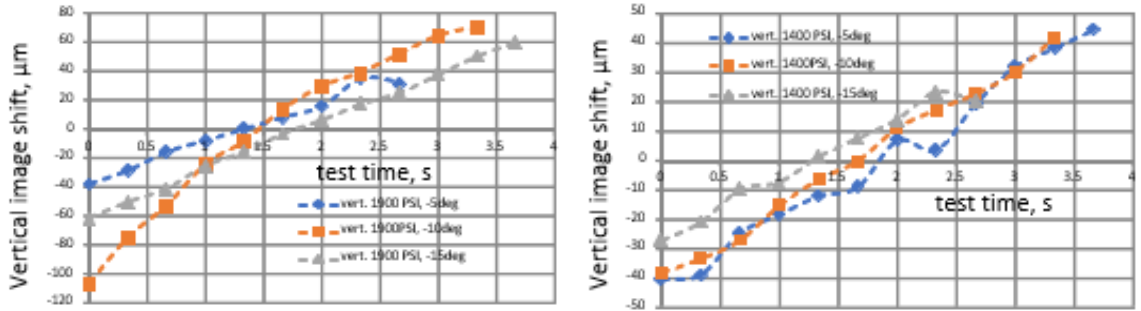


Figure 3.13 Measured vertical displacement of horizontal lines in subsequent images using Nikon camera with constant illumination for 1400 and 1900PSI [3]

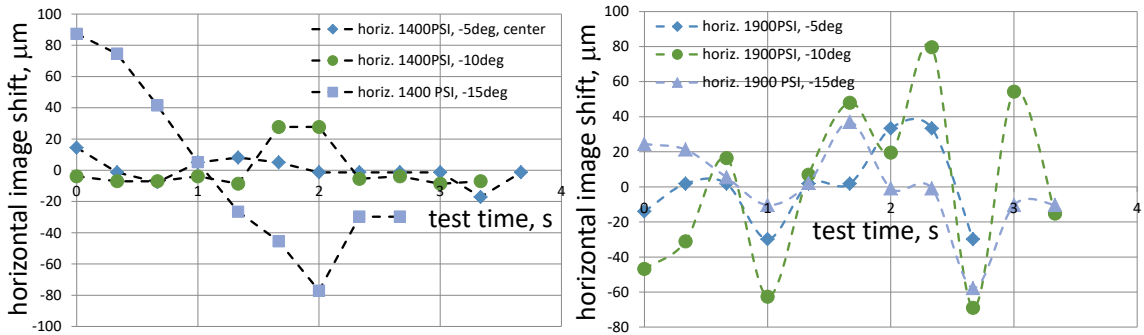


Figure 3.14 Measured horizontal displacement of vertical lines in subsequent images using Nikon camera with constant illumination for 1400 and 1900 PSI [3]

The main goal of the vibrational analysis was done post first test campaign to determine an adequate acquisition time to prevent or at least minimize vibrational influences during future test campaigns. As mentioned above, it was observed in consecutive test images over the tunnel test that horizontal and vertical lines physically shift along the camera CCD. This is due to either a movement of the test probe from flow or the camera oscillating along the direction of flow. Although, cannot be determined directly, it is possible to trace the low frequency oscillation of the lines on the camera CCD and is this is shown in Fig. 3.13 and 3.14 for the vertical and horizontal directions respectively. In the vertical a continuously increasing shift is observed over the 3.5 second test duration indicating an oscillation frequency less than 1/3 Hz. However, this is much lower than those amplitudes derived from the accelerometer data. In the horizontal direction oscillations on order of 1 Hz are observed, again though, with lower amplitudes than those derived from the accelerometer data. From the accelerometer data analysis, acquisition times not influenced by oscillations with frequencies greater than 10 Hz are needed to prevent vibrational influences. This was realized by minimizing the illumination

time of the test models through two pulsed flash systems. Due to geometry difficulties illuminating the wedge model from outside through the test window which is also used for imaging with the Nikon camera, a Xenon flash lamp (Balcar 6400 Source ASYM) with a pulse width on order of 2-6 ms was positioned at the top window flashing down into the chamber. For the cone model, Xenon flash illumination through the top window as well as illuminating the model by a commercial camera flash with pulse width of 400 μ s through the side window were both possible without significantly increasing the noise level. In addition, constant illumination through the facility LEDs at reduced acquisition times of 1/6 s, as the camera allowed for proper illumination, was applied for tests with the cone model. These results are discussed later in Chapter 4.4.2 and displayed in Fig 4.17.

3.5 Distortion Analysis Methods

To determine distortion as a measurable quantity a definition needed to be established. This was the Strehl Ratio that was previously discussed briefly in section 1.1.2. The Strehl Ratio is defined as the ratio of the peak intensity of a point source from an aberrated image to that which is diffraction limited. The primary idea is that a point source illumination from a diffraction limited system would provide a defined point spread function (PSF) illumination pattern that has a maximum intensity and the aberrated pattern would be less where the illumination has been scattered outwards.

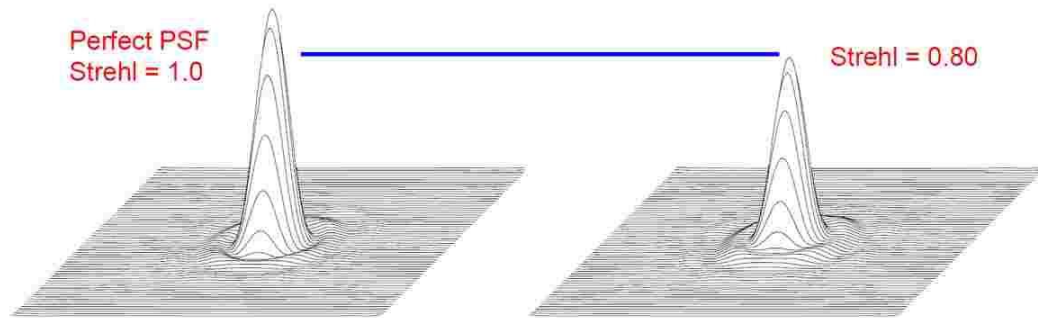


Figure 3.15 Illumination pattern of a point spread function for a diffraction limited and aberrated case [1]

Fig. 3.15 gives an example of a theoretical point spread function that may be obtained from a diffraction limited case and compares it to one that is distorted. It is assumed that the amount of light input into both scenarios is equal and the decline in peak intensity in the distorted profile is a spreading of the light outwards from the central point. The PSF to the right with a theoretical Strehl of 0.8 shows this, where there is an increase in the light exposed to the first-degree bright fringe. A result of light spreading from the PSF also is that the width of these central profiles changes as well. Though, from experience PDFs proved difficult to align accurately and consistently to the camera array. Another way to look at this problem was investigated.

If we consider a line of infinitesimal width, we can interpret this line as a combination of an infinite number of points. The resulting profile across that line is the line spread function (LSF). The line spread function can be obtained either directly by imaging an ideal slit using a test target or numerically as the spatial derivative of the Edge Spread Function (ESF). For our test case we use our gridded pattern with precise etchings to provide a simulated slit for measuring LSFs. The final profile is what is shown below in Fig. 3.16 and would be obtained. This profile then could be achieved not by summing the point spread function cross section, but also by imaging an illuminated line. The corresponding

line spread functions would provide the same results for distortion analysis as the Strehl Ratio is only dependent on the ratios of the maxima. The observed distortion would still be observable as a broadening of the line spread functions to the outer wings.

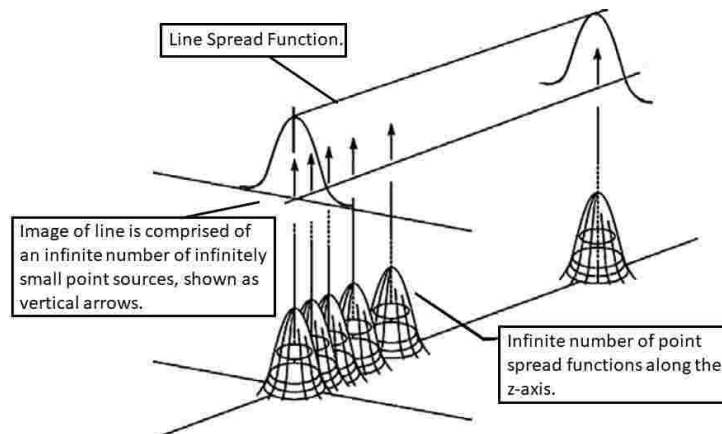


Figure 3.16 Illustration of how the LSF is derived from the PSF [1]

In the first test campaign the use of line spread functions was ultimately identified as the method of which distortion would be analyzed. A broadening of the corresponding line profiles that were laser etched to the wedge plate inserts and the cone model would be the distortion that we observe. A critical component to this technique would require that the amount of light observed during the diffraction limited and aberrated profiles were equal. That is because if the distortion measured is described by only the maxima, a decrease in light would falsely appear as an increase in distortion. This effect was indeed observed during testing and during tunnel operation over both test campaign for unknown reasons. It seems that during tunnel operation there is a scattering of light which is eventually lost from the observed profiles. This phenomenon persisted with all illumination methods used. This unfortunately complicated the analysis procedure that would be applied since describing distortion as a ratio of the peak intensities of the profiles provided inaccurate results. Two different solution approaches to this problem were developed from the first test campaign to the second. In the following, the exact methods used for extracting a Strehl

Ratio from the data collected will be discussed in detail in Chapter 4. The procedures were all done using MATLAB R2017 –R2020b.

CHAPTER 4. ANALYSIS METHODS ON OPTICAL DISTORTION

The measurement strategy was to record images without flow field interactions simulating a distortion free reference to compare to images that would be taken during tunnel on conditions. Recorded differences in the pre-test and during-test images are used to determine parameters that characterize a quantitative amount of observed distortion. Specifically, the differences in the defined LDFs are investigated for observable distortion through the flow field which would result in a broadened signal distribution. For each of the horizontal and vertical section extracted from the models as displayed in Fig. 4.1, 51 individual LDFs were analyzed over the RGB colorspace. These profiles would be extracted as an observed intensity on the camera CCD to a spatial coordinate defined by the pixel.

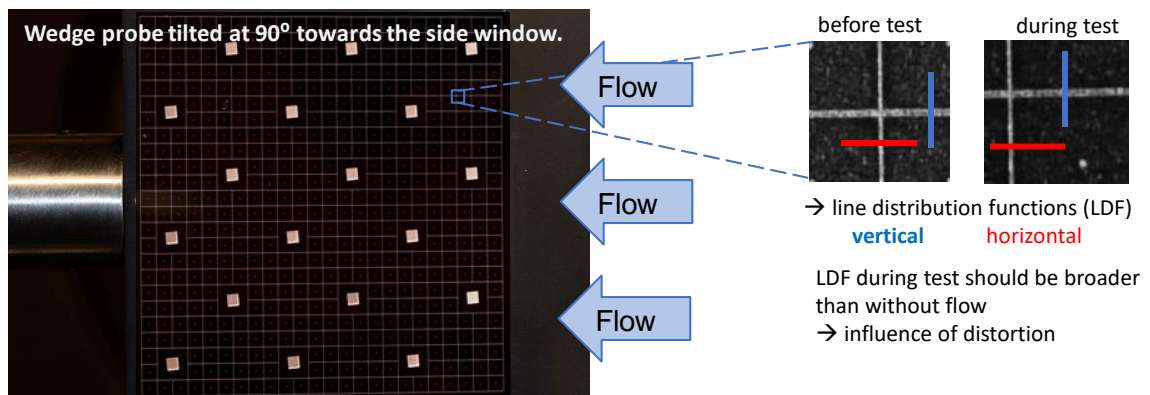


Figure 4.1 General principles of how LDFs were extracted during tunnel operation [3]

4.1 Strehl Ratios and Line Distribution Functions

Using the extracted LDFs, Strehl Ratios can be determined. Strehl Ratios can be derived from the ratio of the peak intensity observed from the LDF of the profile influenced by distortion (during tunnel on images) to a diffraction limited system peak intensity, which here is defined as LDFs captured right before and after tunnel operation, but otherwise would be similar conditions. The Strehl Ratio is commonly used for optical quality measurements where the quality is often compromised due to turbulent flow. For the case

that a Strehl Ratio of 1 would be observed, this would mean that there is no effect on optical distortion and that the before and during test images are identical.

It was observed that during tunnel operation that there was an overall loss of light which contributes negatively to the Strehl Ratio where we are interested in the peak intensity values, as these would also be falsely lower in the during test images. There is no exact reasoning as to why this occurs, but one explanation would be a scattering of light from the illumination method from particles in the tunnel flow. Although this light loss cannot be perfectly identified, it does however directly influence the results that are calculated when interpreting Strehl Ratios from the peak intensities. A new formulation of Strehl Ratio was to be identified as a ratio of the widths was investigated as the overall shape of the profiles was not as easily disturbed.

Theoretical LDFs were generated through the shapes of Gaussian, Lorentz, and Voigt profiles. From these generated profiles ratios of their peak intensities were compared to the ratio of their full widths at half maximum (FWHM). A final constraint was held that when generating the profiles, the area under each curve was identical, therefore simulating that there was no loss of signal before a theoretical before and during LDF. From all profiles investigated it was seen that the ratio of their peak intensities was identical to the inverse ratio of their FWHM. Therefore, it is determined that the Strehl Ratio could also be defined using the shape of the profiles. This would allow for a better interpretation of the actual data.

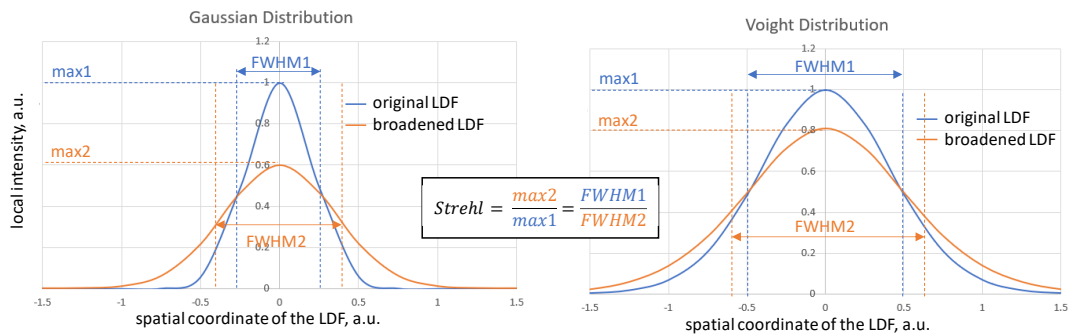


Figure 4.2 Theoretical Gauss and Voigt distributions are investigated for reformulation of Strehl Ratio.

By definition the Strehl Ratio is determined by comparing an image influenced on distortion to that of a diffraction limited one. The best possible resolution achievable is

defined by an Airy disk which is the diffraction limited of a point source for a best focused lens. This profile has an intensity profile which is defined as

$$I(\theta) = I_o \left(\frac{2J_1(ka \sin \theta)}{ka \sin \theta} \right)^2 = I_o \left(\frac{2J_1(x)}{x} \right)^2 \quad \text{Eq. 5}$$

where I_o is the maximum intensity of the profile at center, J_1 is the Bessel function of the first kind of order one, k is the wavenumber defined by $2\pi/\lambda$ where λ is the wavelength of light, a is the radius of the aperture, and θ is the angle between the center of the generating aperture to the radial position away from center. A Gaussian profile can very closely resemble that of the first order Airy disk profile where the two have similar FWHM. Theoretical Airy disk and Gaussian profiles were generated to confirm recreation of this and shown in Fig. 4.3. Therefore, for analysis of the profiles using the overall shapes of the curves a Gaussian profile is selected since its mathematical formulation is much easier characterized by a single parameter given by its FWHM.

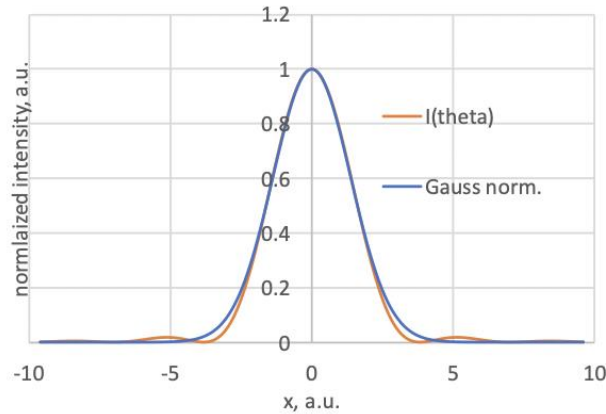


Figure 4.3 Comparison of theoretical Airy disk and Gaussian profiles with similar FWHM

4.2 Methods of Extracting LDFs from the Measured Profiles

Laser etched patterns in the form of narrow lines were captured on the camera CCD and is resolved only on a few pixels. In an ideal world, while analyzing these LDFs one would expect to observe that of a step function where all the intensity from the illuminated line profile would be focused on a single pixel or group of pixels. Unfortunately, this is not a perfect system and there are intensities found across several pixels which extend past that

of a step function and there is intensity found far from center. Typically, the half widths that were observed were on the order of $\sim 1-3$ pixels. Because of this, the underlying Airy disk or best estimated Gaussian profiles are on a sub pixel scale and are integrated over the individual pixels. Fig. 4.4 illustrates the integration of what the camera observes on the CCD. Since most of the profiles are only on order of a few pixels it should be noted that they are not symmetric often. From this, a key factor to consider is that the center of the LDF does not align perfectly to the center of a pixel on the camera CCD.

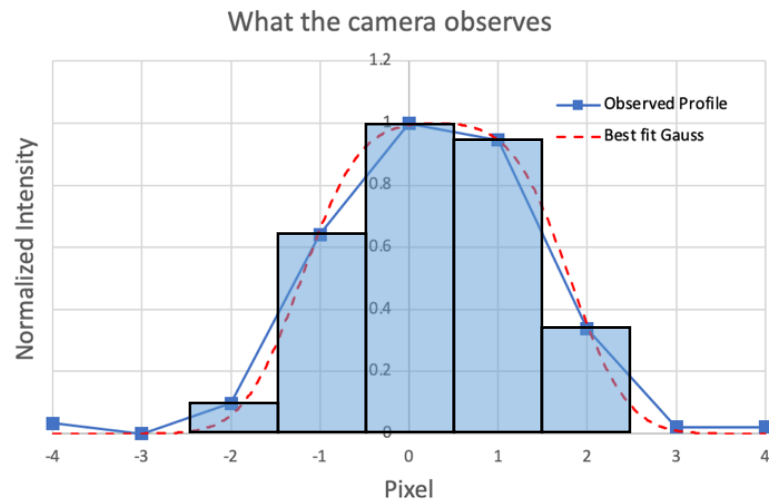


Figure 4.4 Illustration of the high-resolution profiles on the CCD

One major problem in this work was to extract features of the underlying high-resolution profiles from the measured profiles in what is observed from the camera. In general, two approaches were investigated:

1. Interpolation of measured profiles and potential increase of the resolution beyond the pixel resolution through averaging of multiple adjacent measured line profiles.
2. Theoretical formulation of high-resolution profiles with subsequent fitting of measured profiles by integration to the CCD pixel resolution.

In the following, both approaches are discussed in more detail.

4.2.1 Fitting Measured data through an integration of a single High Resolution Gauss profile

This method was already briefly stated before in this chapter, where physically there should be a continuous light distribution that exposed the camera sensor to give the measurements seen. We start with a continuous profile and integrate over the pixels to recreate what would be observed by the camera. The agreement between the measured profiles and the simulated high resolution Gauss profiles depends on the generating distribution type and the integration method. The integration method mainly is influenced by the originating Gauss width and the shift of the distribution maximum to the pixel center. Fig. 4.5 illustrates a fast approximation of fitting a measured profile with a single generating Gaussian profile. The solid red curve is the best simulated profile using the dashed red generating Gauss when integrated to the pixel resolution and matching the 3 central maximum intensities.

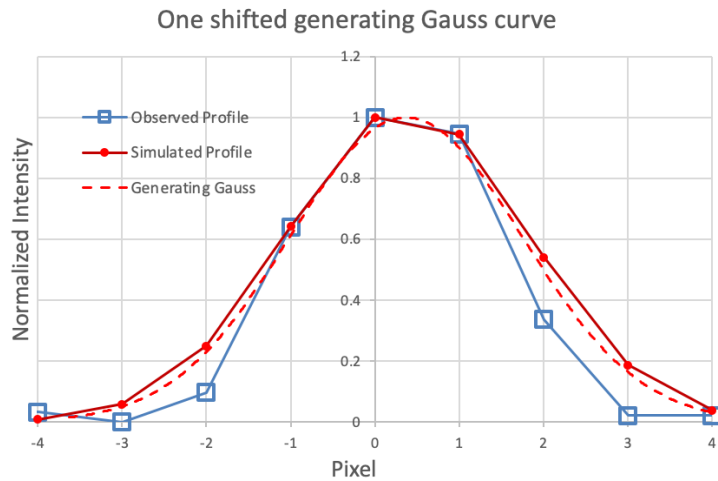


Figure 4.5 Best fitting of a measured profile using a single Gauss distribution

In the example provided, this generating Gauss needed to be shifted by approximated one-third of a pixel to the right to match the central 3 maximum values, and in fact that match and agree very well. The wings of the profile however do not agree sufficiently and therefore this generating Gauss is not what the camera physically observed. Despite that, this method is very intriguing where the generating Gauss that is generated can be very easily automated by investigating a ratio of the 3 central maximum values.

Creating a ratio of the central maxima as the central maximum squared over the product of the second and third provides a quick and easy to generate metric for the best fitting Gauss profile.

$$r_{3max} = \frac{I_{max}^2}{I_{max2}I_{max3}} \quad \text{Eq. 6}$$

For different shifts of the high-resolution Gauss distribution to the center of the CCD pixel, this ratio will slightly change for one given half width at half maximum (HWHM). When plotting this ratio over a range of half width steps on order of 0.01 pixels a unique relation can be obtained. The relation obtained between HWHM and r_{3max} is shown in Fig. 4.6 for values between 0.6 and 3, which should fully encompass the widths that we have for the measured wind tunnel data. The resulting curve is split into 2 different polynomial fits to give sufficient agreement to the original data. For this relation when splitting into two 6th order best fit polynomials where r_{3max} is greater or lesser than 2.5 R^2 values of 0.9999 are observed on either side of the curve.

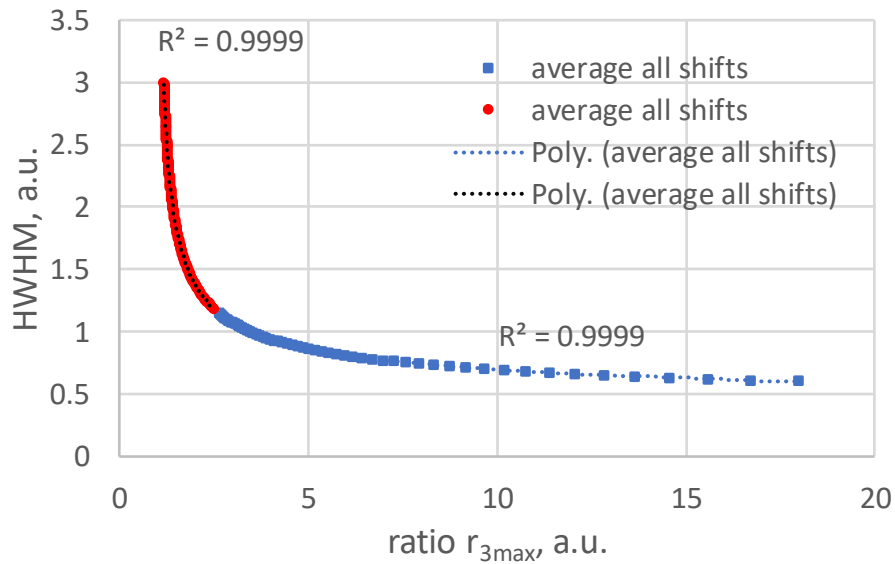


Figure 4.6 Observed relationship between the profile HWHM and r_{3max}

However, for broader profiles the 3 maximum intensities might not be sufficient to characterize the underlying Gauss profile. Therefore, it was investigated to use more maximum values of the measured data for finding the best Gauss profile. For this, the 4th maximum was included, and a new ratio was investigated, that was

$$r_{4max} = \frac{I_{max}I_{max2}}{I_{max3}I_{max4}} \quad \text{Eq. 7}$$

This new ratio shows similar properties as the one that was characterized using the three maximum values, but the effect on the shift of the pixel is lower for the ratio when using 4 maximum values. Fig. 4.7 shows the new relation between HWHM of the originating profile width and r_{4max} . If you consider a narrow profile though, such as the example above in Fig. 4.5, the 4th maximum could be lost in the background noise. Therefore, it was chosen to use r_{3max} relation for HWHM values up to 1.5. When the HWHM exceeded this, the analysis was switched to use r_{4max} .

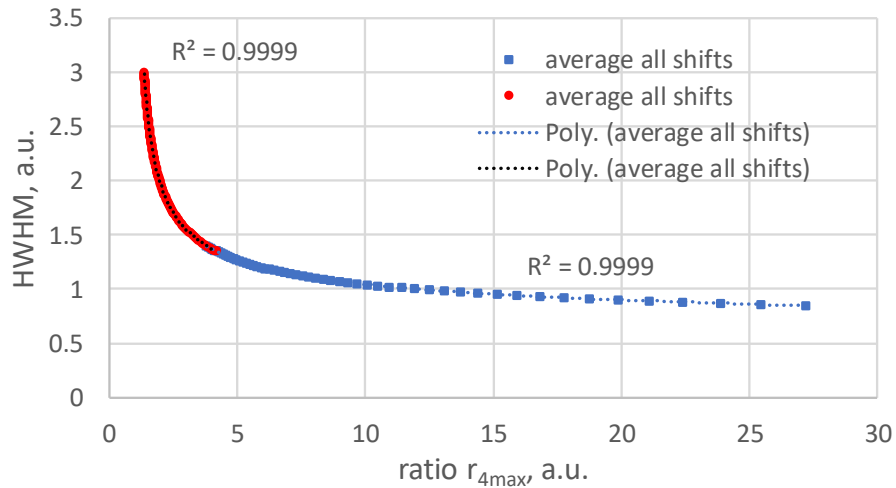


Figure 4.7 Observed relationship between the profile HWHM and r_{4max}

4.2.2 Superposition of multiple narrow Gauss profiles

Using a single high-resolution Gauss proves to work well when fitting the measured data to the center values. However, we are not able to fit this well far from center using this method and the measured data in the wings is not sufficiently reproduced. Therefore, a generating profile was created through a superposition method using multiple narrow Gauss distributions. This idea was brought up similar to how a LDF could be generated as a superposition of many PDF as discussed in Chapter 3.5. This method involves 2 fitting parameters that were the width of the originating Gauss and the superposition length over the sub pixels. Fig. 4.8 illustrates the method of creating a new generating LDF using a

single black narrow Gauss that has been shifted by the superposition length and then integrated over. Using this method, by finding the appropriate length and originating width it was possible to create a generating LDF that more accurately represented the measured data as a whole, even far from center at the wings. In Fig. 4.9 the same measured data as before is attempted to be simulated with much better results at the wings, where the simulated profile begins to collapse onto those that were measured.

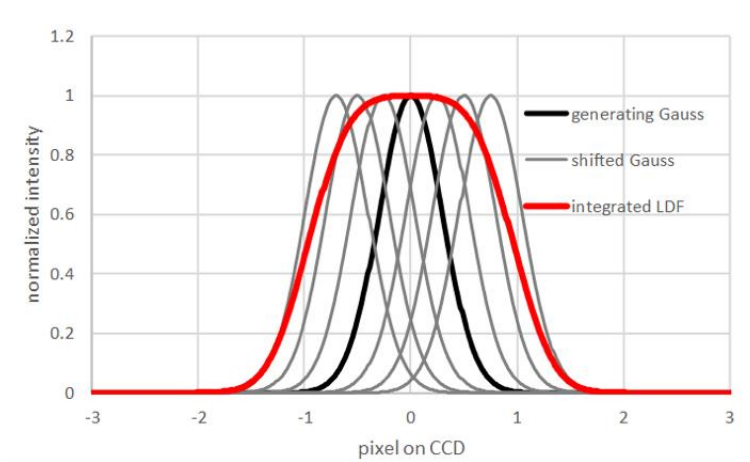


Figure 4.8 Using a superposition of many narrow Gauss profiles to create a non-Gauss generating LDF

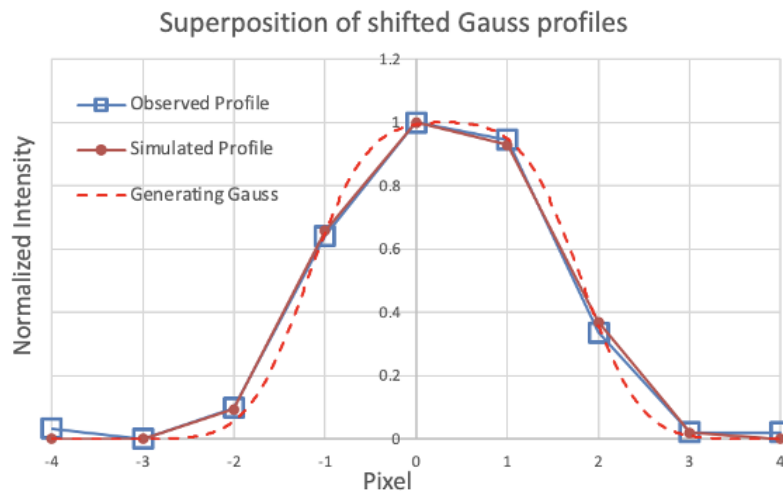


Figure 4.9 Best fitting of a measured profile using a non-Gauss distribution created from a superposition of many narrow Gauss profiles

To apply this method to experimental data from the tunnel experiments, a database of new modified Gauss profiles needed to be created which included the new parameters. The current database includes modified Gauss profiles with parameters of:

1. 0.35 to 0.55 pixels originating Gauss half width in increments of 0.005

2. 75 to 230 integrations of the similar Gauss profiles to create the modified Gauss, with step increments of 1/100 of a CCD pixel.
3. -0.35 to 0.35 pixels shift across a CCD pixel in increments of 0.01 pixels.

This database creates profiles that simulate Gauss profiles in a range from 1.52 to 4.62 pixels in FWHM which covers well the tunnel data where the FWHM of the measured profiles is generally on order of 3 pixels.

The automated fitting procedure uses a correlation algorithm which sums up the differences of the highest 5 profile values of the normalized measured profile to the simulated one. The algorithm has been tested against simulated profiles and showed accuracies better than 5% in profile width. One advantage of this fitting method over the interpolation method described in the previous sub-chapter is that the results are not averaged over an entire spatial region so spatial variations of the line width are included when the different images are aligned to each other. Therefore, statistical analysis of the obtained results can be conducted to provide uncertainty estimates.

To reduce scatter in the analysis of the measured data, it was chosen to eliminate outliers in Strehl number by using only 2/3 of the available data along the laser-edged line and neglecting profiles which yielded the highest and lowest Strehl numbers. This means that we used only the data within one standard deviation in terms of Strehl number.

The procedure to automatically generate the best fit with database LDFs in MATLAB is:

1. Call most current high-resolution database with 1.52-to-4.62-pixel FWHM to memory.
2. Provide input location for analysis which finds the 5 maximum values for each LDF along each experimental dataset.
3. For each measured line profile, a correlation factor is calculated against all modified Gauss LDFs in the database, and the best fit profile is selected.
 - a. This best fit curve has all information on the originating Gauss width, number of integrations, pixel shift, and the FWHM of the modified Gauss.

4. Step 3 is repeated for all images and the resulting FWHM of the nominal images is compared to that of the distorted images.
5. Distorted images do not always have the same spatial scale as the nominal images. A linear interpolation is used to align the datasets to one another.
6. Once the datasets are aligned, Strehl ratios are calculated for every LDF.
7. An average best of 2/3 of the data corresponding to the data within one standard deviation is selected from the Strehl results and the corresponding FWHM data are used to determine the final Strehl numbers.

4.2.3 Direct Interpolation of measured Line Profiles using an Averaging over Shifted Profiles

As already discussed, most of the profiles measured are non-symmetric to the maximum since the underlying high-resolution profile that caused the camera to observe the measured profile is shifted off from the pixel center. Linearly interpolating artificial data points between the measured profiles data points does not yield any additional information about the underlying profile shape. Therefore, additional information is gathered by means of averaging over several adjacent profiles. The following methods of doing so was developed to analyze a measured profile:

1. Linearly interpolate a measured profile on a resolution of 100 points per pixel.
2. Determine the half maximum points of this profile to get a first estimate of its half width.
3. Shift the whole profile so that the two half width points are symmetrical to the new line center (which now does not necessarily show the maximum intensity).
4. Add up multiple (up to 50) adjacent lines all centered to their individual half widths. This new profile now shows a non-linear shape in between the original pixels and does carry additional information about the line shape compared to individual interpolated profiles.
5. Measure half widths directly from this new profile or fit it with an appropriate theoretical line shape (as discussed before, a Gauss profile offers itself).

This principle was used in analyzing the wind tunnel data which will be presented in a following section. An advantage of this is that line shape information can be determined that is below the resolution of the pixels. A disadvantage though, would be that the physical laser etched patterns that we are analyzing show variations in the line width over the imaged 50 adjacent lines. Theoretically, these variations in line width are present in both the before and during test images though and would therefore cancel each other out in the final results.

4.3 Lab Experiment using a back Illuminated Slit with Artificial Distortion

A lab setup was created to investigate the sensitivities of the optical setup used during the Mach 6 wind tunnel experiments to Strehl Ratio. To recreate a line profile to measure, a back illuminated slit was calibrated under microscope to $\sim 30\mu\text{m}$ width which corresponds to roughly the average width of the laser etched patterns that were imaged. Also, a similar viewing distance to the object of about 48 inches was used to recreate LDFs with FWHMs on the camera CCD that would closely replicate those during the wind tunnel experiments. To investigate the effect of diffraction broadening, several aperture stops were used to capture the images. The baseline configuration was what was used during the tunnel tests of f/16 and two other aperture settings were used at f/22 and f/32 to provide images with higher diffraction limits.

To recreate a during-test image, some sort of distortion needed to be applied to the images. For this, an artificial distortion mechanism was applied along the optical axis and would be compared to a best diffraction limited system which did not have this along the axis. To provide artificial distortion different plano-convex lenses with focal lengths of 75.6mm (Newport KPX088) and 200mm (Newport KPX106) were placed in front of the slit between images. There were two orientations of the setup that were imaged to provide extra data when analyzing the LDFs which involved flipping the lens so that the flat side was either towards the slit or towards the camera. The measured results in the lab experiment were compared to a numerical simulation in Zemax. Lastly, two slit orientations (0° and 5° tilt to the vertical) to investigate if a controlled positioning of the

LDF on the CCD can yield additional information. A sketch of the setup used is presented in Fig. 4.10 showing the two different orientations of the plano-convex lens.

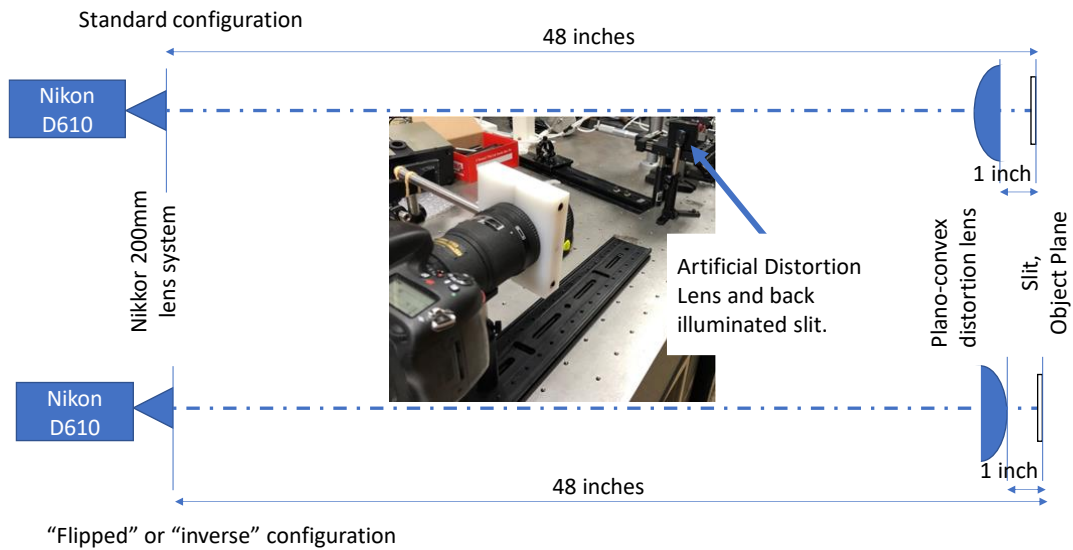


Figure 4.10 Sketch of the Optical Setup used for investigating the setup sensitivity using a back illuminated slit with artificial diction mechanisms

4.4 Results from Mach 6 Wind Tunnel Experiment

There were two measurement campaigns, the first was a 2-week testing period in October 2017 and the second was a 3-week testing period during February-March 2019. The 2017 test campaign focused on the 15° wedge probe insert with interchangeable plates, while the second included additional measurements using the 7° half angle cone model with 10% and 20% blunt tips. A lesson learned from the first test campaign was that the illumination method using continuous light did not provide sufficient lighting to apply short acquisition times. This in turn caused quantitatively unknown influences of vibrations on the model which artificially caused broadening (smearing) over the camera CCD which would be misinterpreted as optical distortion. Therefore, different flash illumination methods or short acquisition times below the measured critical vibrational frequencies were used when gathering data during the second campaign. In addition, tests were conducted to investigate the influence of tunnel vibrations by using a constant illumination at various camera acquisition times and comparing these results.

4.4.1 Selection of Analysis Locations for the models

The analysis locations in the 2017 test campaign were chosen from the vertical lines of all gridded patterns from the initial test plate. The initial test plate and the extracted locations for measurements are displayed in Fig. 4.11. The LDFs were built as an average over all adjacent profiles over 25-pixel rows. Because of the influence on vibrational effects, the three images that yielded the least influence of distortion were then averaged to gather 1 Strehl Ratio at every location on the plate [3]. Later in the next testing campaign the analysis method was refined to include the interpolation method described earlier.

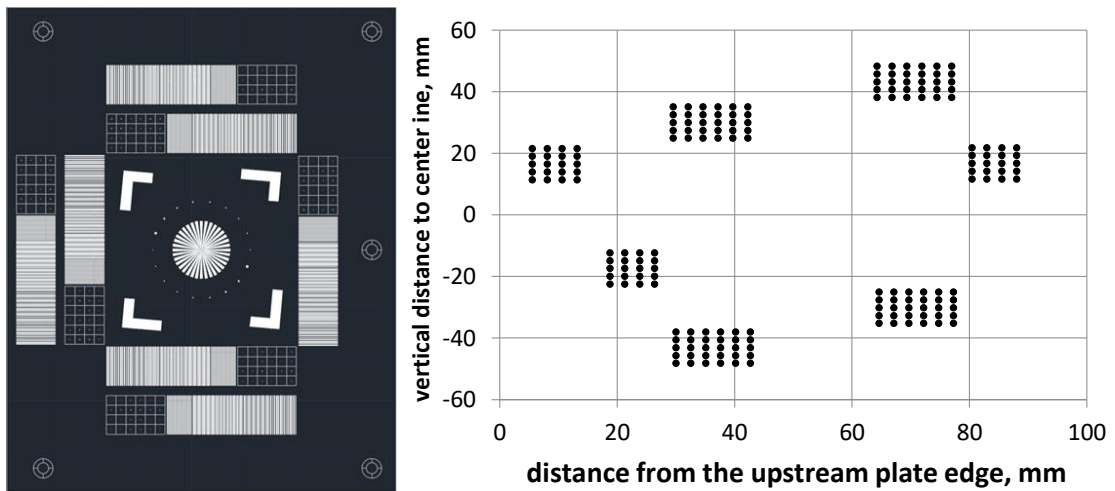


Figure 4.11 Selected locations for analysis on the wedge plate from the October 2017 test campaign

The analysis locations in the 2019 test campaign were highly influenced by the damage that was occurring to the plate from particles in flow (not present in previous testing). After just one test of the wedge probe at 1900 PSI and an angle of attack of 15° , the optical patterns on the plate insert were severely damaged and would cause false signals during analysis procedures. From the particles impacting the plate over the course of one test the LDFs were becoming disfigured in many locations on the plate. Fig. 4.12 illustrates an evolution of the plate quality during that first test.

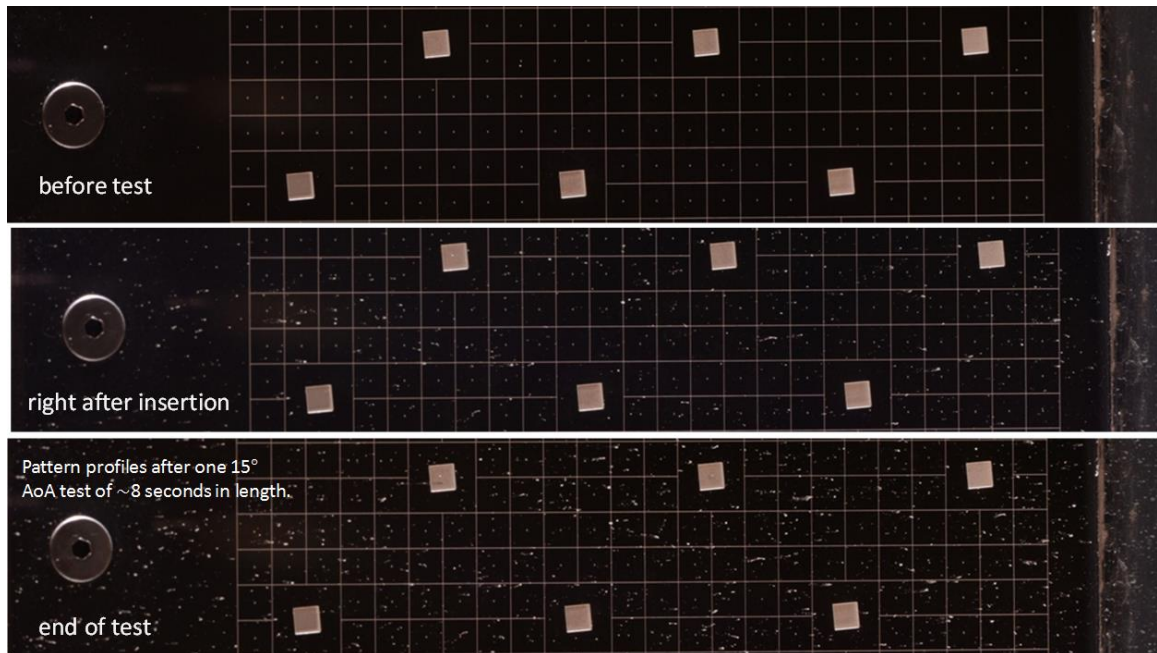


Figure 4.12 Surface evolution of the LDFs on plate insert during the first test

From earlier measurements it was observed that surface damage was greatly dependent on reservoir pressure and angles of attack. However, surface damage also significantly increased with both increasing pressure and angles of attack. The test matrix was changed to include the test conditions that did not damage the plate as quickly so that more of the measured data would be usable. These locations were identified from the final test that was performed using that plate. If there was no observable damaging at the selected locations after the final test, there would be no damage at those locations during prior tests. In the following analysis, the locations are addressed by their distance to the upstream leading edge of the plate insert regardless of their vertical location.

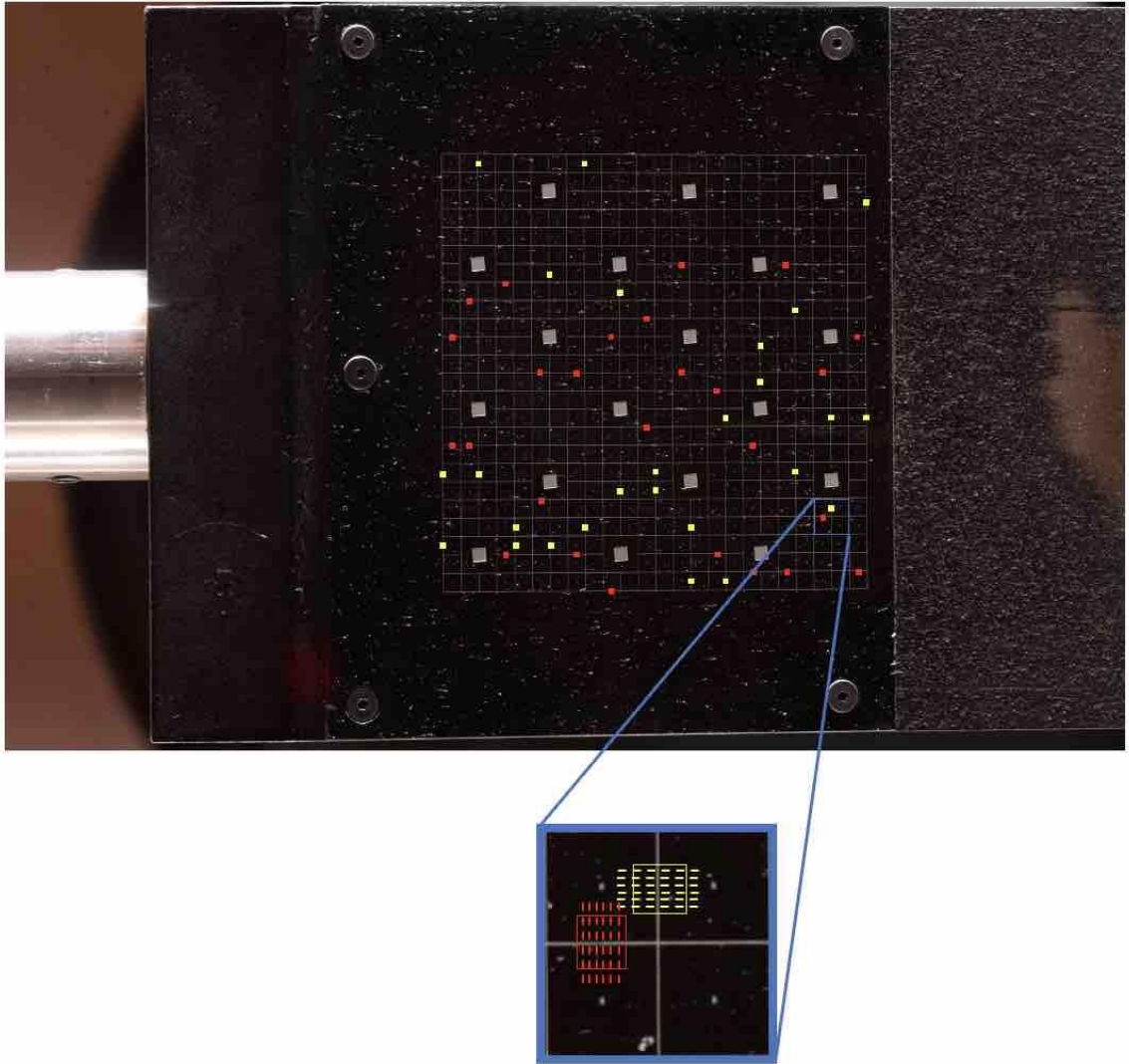


Figure 4.13 Selected locations for analysis on the wedge plate from the February-March 2019 test campaign

The cone probe was manufactured of carbon steel and was subject to a Zinc coating that blacked the surface. The surface was then laser etched with axial and radial lines, $\frac{1}{4}$ inch and 10° respectively, that would give the surface a grid like pattern for similar analysis to the wedge model. The field of view of the camera was ~ 7.5 inches (190mm) and was aligned so that the upstream side of the field of view aligned to the location where the cone tips attached. This was to include what was expected to show regions of both laminar and turbulent boundary layers as discussed previously in Chapter 3.3. This region should include a section of the cone body where a laminar boundary layer is present, but transitions to turbulent downstream for the 10% tip (see Fig. 3.7).

Just as was observed for the wedge model, the cone was also subject to particle damage with increasing reservoir pressure and higher incident angles of attack. Again, analysis locations for the cone model were selected after the final test was conducted so that there is no significant particle damage along the LDF. These locations are illustrated in Fig. 4.14.

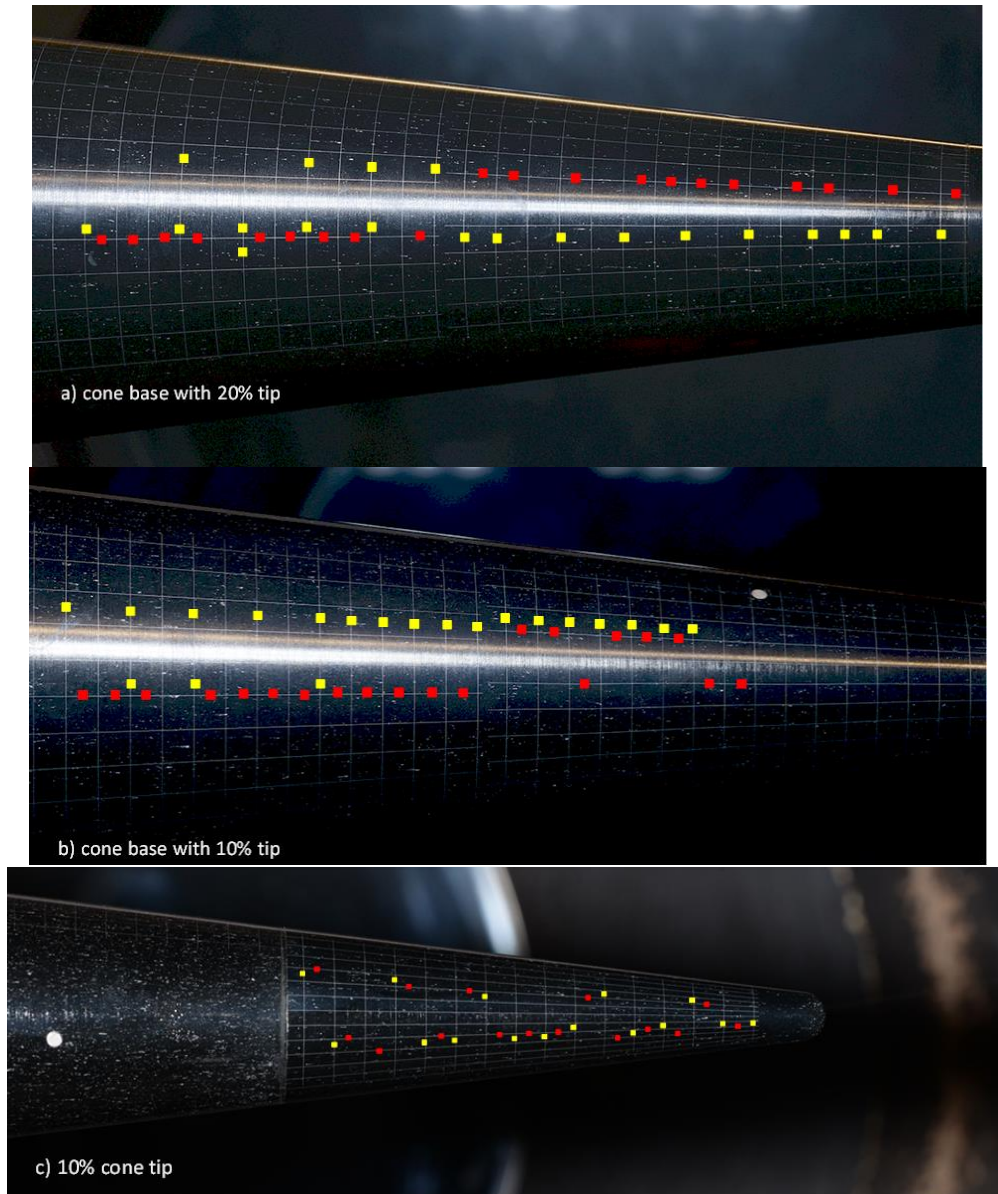


Figure 4.14 Selected locations for analysis on the cone base of 20% and 10% blunt tips and on the 10% tip with the least influence of particle damage

4.4.2 *Strehl Ratio Results with the Wedge Probe*

A goal of repeating wedge tests in the 2019 test campaign was to verify results that were seen from 2017 which indicated aero-optical distortion for conditions of high pressure

and high angles of attack [3]. The current analysis methods do not confirm what was previously measured for the wedge model where Strehl Ratios around 0.8 were measured for 1900PSI and 15° angle of attack. This indicates that there is no aero-optic distortion present in the visible data from the flow field around the wedge. An additional analysis of the previous raw data was repeated using the FWHM of the extracted LDFs to eliminate uncertainties that were present about the loss of intensities from the visible images during the tunnel test. The Strehl Ratios that are extracted from the old data agree well with those that were originally reported and shows an increase of Strehl Ratios downstream of the leading edge ending in unphysical values greater than 1 [3]. The results from the FWHM analysis on the old data is presented in Fig. 4.15.

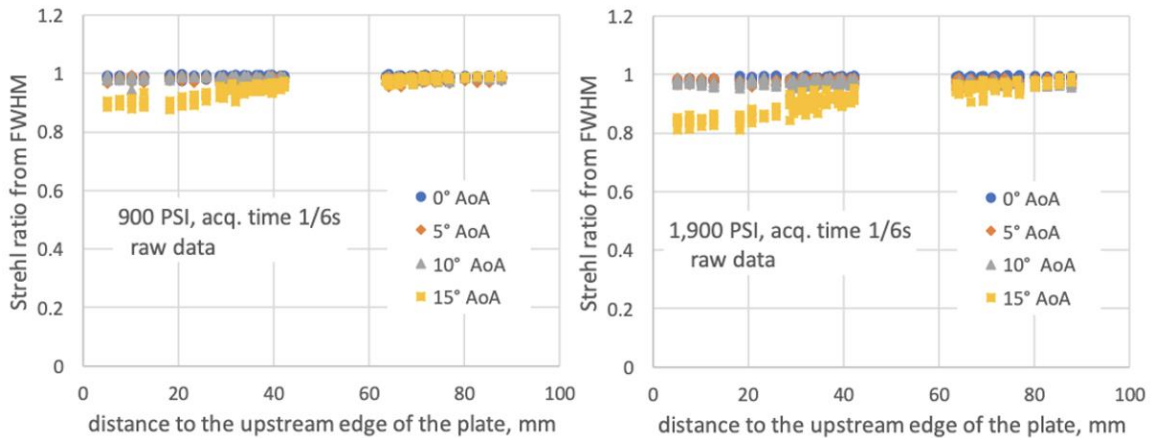


Figure 4.15 Resulting Strehl Ratios from the old test data using the FWHM of the extracted LDFs for 900 and 1900PSI over all angles of attack.

These experiments though were conducted with constant illumination at camera acquisition times of 1/6 seconds. Therefore, these results were subject to potential broadening as identified from the vibration analysis. To illuminate the effects on vibrational broadening, lighting through a Xenon flash lamp placed at the top access window of the tunnel illuminating the wedge indirectly, which eliminated the problem with glare from the side window which mainly motivated the use of constant illumination in the first campaign. As mentioned earlier, analysis of the LDFs was conducted for the 2019 campaign using the ratio of FWHM, ultimately eliminating the any issues of a loss of light that was previously present. Results from the wedge model using flash illumination is shown in Fig 4.16.

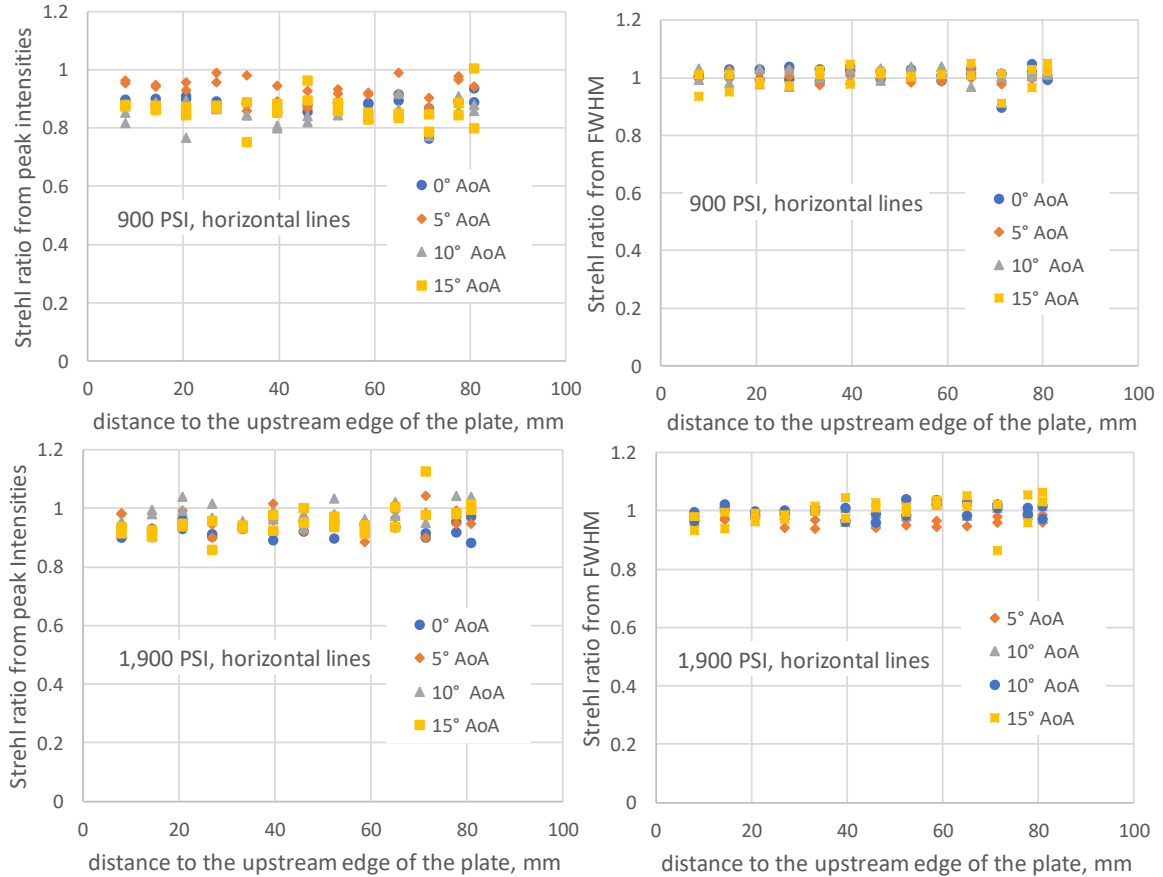


Figure 4.16 Strehl Ratios extracted from the flash illuminated images at 900 and 1900PSI using both intensity and FWHM ratios.

To understand more on the vibrational influences of the tunnel that is present in the old raw data, an additional measurement was conducted using constant illumination, but varying camera acquisition time was set to capture more effects of vibration. The acquisition times of the camera were set to include what was initially present in the results from the old data of 1/6, and additional times of 1/30, 1/60 and 1/100 were added to show a decrease in the vibrational influences.

Results from this analysis for both vertical and horizontal lines at reservoir pressure of 1900 PSI and 15° angle of attack are shown in Fig. 4.17. For the vertical lines (influenced by vibrations in flow direction) there is a clear trend that with decreasing acquisition times there is a lesser influence on the vibration broadening. However, the horizontal lines that are perpendicular to the flow and used for analysis in Fig. 4.16 do not see this effect. There is a small increase in Strehl Ratio with distance from the upstream edge of the plate which qualitatively is in agreement with the earlier data displayed above. The differences between

the two measurements though from Fig. 4.16 and 4.17 are that there could be a slightly larger gap between the plate insert and the leading edge that would cause a larger secondary shock and the plate thickness between the plates varied by 1/1000th of an inch (0.006 inches for the recent steel plates and 0.005 inches for the old aluminum plates). Either of these could have influence on the slightly different results and cause higher apparent Strehl Ratios that are presented between the two test campaigns.

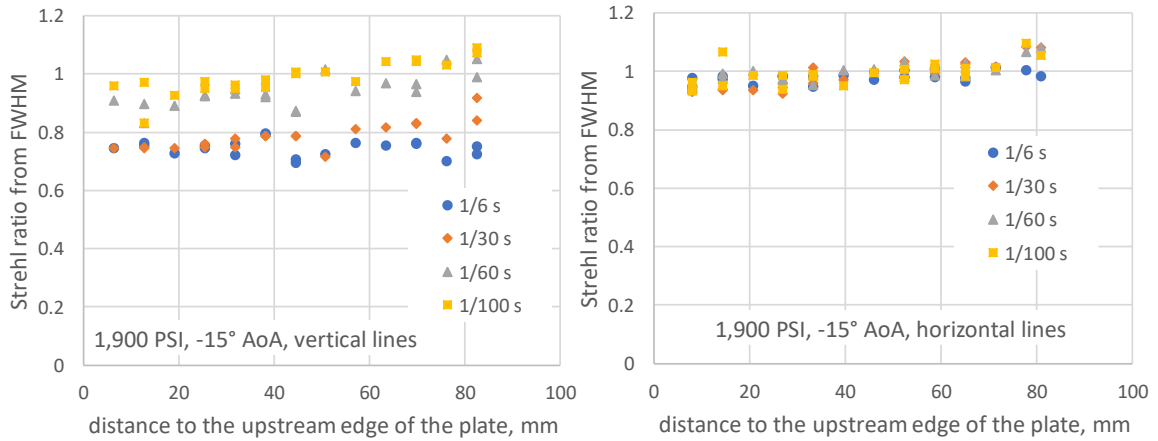


Figure 4.17 Strehl Ratios extracted from LDF FWHM ratios with constant illumination and varying acquisition times at 1900PSI and 15° angle of attack

4.4.3 Strehl Ratio Results of the Cone Model

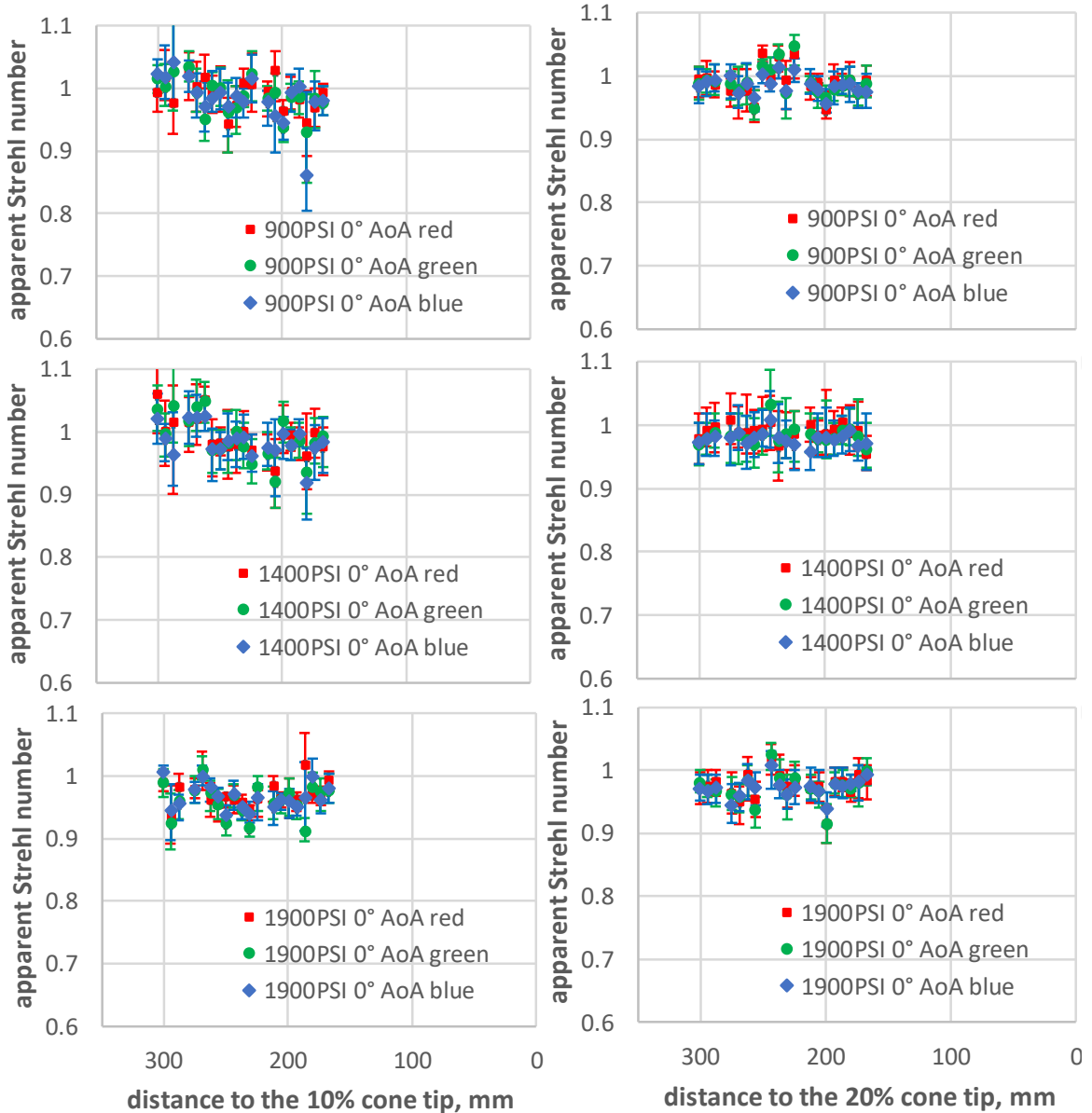


Figure 4.18 Strehl Ratios from LDF FWHM ratios vs distance to the 10% and 20% blunt cone tip on the cone base for all reservoir pressures under a 0° angle of attack for the RGB camera pixels.

The results from the Strehl Ratio analysis on the cone body at the two different tip bluntness, 10% and 20% at 0° angle of attack are presented. These values were derived from the FWHM analysis of the horizontal lines that were at circumferential angles of ~10°. The camera was best focused to the 0° circumferential angle and straying away far from this angle would cause defocusing errors from the change in depth of field. The analysis is

conducted for all RGB pixel values and Strehl Ratios were evaluated from averaging the results from consecutive images taken during a run. Error bars are included to show scatter between results from different images.

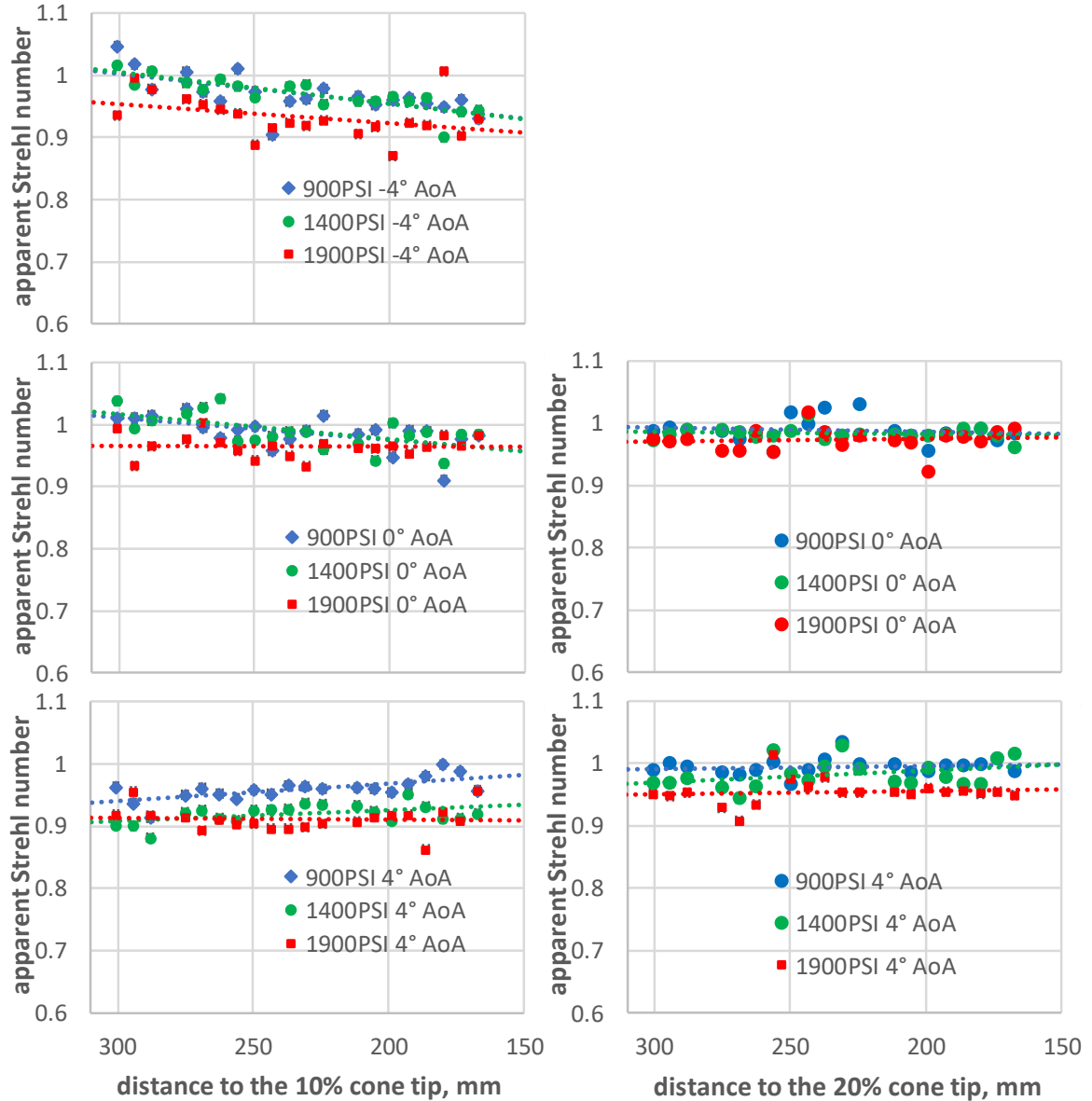


Figure 4.19 Strehl Ratios from LDF FWHM ratios vs distance to the 10% and 20% blunt cone tip on the cone base for all reservoir pressures under all angle of attack averaged over the RGB camera pixels.

Fig. 4.19 show the Strehl Ratios extracted from the RGB averaged LDFs for both cone tips, over all reservoir pressures and angles of attack. The right set of data in Fig. 4.19 shows very little aero-optic distortion with most Strehl Ratios tending to greater than 0.95.

Although, it tends to be the case that the influence on distortion is increasing with increasing reservoir pressures. If effects of distortion are detected it seems that the effect decreases for positive angles of attack relative to cone distance, stays mostly constant for 0° angle of attack, and increases for negative angles of attack relative to cone distance. In general, the effects of optical distortion present are weak with the greatest effect of ~ 0.9 seen for the cone model. There is no clear correlation observed from the onset of the transition of the flow regime determined from the IR imaging as shown in Fig. 3.7.

CHAPTER 5. EXTRAPOLATION OF THE WIND TUNNEL TEST TO REAL WORLD IMAGING

An attempt to relate the tunnel lab experiments to real world applications was performed by analyzing slanted edge patterns on the wedge probe applied during the first test campaign. Image quality measurements were performed using an analytical solution known as the *General Image Quality Equation* (GIQE). This construct was developed as a method for predicting image quality on the *National Imagery Interpretability Rating Scale* (NIIRS) which, by definition, ranges from 0 to 9 for the worst and best image quality measurements, respectively [7]. The basic idea of the resulting NIIRS values is, that they can be closely related to a spatially resolved ground distance which is important for aerial photography. For instance, a NIIRS of 1-2 (low spatial resolution) would describe an image that could detect large hangers, and distinguish between runways in an airfield, whereas a NIIRS of 8-9 (high spatial resolution) would describe an image with the ability to identify weld joints on an object or even identify individual barbs on a line of barbed wire.

5.1 General Image Quality Equation

Initial versions of the General Image Quality Equation, versions 3 and 4, used five image quality factors that would be used as an input for the analytical solution for NIIRS. Those factors were derived from parameters that are seen to affect image quality; ground sampling distance (*GSD*), relative edge response (*RER*), overshoot (*H*), noise gain (*G*), and the signal to noise ratio (*SNR*). Advancements in newer versions of *GIQE* have allowed for quicker assessment of images, and currently the most recent version, 5, calculates *NIIRS* using only the unenhanced image variables [5, 7]. This means that the defined *GIQE 5* is used to approximate *NIIRS* from only the three parameters defined above: *GSD*, *RER*, and *SNR*. The overshoot and noise gain parameters are a product of image enhancement and are no longer needed. The resulting equation of *GIQE 5* is [7]:

$$NIIRS = c_0 + c_1 \log_{10} GSD + c_2 \left[1 - \exp\left(\frac{c_3}{SNR}\right) \right] \log_{10} RER + c_4 (\log_{10} RER)^4 + \frac{c_5}{SNR} \quad \text{Eq. 6}$$

where the c_n values are given in Table 5.1

Table 5.1 Coefficients for current version of *GIQE 5*

c_0	c_1	c_2	c_3	c_4	c_5
9.57	-3.32	3.32	-1.9	-2	-1.8

From *GIQE 5*, values of *NIIRS* were calculated to investigate how image quality was affected from the tunnel flow for the wedge model. For this, effective values for the *GSD*, *RER* and *SNR* with the wedge models test target needed to be determined.

For *GIQE 5*, the *GSD* is calculated in inches and can be found as a function of the distance to the object d , the focal length of the optics f , and the pixel pitch p [10]. For our testing, *GSD* was held constant during the test campaigns and was calculated to be:

$$GSD = \frac{d}{f}p \quad \text{Eq. 7}$$

where the distance to the image plane d was held constant at 48 inches, the focal length, f of the optical system was 200mm, and the pixel pitch p on the CCD array on the camera was 5.984 μ m. Inputting these variables into the equation for *GSD* yields a value of 0.001436 inches. However, when using this for calculation of *NIIRS*, values much greater than 9 were often obtained which exceeds the maximum limit that is defined and did not provide any useful information on the effect of the observed optical distortion to real world imaging. This was most likely a result of the fact that *NIIRS* was created to determine image quality on a much larger scale than that which in our case was almost microscopic when compared to those of aerial photography. Real world effects were therefore hypothetically calculated for distances on 3 typical observation scales: on ground observations (~1km), aerial observations (~10km), and satellite observations (~100km).

The *RER* was determined using an edge response function which measures the ability for an imaging process to produce sharp edges [4, 6]. For our purpose, during the design phase 5° slanted areas were included on the wedge test targets that could be used to measure the camera's ability to produce these sharp edges. This process of extracting an edge response function was done using a commercially available package in *ImageJ* where an area of the slanted edge would be entered into the program, and an average over the slant

would be measured as a function of spatial position. The area used is shown below in Fig. 5.1 and was then averaged across the slant to create the relevant edge response.

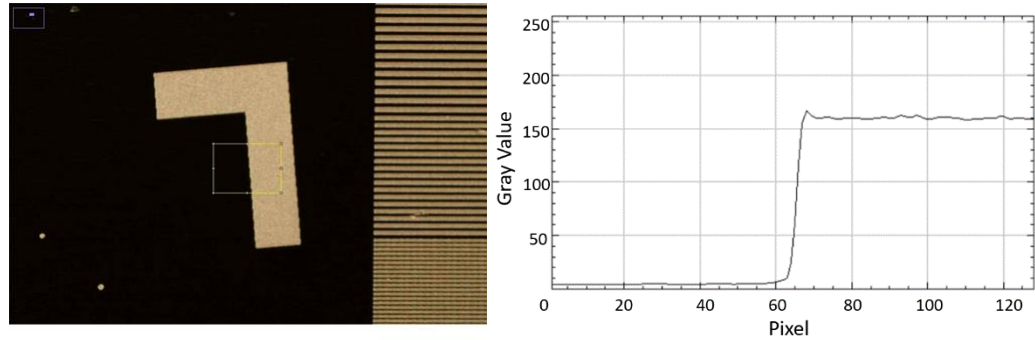


Figure 5.1 The 5° slanted edge area used for characterizing the camera's ability to reproduce sharp edges

The measured edge response function was then normalized. The input for the *GIQE 5* is defined as the difference in the normalized edge response measured at half a pixel on either side of where the edge response measures 0.5. The process is illustrated below in Fig. 5.2.

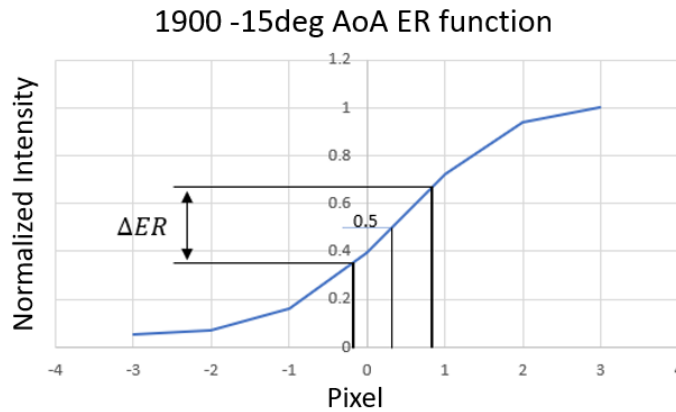


Figure 5.2 The process of measuring RER a half pixel on either side of the 0.5 measured intensity

The final parameter needed for the *GIQE 5* equation is the *SNR*. This ratio is defined as the mean of an area where signal is measured over the standard deviation of a region in which noise is present [10]. Formally, the *SNR* can be written as

$$SNR = \frac{\mu}{\sigma} \quad \text{Eq. 8}$$

For every image investigated the *NER* and *SNR* needed to be calculated where these variables are dependent on the actual imaging through the flow structures. The best two images, similar to as they were defined in the first test campaign, displaying the greatest Strehl ratios from a characteristic location near the leading edge, were chosen for further investigation into real world measurements using the *GIQE 5*. This was done through an analysis of *NIIRS* values over a varying *GSD* as described above to determine the effect of image quality on observation distance.

5.2 Extrapolated Results

The analysis used the nominal pretest image along with the 2 best images as described above in Chapter 5.1. For each of the images selected; best, 1st best and 2nd best (3 best images), *NER* and *SNR* were calculated and held constant over a series of *NIIRS* calculations with varying *GSD*. This was to simulate the effect of imaging at distances much greater than what was done in the wind tunnel, given that we experienced the same image sharpness and signal to noise at the varying distances. With the setup used at the wind tunnel it was observed that for the typical *NER* and *SNR*, and a hypothetical *GSD* of 1 km an *NIIRS* value of 9 was measured. These values would be used as the baseline configuration where a value of 9 is the theoretical best possible imaging giving the *NIIRS* scale. For the further work of extrapolating these calculations to much greater distances, those calculation at 1km were then used to be the baseline measurements. Corresponding *NIIRS* values are shown below in Fig. 5.3 for the experiments at 1900PSI at AoA of -15° and -0°, respectively.

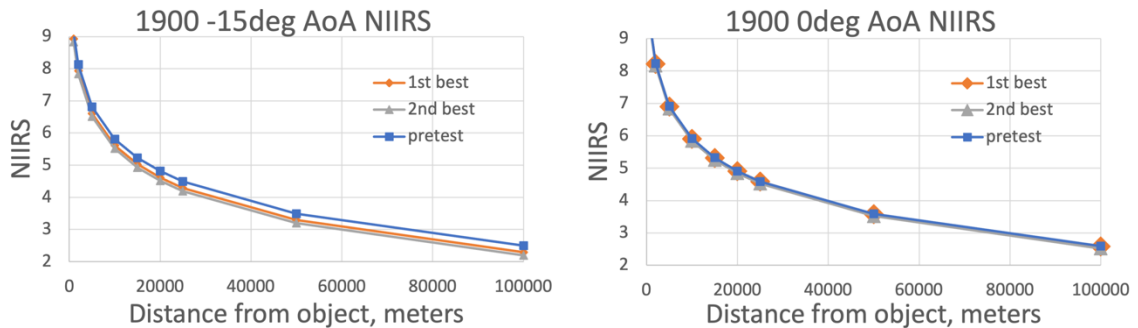


Figure 5.3 Extracted *NIIRS* values for hypothetical distances up the 100km for experiments at 1900PSI and AoA of 0° and -15°

The results agree well with those of what were observed with the Strehl analysis in the first test campaign. There is weak to moderate influence observed for the -15° AoA, but rising with an increase in distance. For the case with 0° AoA, there is no significant reduction in *NIIRS* even if extended to large observation distances. The numerical *NIIRS* values for 1900PSI at an AoA of -15° and 0° is given below in Table 5.2 and Table 5.3, respectively, with a percent change from the pretest images.

A similar analysis was performed for the images at the condition at 900PSI over all angles of attack. As observed from the 1900PSI case, there was little if any influence present at 0° AoA, and only a very weak influence at -15° AoA. This again agrees with the previous Strehl analysis where little effects on optical distortion were observed for those conditions at 900PSI. Numerical *NIIRS* values at the 900PSI condition at -15° and 0° are shown below with the very little influence in Tables 5.4 and 5.5.

Table 5.2 Numerical *NIIRS* values for 1900PSI at -15° AoA

distance, m	<i>NIIRS</i> pretest	<i>NIIRS</i> 1st best	<i>NIIRS</i> 2nd best	1st best/pretest	2nd best/pretest
1000	9.14	8.93	8.83	97.79%	96.71%
2000	8.14	7.93	7.84	97.51%	96.31%
5000	6.81	6.61	6.51	97.03%	95.59%
10000	5.82	5.61	5.51	96.52%	94.83%
15000	5.23	5.03	4.93	96.13%	94.25%
20000	4.82	4.61	4.52	95.80%	93.76%
25000	4.49	4.29	4.19	95.50%	93.31%
50000	3.49	3.29	3.19	94.21%	91.40%
100000	2.50	2.29	2.19	91.89%	87.95%

Table 5.3 Numerical NIIRS values for 1900PSI at -0° AoA

distance, m	NIIRS pretest	NIIRS 1st best	NIIRS 2nd best	1st best/pretest	2nd best/pretest
1000	9.23	9.22	9.16	99.93%	99.24%
2000	8.23	8.22	8.16	99.92%	99.15%
5000	6.91	6.90	6.84	99.90%	98.98%
10000	5.91	5.90	5.84	99.89%	98.81%
15000	5.33	5.32	5.26	99.87%	98.68%
20000	4.91	4.90	4.84	99.86%	98.57%
25000	4.59	4.58	4.52	99.85%	98.47%
50000	3.59	3.58	3.52	99.81%	98.04%
100000	2.59	2.58	2.52	99.74%	97.28%

Table 5.4 Numerical NIIRS values for 900PSI at -15° AoA

distance, m	NIIRS pretest	NIIRS 1st best	NIIRS 2nd best	1st best/pretest	2nd best/pretest
1000	9.11	9.01	9.00	98.93%	98.80%
2000	8.11	8.01	8.00	98.80%	98.66%
5000	6.79	6.69	6.68	98.57%	98.39%
10000	5.79	5.69	5.68	98.32%	98.12%
15000	5.20	5.10	5.09	98.13%	97.91%
20000	4.79	4.69	4.68	97.97%	97.72%
25000	4.46	4.37	4.36	97.82%	97.56%
50000	3.47	3.37	3.36	97.19%	96.86%
100000	2.47	2.37	2.36	96.06%	95.58%

Table 5.5 Numerical NIIRS values for 900PSI at -0° AoA

distance, m	NIIRS pretest	NIIRS 1st best	NIIRS 2nd best	1st best/pretest	2nd best/pretest
1000	9.21	9.17	9.19	99.61%	99.80%
2000	8.21	8.17	8.19	99.56%	99.78%
5000	6.89	6.85	6.87	99.48%	99.74%
10000	5.89	5.85	5.87	99.39%	99.69%
15000	5.30	5.27	5.29	99.33%	99.66%
20000	4.89	4.85	4.87	99.27%	99.63%
25000	4.57	4.53	4.55	99.22%	99.60%
50000	3.57	3.53	3.55	99.00%	99.49%
100000	2.57	2.53	2.55	98.61%	99.29%

The *GSD* was a key factor for determining *NIRS* of our optical setup, performance and impact of shock structures when extrapolating the results for large observation distances. The results achieved are in agreement with those of the initial testing campaign and showed the greatest effects on optical distortion for those conditions with higher angles of attack and reservoir pressures. Also, as the distance to the object increased, the measured influence of distortion increased as well, but at a declining rate. For the observed conditions the greatest influence on distortion was seen at 1900PSI and -15° , however, which only resulted in a moderate change from the baseline measurement by about 12% from the benchmark image at the greatest observation distance of 100,000 km.

CHAPTER 6. CONCLUSIONS

The goal of this work was to investigate how visible imaging qualitatively and quantitatively is impaired through the boundary layers and shock structures of a Mach 6 flow. For this purpose, two experimental test campaigns were conducted along with Wright Patterson Air Force Base at a Mach 6 high Reynolds Number wind tunnel. Visible imaging of two test probes, a 15° wedge model and a 7° half angle blunt cone was performed through laser etching of optical test patterns that would be applied to the surface of the test models and then injected into flow. Alongside visible imaging, IR and Schlieren measurements were gathered to accompany any supporting information to characterize flow field conditions downstream of the test models. To account for any potential vibrations that may be present in the visible imaging that may be a result from the model or the cameras themselves, accelerometer data was gathered with sensors inside and outside of the test tunnel. This was done by mounting an accelerometer inside a model in the tunnel flow, as well as mounting separate accelerometers to the cameras imaging from outside of the tunnel. Lastly, additional measurements were conducted post testing to support results from both test campaigns using a back illuminated slit. The slit was used to simulate an optical pattern on the surface of the test models. To simulate a distortion effect as introduced by the shock structures in tunnel testing, plano-convex lenses were placed on the optical axis between the camera and back illuminated slit.

In the first test campaign, Strehl ratios were calculated from line distribution functions (*LDFs*) of laser etched lines on an optical target illuminated from outside of the flow. It was observed that measurable optical distortion was only present at the higher reservoir pressures and angles of attack. However, during tunnel operation vibrations were measured at low frequencies, typically <30Hz, that caused significant broadening of the *LDFs*. This was due to the long camera acquisition times that were set with the continuous illumination method to allow for sufficient exposure on the camera CCD. For the second test campaign this was ultimately prevented by using indirect flash illumination sources with short pulse times that allowed for only brief illumination of the test targets much shorter times than impacted by the vibrational frequencies. The new analysis of the wedge probe showed little to no aero-optical distortion, somewhat contradicting the previous results. However,

additional measurements were performed on the wedge using continuous illumination at various camera acquisition times to investigate the effects of low frequency vibrations. These results showed significant influence of vibrations to the vertical lines, but moderate to none on the horizontal lines. Therefore, the earlier results on influence of distortion cannot be linked solely to effect of vibrations.

Additionally, a cone model was investigated for optical distortion using analysis methods similar to the wedge model. The cone was mounted with attachable blunt tips specifying 10% and 20% bluntness to the cone base. Analysis on the cone showed no significant influence of distortion on the probe if equipped with the 20% blunt tip, and moderate but measurable influence with the 10% tip. The measured effects increased with reservoir pressure as already seen before in the wedge measurements. When effects of distortion were detected, the effect decreased for positive angles of attack relative to cone distance, stayed mostly constant for 0° angle of attack, and increased for negative angles of attack relative to distance from the cone tip.

For analysis with the back illuminated slit to support previous test results, new analysis methods were developed to extract high resolution information about the generating *LDFs* from a sub pixel level. The first method was performed by means of a direct linear interpolation of measured line profiles shifted to a common line center defined by their half width and then averaging over multiple profiles, attempting to yield new information about the underlying profiles. The second method involved fitting the measured data through an integration of single high resolution Gauss profiles to the CCD resolution, by means of ratios of maxima of the profile close to center. The third approach involved a superposition of multiple narrow Gauss profiles, which would ultimately create a non-Gauss generating line profile, but fit the measured data much more closely, especially far from center. All 3 analysis methods presented above were successfully automated in MATLAB to enable processing large amounts of data more easily.

The results from these analysis methods in the form of line widths at half maximum ratios were determined to yield Strehl ratios. Strehl ratios are used as a metric in determining the amount of distortion present in a system. Generally, the Strehl ratio is defined as a ratio of the peak intensity of an aberrated point source to the peak intensity from that of a diffraction limited system. It was found that the Strehl ratio could also be

defined as a ratio of the line half widths, which is helpful for relating distortion not as a ratio of maximum values, but as a ratio of the overall shape of the profiles, less likely to be disturbed by additional impacts such as scattering of light.

The back illuminated slit experiments were conducted in controlled lab environment to investigate the accuracy and quality of the three developed analysis methods mentioned earlier. To assist in the understanding of how the slit should react and illuminate the camera CCD, the raytracing software Zemax was used. This provided additional information about the analysis methods, and an assessment which individual method would provide the most accurate results in the automated analysis procedures. The work from the Zemax calculations were conducted by my advisor Dr. Michael Winter. It was observed that the results from the single Gauss interpolation method in some configurations gave the best results but were often unphysical. In the cases identified as unphysical, it was seen that Strehl ratios were greater than 1, meaning that the “distorted” profile was less broad. The direct interpolation method, though not the exact same as the Zemax calculations proved to be consistent, followed by the multiple narrow Gauss superposition method which gave the most accurate results.

Initial analysis of the wind tunnel experiments in the first test campaign was conducted with the direct linear interpolation method. Using the new analysis methods, the measured data from the first test campaign was reanalyzed. All results showed a significant influence of distortion on the wedge at higher pressure conditions and high angles of attack from the preliminary analysis. The same experiments with the wedge in the second test campaign, although this time with flash illumination to eliminate influences that were caused from vibrations, confirmed the same trends as before, but not in the same magnitude. These results from the second test campaign might indicate that the sensitivity in the visible imaging spectrum is less than initially measured.

To support the visible imaging data, IR data was collected alongside to provide possible information on transition locations from laminar to turbulent flow. A transition location could be seen as an increased heat load on the surface downstream of the test models whilst being exposed to the tunnel flow. For the wedge model, a slow increase in heat flux was observed that might indicate transitioning. For the 10% cone however, clear transition to turbulence was seen. The IR agreed very well with data that was already

collected from Wright Patterson Air Force Base; where tests were previously performed, and transition locations were identified using a geometrically similar model that was instrumented with thermocouples every inch down the downstream surface. However, the weak distortion observed at the varying angles of attack could not clearly be linked to this transition to turbulence.

APPENDICES

APPENDIX 1. TEST CAMPAIGN PROTOCOLS

October 2017 Test Campaign Protocol

Note: For the October 2017 test campaign, the “pre test” image to be compared to flow on images in the first image in the folder containing all images for that given test condition. For instance, on date 10/20/2017, Nikon imaging of the wedge plate at 1900PSI was conducted, inside the file of raw data titled the test date are images #####

Date	Diagnostics	Model-Orientation	Pressure (PSI)	Duration (nominal), seconds
10/17/17	IR, Schlieren	flat up, -5 deg	900	20 s
10/17/17	IR, Schlieren	flat up, (-5) 0 deg	900	20 s
10/17/17	IR, Schlieren	flat up, (-5) 0 deg	1400	20 s
10/18/17	IR, Schlieren	flat up, (-5) 0 deg	1900	20 s
10/18/17	Nikon, Redlake	flat side, 90 deg rotated	1900	5s
10/18/17	Nikon, Redlake	flat side, 90 deg rotated	1900	5s
10/18/17	Nikon, Redlake	flat side, 90 deg rotated	1400	5s
10/19/17	Nikon, Redlake	flat side, 90 deg rotated	1400	5s
10/19/17	Nikon, Redlake	flat side, 90 deg rotated	900	5s
10/19/17	Nikon, Redlake	flat side, 90 deg rotated	900	5s
10/19/17	Nikon	wedge side, 15deg	900	5s
10/19/17	Nikon	wedge side, 15deg	900	5s
10/20/17	IR, Schlieren	wedge up, 15deg	900	20 s
10/20/17	IR, Schlieren	wedge up, 15deg	1400	20 s
10/20/17	Nikon	wedge side, 15deg	900	5s
10/20/17	Nikon	wedge side, 15deg	1400	5s
10/20/17	Nikon	wedge side, 15deg	1800	5s
10/23/17	IR, Schlieren	flat up, 0deg	900	20s
10/23/17	IR	flat up, -10deg wrong	1400	2s
10/23/17	IR, Schlieren	flat up, 0deg	1400	20s
10/23/17	IR, Schlieren	flat up, 0deg	1900	20s
10/23/17	IR, Schlieren	wedge up, 15deg	1900	20s
10/23/17	Nikon	flat side, 90 deg rotated	1900	5s
10/23/17	Nikon	flat side, 90 deg rotated	1400	5s
10/23/17	Nikon	flat side, 90 deg rotated	900	5s
10/23/17	Nikon	wedge side, 15deg	1400	5s

10/24/17	IR, Schlieren	flat up, -5deg	1900	20s
10/24/17	IR, Schlieren	flat up, -5deg	1400	20s
10/24/17	IR, Schlieren	flat up, -5deg	900	20s
10/24/17	Nikon	flat side, -5deg, 90deg rotated	1900	5s
10/24/17	Nikon	flat side, -5deg, 90deg rotated	1400	5s
10/24/17	Nikon	flat side, -5deg, 90deg rotated	900	5s
10/24/17	Phantom	flat side, -5deg, 90deg rotated	1400	5s
10/24/17	Phantom	flat side, -5deg, 90deg rotated	900	5s
10/25/17	IR, Schlieren	flat up, -5deg	1900	20s
10/25/17	IR, Schlieren	flat up, -15deg	1400	20s
10/25/17	Phantom	flat side, -5deg, 90 deg rotated	1900	5s
10/25/17	Phantom	flat side, 90 deg rotated	1900	5s
10/25/17	Phantom	flat side, 90 deg rotated	1400	5s
10/25/17	Phantom	flat side, 90 deg rotated	900	5s
10/26/17	IR, Schlieren	wedge up, 10deg	900	20s
10/26/17	IR, Schlieren	wedge up, 10deg	1400	20s
10/26/17	IR, Schlieren	wedge up, 10deg	1900	20s
10/26/17	Phantom	wedge side, 10deg	900	5s
10/26/17	Phantom	wedge side, 15deg	900	5s
10/26/17	Phantom	wedge side, 10deg	1400	5s
10/26/17	Phantom	wedge side, 15deg	1400	5s
10/26/17	Phantom	wedge side, 10deg	1900	5s
10/26/17	Phantom	wedge side, 15deg	1900	5s
10/26/17	Nikon	wedge side, 10deg	900	5s
10/26/17	Nikon	wedge side, 10deg	1400	5s
10/26/17	Nikon	wedge side, 10deg	1900	5s
10/27/17	IR, Schlieren	wedge up, 0deg	1900	20s

Feb-March 2019 Test Campaign Protocol

During the 2019 test campaign for the Nikon visible imaging tests many pre test images may have been taken for various configurations. It is important to refer to this chart to know which image numbers refer to in and out of flow testing. The out of flow test images were taken just moments before tunnel on conditions were applied which then the model was put into flow and subsequent images were immediately gathered.

Day	Diagnostics	Model-Orientation	Pressure (PSI)	Duration (sec)	Pre-test Image #'s	During test Image #'s
2/20/19	Nikon, Xe	15-deg towards side window	900	8	7322-7326	7336-7341
2/20/19	Nikon, Xe	15-deg towards side window	900	8	7366 (tunnel lights)	7368-7372
2/20/19	Nikon, Xe	15-deg towards side window	900	8	7382-	7383-7388
2/21/19	Nikon, Xe	0-deg towards side window	900	8	7397-	7399-7403
2/21/19	Nikon, Xe	0-deg towards side window	900	8	7419-	7420-7423
2/21/19	Nikon, Xe	0-deg towards side window	1900	10	7427-	7428-7434
2/21/19	Nikon, Xe	0-deg towards side window	1400	10	7435-7445-7447	7437-7441
2/21/19	Nikon, Xe	WP 7-deg cone testing	900		7448-7450	7461-7474
2/21/19	Nikon, Tunnel lights	WP 7-deg cone testing	900		7451-7453	
2/21/19	Nikon, Xe	WP 7-deg cone testing	1900		7475-	7477-7487
2/21/19	Nikon, LED lights	0-deg towards side window	900	3	7517-	7518-7531
2/21/19	Nikon, LED lights	0-deg towards side window	900	3	7532-	7533-7546
2/21/19	Nikon, LED lights	0-deg towards side window	900	3	7547-	7548-7561
2/21/19	Nikon, LED lights	0-deg towards side window	900	3	7562-	7563-7576
2/21/19	Nikon, LED lights	0-deg towards side window	900	3	7577-	7578-7591
2/21/19	Nikon, LED lights	0-deg towards side window	900	3	7592-	7593-7606
2/25/19	Nikon, Xe	5-deg towards side window	1900 (1830)	10	7624-	7627-7631
2/25/19	Nikon, Xe	5-deg towards side window	900	10	7634-	7635-7639
2/25/19	Nikon, Xe	0-deg towards side window	1900 (1800)	10	7642-	7643-7647
2/25/19	Nikon, Xe	0-deg towards side window	900	10	7650-	7651-7655

2/25/19	Nikon, Xe	10-deg towards side window	1900 (1785)	10	7661-	7662-7665
2/25/19	Nikon, Xe	10-deg towards side window	900	10	7671-	
2/26/19	Nikon, Xe	15-deg towards side window	1900	10	7679-	7680-7684
2/26/19	Nikon, Xe	15-deg towards side window	900	10	7694-	7695-7701
2/26/19	Photron SA-Z	0-deg towards upper window front edge of plate	1900	1		
2/26/19	Photron SA-Z	0-deg towards upper window front edge of plate	900	1		
2/26/19	Photron SA-Z	5-deg towards upper window front edge of plate	1900	1		
2/26/19	Photron SA-Z	5-deg towards upper window front edge of plate	900	1		
2/26/19	Photron SA-Z	10-deg towards upper window front edge of plate	1900	1		
2/26/19	Photron SA-Z	10-deg towards upper window front edge of plate	900	1		
2/26/19	Photron SA-Z	15-deg towards side window front edge of plate	1900	1		
2/26/19	Photron SA-Z	15-deg towards side window front edge of plate	900	1		
2/26/19	Photron SA-Z	0-deg towards upper window back edge of plate	900	1		
2/26/19	Photron SA-Z	0-deg towards upper window back edge of plate	1900 (1800)	1		
2/26/19	Photron SA-Z	5-deg towards upper window back edge of plate	900	1		
2/26/19	Photron SA-Z	10-deg towards upper window back edge of plate	900	1		
2/26/19	Photron SA-Z	15-deg towards upper window back edge of plate	900	1		
2/27/19	FLIR	0-deg towards upper window	900	15		
2/27/19	FLIR	0-deg towards upper window	900	15		
2/27/19	FLIR	0-deg towards upper window	1900	15		
2/27/19	FLIR	5-deg towards upper window	900	15		
2/27/19	FLIR	5-deg towards upper window	1900	15		
2/27/19	FLIR	10-deg towards upper window	1900	15		

2/27/19	FLIR	10-deg towards upper window	900	15
2/28/19	FLIR	15-deg towards upper window	1900	15
2/28/19	FLIR	15-deg towards upper window	1900	15
2/28/19	FLIR	15-deg towards upper window	900	15
2/28/19	FLIR	10-deg towards upper window	1900	15
2/28/19	FLIR	5-deg towards upper window	1900 (1875)	15
2/28/19	FLIR	10-deg towards upper window	900	15
2/28/19	FLIR	5-deg towards upper window	900	15
2/28/19	FLIR/Photron SA-Z	0-deg towards upper window front edge of plate.	900	
2/28/19	FLIR/Photron SA-Z	0-deg towards upper window front edge of plate.	1900	
2/28/19	FLIR/Photron SA-Z	5-deg towards upper window front edge of plate	1900	
2/28/19	FLIR/Photron SA-Z	5-deg towards upper window front edge of plate	900	
3/1/19	Photron SA-Z	10-deg towards upper window front edge of plate	900	
3/1/19	Photron SA-Z	10-deg towards upper window front edge of plate	1900	
3/1/19	Photron SA-Z	0-deg towards upper windows front edge of plate	900	
3/1/19	Photron SA-Z	0-deg towards upper windows front edge of plate	1900	
3/1/19	Photron SA-Z	5-deg towards upper window front edge of plate	1900	
3/1/19	Photron SA-Z	5-deg towards upper window front edge of plate	900	
3/1/19	Photron SA-Z	0-deg towards upper window back edge of plate	1900	
3/1/19	Photron SA-Z	0-deg towards upper window back edge of plate	900	
3/1/19	Photron SA-Z	5-deg towards upper window back edge of plate	900	
3/1/19	Photron SA-Z	5-deg towards upper window back edge of plate	900	
3/1/19	Photron SA-Z	5-deg towards upper window back edge of plate	900	

3/1/19	Photron SA-Z	0-deg towards upper window back edge of plate	900			
3/4/19	Nikon, LED lights	15-deg towards side window	1400	10	7796-	7797-7810
3/4/19	Nikon, LED lights	15-deg towards side window	1400	10	7811-	7812-7825
3/4/19	Nikon, LED lights	4-deg away from side window	-		7836-	
3/4/19		CALIBRATION FOR CONE				
3/5/19		RE-CALIBRATION FOR CONE (0.6ms INT)				
3/5/19		RE-CALIBRATION FOR CONE (0.6ms INT)				
3/5/19		RE-CALIBRATION FOR WEDGE (0.4ms INT)				
3/5/19	Nikon, LED lights, IR	20% cone 0-deg yaw towards Nikon camera	900		7860-7861	7862-7875
3/5/19	Nikon, LED lights, IR	20% cone 0-deg yaw towards Nikon camera	1400		7876-7877	7878-7891
3/5/19	Nikon, LED lights, IR	20% cone 0-deg yaw towards Nikon camera	1900		7892-7893	7894-7907
					7908-7909 (7910 external lights off)	7911-7924
3/5/19	Nikon, LED lights, IR	20% cone 4-deg yaw towards Nikon camera	900		7925-7926	7927-7940
3/5/19	Nikon, LED lights, IR	20% cone 4-deg yaw towards Nikon camera	1400		7941-7942	7943-7956
3/5/19		RE-CALIBRATION FOR CONE (1.5ms INT)				
3/6/19	IR, Schlieren	20% cone 4-deg pitch towards IR camera	1900			
3/6/19	IR, Schlieren	20% cone 4-deg pitch towards IR camera	1400			
3/6/19	IR, Schlieren	20% cone 4-deg pitch towards IR camera	900			
3/6/19	Nikon, LED lights, IR	10% cone 4-deg yaw towards Nikon camera	1900		7958-7959	7960-7973
3/6/19	Nikon, LED lights, IR	10% cone 4-deg yaw towards Nikon camera	1400		7974-7975	7976-7989
3/6/19	Nikon, LED lights, IR	10% cone 4-deg yaw towards Nikon camera	900		7990-7991	7992-8005
3/6/19	Nikon, LED lights, IR	10% cone 0-deg yaw towards Nikon camera	1900		8015-8016	8017-8021

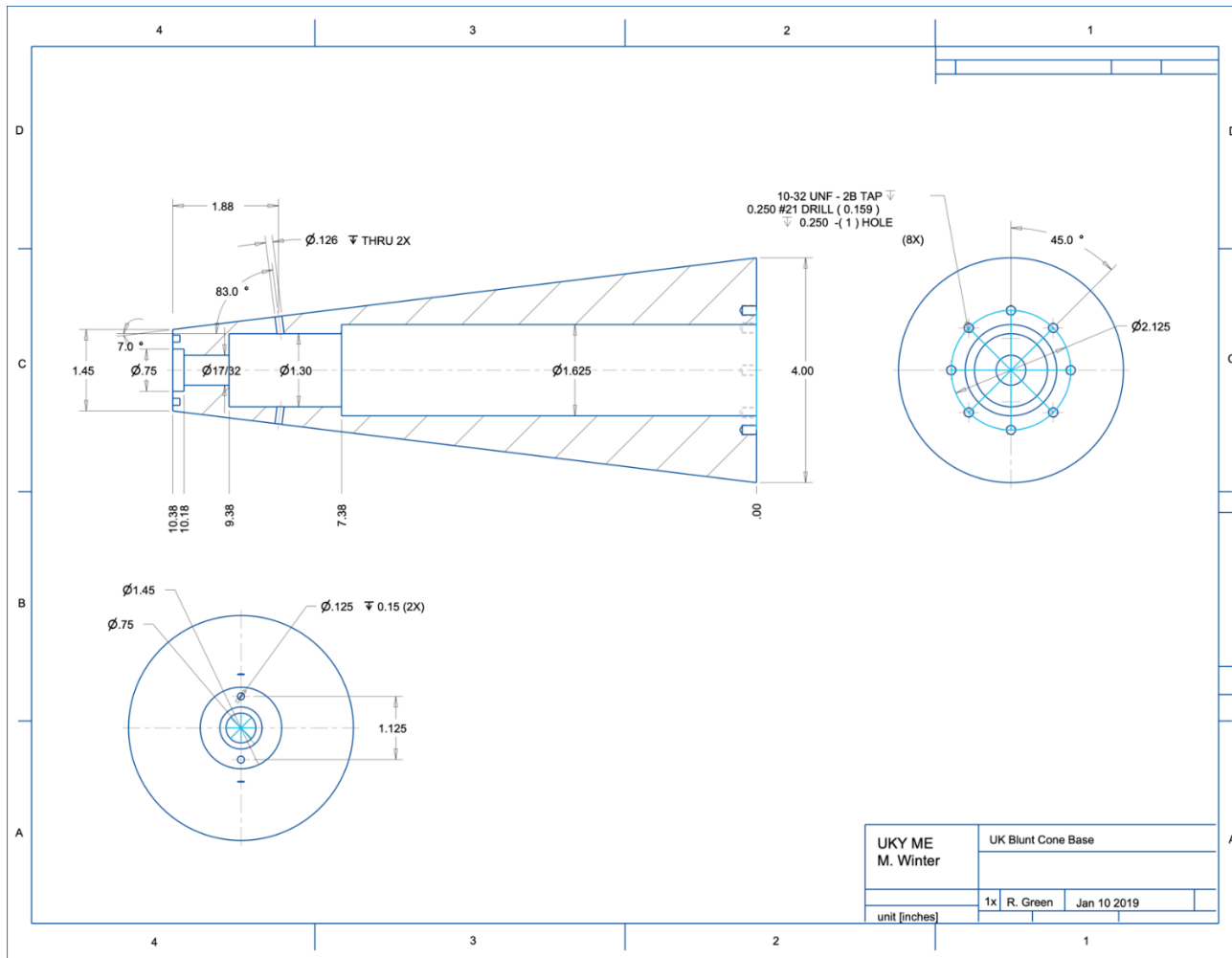
3/6/19	Nikon, LED lights, IR	10% cone 0-deg yaw towards Nikon camera	1400	8022-8023	8024-8037
3/6/19	Nikon, LED lights, IR	10% cone 0-deg yaw towards Nikon camera	900	8038-8039	8040-8053
3/6/19	Nikon, LED lights, IR	10% cone -4-deg yaw towards Nikon camera	1900	8055-8056	8057-8070
3/6/19	Nikon, LED lights, IR	10% cone -4-deg yaw towards Nikon camera	1400	8071-8072	8073-8086
3/6/19	Nikon, LED lights, IR	10% cone -4-deg yaw towards Nikon camera	900	8087-8088	8089-8102
3/7/19	IR, Schlieren	10% cone 4-deg pitch towards IR camera	1900		
3/7/19	IR, Schlieren	10% cone 4-deg pitch towards IR camera	1400		
3/7/19	IR, Schlieren	10% cone 4-deg pitch towards IR camera	900		
3/7/19	IR, Schlieren	10% cone -4-deg pitch towards IR camera	1900		
3/7/19	IR, Schlieren	10% cone -4-deg pitch towards IR camera	1400		
3/7/19	IR, Schlieren	10% cone -4-deg pitch towards IR camera	900		
3/7/19	IR, Schlieren	20% cone -4-deg pitch towards IR camera	1900		
3/7/19	IR, Schlieren	20% cone -4-deg pitch towards IR camera	1400		
3/7/19	IR, Schlieren	20% cone -4-deg pitch towards IR camera	900		
3/12/19	Nikon, LED lights	0-deg towards side window	1900	8123-8124	8125-8138
3/12/19	Nikon, LED lights	0-deg towards side window	1900	8139-8140	8141-8154
3/12/19	Nikon, LED lights	0-deg towards side window	1900	8157-8158	8159-8172
3/12/19	Nikon, LED lights	0-deg towards side window	1900	8173-8174	8175-8188
3/12/19	Nikon, LED lights	0-deg towards side window	1900	8189-8190	8191-8204
3/12/19	Nikon, LED lights	0-deg towards side window	1900	8214-8215	8216-8229
3/12/19	Nikon, LED lights	0-deg towards side window	1900	8232-8233	8234-8247
3/12/19	Nikon, LED lights	0-deg towards side window	1900	8249-8250	8251-8264
3/12/19	Nikon, LED lights	0-deg towards side window	1900	8265-8266	8267-8280

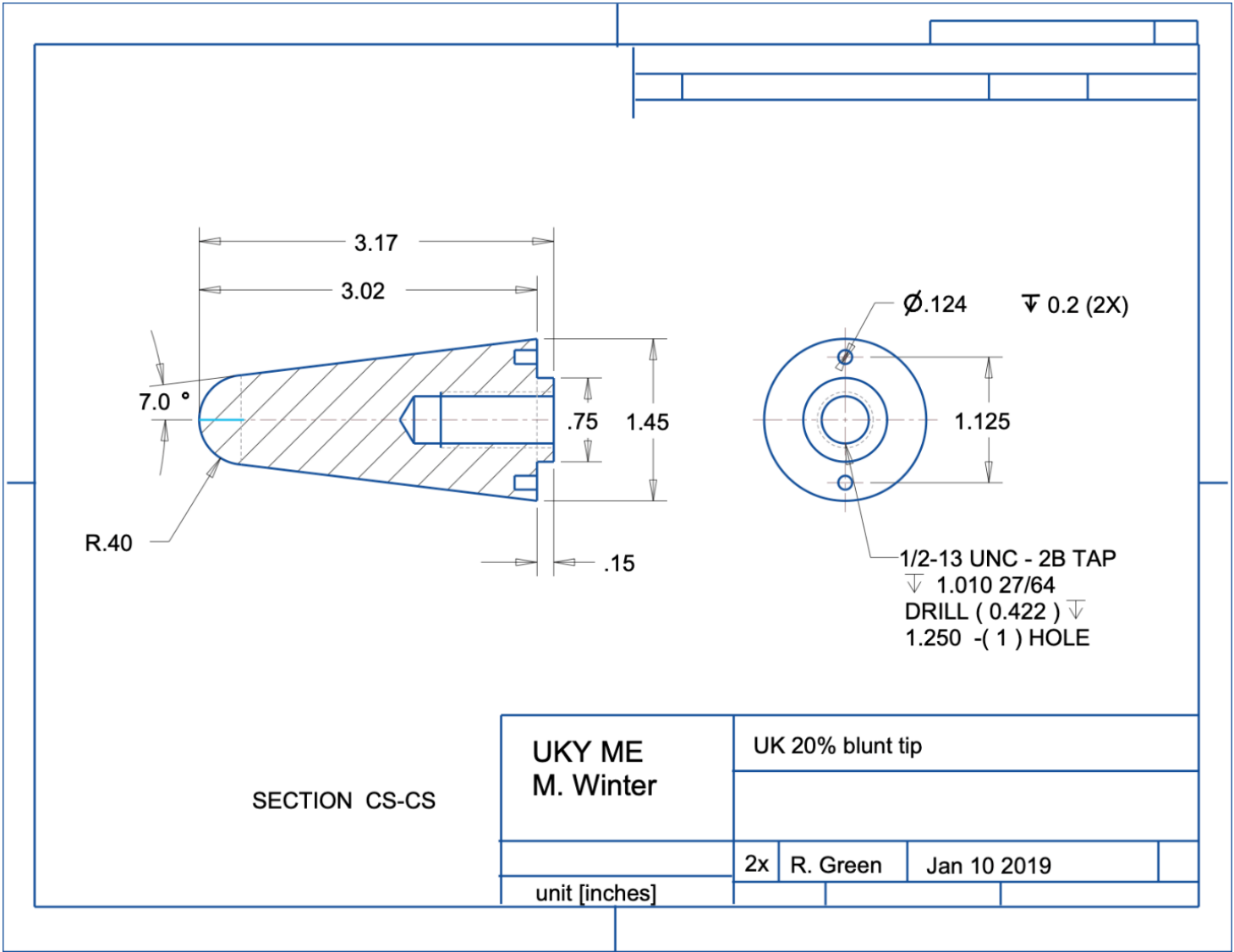
3/13/19	Nikon, LED lights	15-deg towards side window	1900	8283-8284	8285-8298
3/13/19	Nikon, LED lights	15-deg towards side window	1900	8299-8300	8301-8314
3/13/19	Nikon, LED lights	15-deg towards side window	1900	8315-8316	8317-8330
3/13/19	Nikon, LED lights	15-deg towards side window	1900	8331-8332	8333-8346
3/13/19	Nikon, LED lights	15-deg towards side window	1900	8347-8348	8349-8362
3/13/19	Nikon, LED lights	15-deg towards side window	1900	8363-8364	8365-8378
3/13/19	Nikon, LED lights	10% cone 4-deg yaw towards Nikon camera	1900	8386-8387	8388-8401
3/13/19	Nikon, LED lights	10% cone 4-deg yaw towards Nikon camera	1400	8402-8403	8404-8417
3/13/19	Nikon, LED lights	10% cone 4-deg yaw towards Nikon camera	900	8418-8419	8420-8433
3/13/19	Nikon, LED lights	10% cone 0-deg yaw towards Nikon camera	1900	8436-8437	8438-8451
3/13/19	Nikon, LED lights	10% cone 0-deg yaw towards Nikon camera	1400	8452-8453	8454-8467
3/13/19	Nikon, LED lights	10% cone 0-deg yaw towards Nikon camera	900	8468-8469	8470-8483
3/13/19	Nikon, LED lights	10% cone -4-deg yaw towards Nikon camera	1900	8486-8487	8488-8501
3/13/19	Nikon, LED lights	10% cone -4-deg yaw towards Nikon camera	1900	8504-8505	8506-8519
3/13/19	Nikon, LED lights	10% cone -4-deg yaw towards Nikon camera	1400	8520-8521	8522-8535
3/13/19	Nikon, LED lights	10% cone -4-deg yaw towards Nikon camera	900	8536-8537	8538-8551
3/14/19	Nikon, camera flash	10% cone 4-deg yaw towards Nikon camera	1900	8687-	8688-8696
3/14/19	Nikon, camera flash	10% cone 4-deg yaw towards Nikon camera	1400	8703-	8705-8713
3/14/19	Nikon, camera flash	10% cone 4-deg yaw towards Nikon camera	900	8718-	8719-8727
3/14/19	Nikon, camera flash	10% cone 0-deg yaw towards Nikon camera	1900	8734-	8735-8746
3/14/19	Nikon, camera flash	10% cone 0-deg yaw towards Nikon camera	1400	8749-	8751-8758
3/14/19	Nikon, camera flash	10% cone 0-deg yaw towards Nikon camera	900	8764-	8766-8776
3/14/19	Nikon, camera flash	10% cone -4-deg yaw towards Nikon camera	1900	8781-	8783-8792

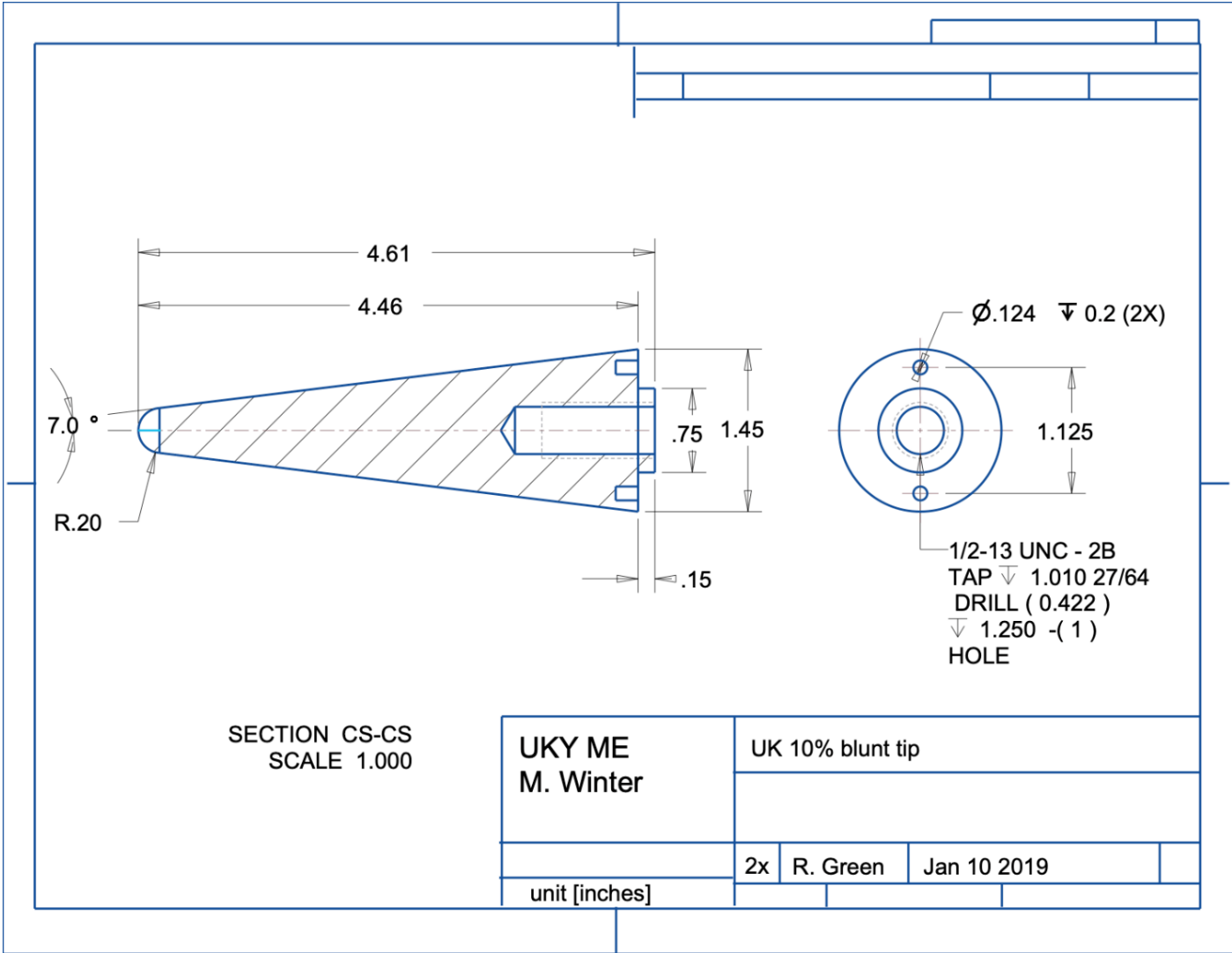
3/14/19	Nikon, camera flash	10% cone -4-deg yaw towards Nikon camera	1400	8796-	8798-8805
3/14/19	Nikon, camera flash	10% cone -4-deg yaw towards Nikon camera	900	8814-	8816-8827

APPENDIX 2. TECHNICAL DRAWINGS

93







REFERENCES

- [1] Smith, W. J. (2000a). *Modern Optical Engineering* (3rd ed.). McGraw-Hill Professional.
- [2] Wyckham, C. M., & Smits, A. J. (2009). Aero-Optic Distortion in Transonic and Hypersonic Turbulent Boundary Layers. *AIAA*, 47. doi:10.2514/1.41453
- [3] Winter, M., Green, R., Borchetta, C., Josyula, E., Hayes, J.R., Jewell, J.S., Hagen, B., "Experimental Investigation of Image Distortion in a Mach 6 Hypersonic Flow," AIAA 2018-4197, 2018 Aerodynamic Measurement Technology and Ground Testing Conference, AIAA AVIATION Forum, , June 25-29, 2018, Atlanta, GA.
- [4] Li, H., Yan, C., & Shao, J. (2016). Measurement of the Modulation Transfer Function of Infrared Imaging System by Modified Slant Edge Method. *Journal of the Optical Society of Korea*, 20(3), 381-388. <https://doi.org/10.3807/josk.2016.20.3.381>
- [5] Leachtenauer, J. C., Malila, W., Irvine, J., Colburn, L., & Salvaggio, N. (1997). General Image-Quality Equation: GIQE. *Applied Optics*, 36(32), 8322. doi:10.1364/ao.36.008322
- [6] Thurman, S. T., & Fienup, J. R. (2008). Analysis of the general image quality equation. *Visual Information Processing XVII*. doi:10.1117/12.777718
- [7] Harrington, L., Blanchard, D., Salacain, J., Smith, S., & Amanik, P. (2015, September 16). General Image Quality Equation; GIQE version 5. Retrieved from <https://www.nga.mil>.
- [8] Jewell, J. S., Kennedy, R. E., Laurence, S. J. and Kimmel, R. L.. "Transition on a Variable Bluntness 7-Degree Cone at High Reynolds Number." AIAA SciTech 2018, January 2018, Kissimmee, FL. AIAA 2018-1822. doi: 10.2514/6.2018-1822
- [9] Jewell, J. S. and Kimmel, R. L.. "Boundary-Layer Stability Analysis for Stetson's Mach 6 Blunt-Cone Experiments", *Journal of Spacecraft and Rockets*, Vol. 54, No. 1 (2017), pp. 258–265. doi:10.2514/1.A33619
- [1] Ali, M., Eltohamy, F., & Salama, G. (2016). Estimation of NIIRS, for High Resolution Satellite Images, Using the Simplified GIQE. *International Journal of Innovative Research in Computer and Communication Engineering*, 4(5), 8403-8408. doi:10.15680/IJIRCCE.2016.0405047
- [11] Anderson, J. D. (2006). *Hypersonic and high-temperature gas dynamics*. American Institute of Aeronautics and Astronautics.
- [12] Goodman, J. W. (1996). *Introduction to Fourier optics*. McGraw-Hill Professional.

VITA

Ricky Green

Education

MS Mechanical Engineering – August 2021
University of Kentucky, Lexington, KY

BA Physics – May 2016
Berea College, Berea, KY

Publications

Experimental Investigation of Image Distortion in a Mach 6 Hypersonic Flow,
AIAA 2018 [3]